UNIVERSITY OF ICELAND

Faculty of Mathematics, Computer Science and Natural Sciences

RWTH AACHEN UNIVERSITY

Simulation studies of Hopfions in atomistic spin systems

Der Fakultät für Mathematik, Informatik und Naturwissenschaften der RWTH Aachen University vorgelegte Dissertation zur Erlangung des akademischen Grades eines Doktors der Naturwissenschaften

von

Moritz Sallermann, M.Sc
ORCID: 0000-0002-2355-9355

aus

Kleve, Deutschland

ACKNOWLEDGEMENTS

I would like to thank Prof. Hannes Jónsson, who has supervised and supported me, especially during my move to Iceland in the latter half of my thesis work. Hannes gave me a lot of freedom and encouragement for exploring and developing my scientific interests. Beyond that, he has been much more than just a scientific advisor.

In the same breath, I would like to express my gratitude to Prof. Stefan Blügel for his supervision and giving me a place at his institute during my two stints – first as a masters student, then as a doctoral student. His advice and ever enthusiastic nature have encouraged me throughout all of this work.

I am grateful to the very patient Prof. Elvar Örn Jónsson for enabling me to expand my scientific horizons beyond the field of atomistic spin dynamics (working on polarizable water force fields) and for funding me for significant stretches.

I would also like to thank Prof. Pavel Bessarab, who, on many occasions, has helped me with his advice and insight into rate calculations in spin systems and has even shouldered parts of my salary.

I gratefully acknowledge scientific discussions (sometimes collaborations) with Dr. Nikolai Kiselev, Prof. Samir Lounis, Dr. Fabian Lux, Dr. Bernd Zimmermann, Markus Hoffmann, Dr. Rohit Goswami, Dr. Amrita Goswami, Dr. Alejandro Peña-Torres and Dr. Hendrik Schrautzer.

I would like to express my gratitude to Dr. Amal Aldarawsheh for many successful collaborations.

Further, I am grateful to Dr. Gideon Müller for his continued advice and mentorship over the years, introducing me to Spirit and for helping out with it even after he had long moved on from Jülich.

I am grateful to the members of the group of Hannes Jónsson, of which Elli and Alejandro deserve a special mention for being awesome housemates during my first few stays in Iceland.

Lastly, I want to thank my family – Ansgar, Bertil, Martina, Christoph, Britta, Janick, Stefan, Kerstin, Sonaly, Debu, Rohit and Ruhi. A very special mention goes to Amrita, who has enriched every part of my life and has been tremendously supportive during the completion of this work.

ABSTRACT

The main protagonists of this thesis, magnetic Hopfions, are three-dimensional topological solitons characterized by the Hopf invariant, a quantity that measures the linking number of pre-images of constant magnetization within magnetic textures. These intriguing solitons appear as local, spatially compact, energy minima in bulk magnetic materials featuring competing exchange interactions, making them ideal candidates for exploring fundamental physical phenomena as well as potential building blocks for advanced spintronic devices. However, determining their practical stability and viability in technological applications necessitates an in-depth analysis of their decay mechanisms, especially in environments subject to thermal fluctuations.

In this thesis, we employ an atomistic spin lattice model, concretely a Heisenberg model with competing exchange interactions, to describe the Hopfion, which we investigate by means of atomistic spin dynamics. In particular, we employ harmonic transition state theory (HTST), a powerful and computationally efficient framework, to rigorously assess the lifetime and decay dynamics of Hopfions.

We further extend the conventional HTST approach – as commonly applied to spin systems where only magnetization precession over the transition state is considered – by explicitly incorporating thermal crossings of the transition state. This extension provides a more complete and physically accurate description of thermally activated decay processes, accounting not only for precessional dynamics but also for thermal fluctuations enabling magnetization states to cross the saddle region, thus improving lifetime predictions. A fundamental example where this contribution is, perhaps, felt the most is the reversal of a single spin under the influence of uniaxial anisotropy (think of a hard ferromagnet) – where conventional HTST fails to predict any rate at all.

To accurately quantify these dynamics, we implement computational techniques such as the geodesic nudged elastic band (GNEB) method combined with an adapted dimer method, enabling precise identification of transition states and corresponding energy barriers associated with Hopfion decay. Following common methodology, we locate first-order saddle points on an energy landscape, representing critical states where decay occurs via the nucleation and subsequent propagation of Bloch points. Our investigations reveal a clear dependence of Hopfion stability on their size, relative to the underlying

lattice structure, demonstrating that larger Hopfions generally exhibit increased robustness against decay.

Moreover, this research explicitly addresses several critical technical challenges inherent to the computational methods employed. These include (i) the accurate treatment and interpretation of Goldstone modes, which emerge due to inherent symmetry properties of the Hopfion configurations, and (ii) the computational complexity associated with evaluating sparse positive-definite determinants, which is essential for determining entropic pre-factors. By resolving these challenges, our study not only provides quantitative predictions of Hopfion lifetimes but also offers qualitative insights into the interplay between energy and entropy in these topological systems.

Through this comprehensive theoretical and numerical analysis, the work presented in this thesis significantly advances the understanding of the fundamental principles governing Hopfion stability.

KURZZUSAMMENFASSUNG

Im Mittelpunkt dieser Arbeit stehen magnetische Hopfionen, dreidimensionale topologische Solitonen, die durch die Hopf-Invariante charakterisiert werden. Diese Größe gibt die Verknüpfungszahl der Urbilder konstanter Magnetisierung innerhalb einer magnetischen Textur an. Diese faszinierenden Solitonen treten, unter anderem, als lokale, räumlich kompakte Energieminima in magnetischen Materialien mit konkurrierenden Austauschwechselwirkungen auf. Dadurch sind sie sowohl für die Untersuchung grundlegender physikalischer Phänomene als auch als potenzielle Bausteine für neuartige spintronische Bauelemente von besonderem Interesse. Um ihre tatsächliche Stabilität und ihre Eignung für technologische Anwendungen beurteilen zu können, ist jedoch eine eingehende Analyse ihrer Zerfallsmechanismen erforderlich, insbesondere unter dem Einfluss thermischer Fluktuationen.

In dieser Arbeit verwenden wir ein atomistisches Spingittermodell, konkret ein Heisenberg-Modell mit konkurrierenden Austauschwechselwirkungen, zur Beschreibung von Hopfionen und untersuchen deren Dynamik mithilfe atomistischer Spindynamik. Insbesondere setzen wir die harmonische Übergangszustandstheorie (harmonic transition state theory, HTST) ein, ein leistungsfähiges und recheneffizientes Verfahren zur quantitativen Bestimmung der Lebensdauer und Zerfallsdynamik von Hopfionen.

Darüber hinaus erweitern wir den konventionellen HTST-Ansatz, wie er üblicherweise auf Spinsysteme angewendet wird, bei denen lediglich die Präzession der Magnetisierung am Übergangszustand berücksichtigt wird, indem wir thermisch bedingte Überquerungen des Übergangszustands explizit einbeziehen. Diese Erweiterung ermöglicht eine vollständigere und physikalisch realistischere Beschreibung thermisch aktivierter Zerfallsprozesse. Dabei werden nicht nur präzessionale Dynamiken berücksichtigt, sondern auch thermische Fluktuationen, die es Magnetisierungszuständen ermöglichen, den Sattelbereich zu überqueren. Dadurch lassen sich insbesondere Vorhersagen der Lebensdauer verbessern. Ein grundlegendes Beispiel, bei dem der Einfluss dieses zusätzlichen Beitrags besonders deutlich wird, ist die Umkehr eines einzelnen Spins unter dem Einfluss uniaxialer Anisotropie, wie sie etwa in einem hartmagnetischen Ferromagneten auftritt. In diesem Fall liefert die konventionelle HTST überhaupt keine Übergangsrate.

Zur genauen Quantifizierung dieser Dynamik implementieren wir numerische Verfahren wie die Geodesic-Nudged-Elastic-Band-Methode (GNEB) in Kombination mit einer angepassten Dimer-Methode. Diese ermöglichen eine präzise Bestimmung der Übergangszustände sowie der zugehörigen Energiebarrieren für den Zerfall von Hopfionen. Entsprechend der etablierten Methodik bestimmen wir Sattelpunkte erster Ordnung auf der Energielandschaft. Diese stellen kritische Zustände dar, an denen der Zerfall durch die Nukleation und anschließende Ausbreitung von Bloch-Punkten erfolgt. Unsere Untersuchungen zeigen eine deutliche Abhängigkeit der Stabilität von Hopfionen von ihrer Größe relativ zur zugrunde liegenden Gitterstruktur. Insbesondere erweisen sich größere Hopfionen im Allgemeinen als robuster gegenüber Zerfallsprozessen.

Darüber hinaus behandelt diese Arbeit explizit mehrere wesentliche technische Herausforderungen, die mit den verwendeten numerischen Methoden verbunden sind. Dazu gehören (i) die korrekte Behandlung und Interpretation von Goldstone-Moden, die aufgrund der inhärenten Symmetrien der Hopfion-Konfigurationen auftreten, sowie (ii) der hohe Rechenaufwand bei der Auswertung von Determinanten dünnbesetzter positiv definiter Matrizen, die für die Bestimmung entropischer Vorfaktoren erforderlich sind. Durch die Bewältigung dieser Herausforderungen liefert diese Arbeit nicht nur quantitative Vorhersagen für die Lebensdauer von Hopfionen, sondern ermöglicht auch qualitative Einblicke in das Zusammenspiel von Energie und Entropie in diesen topologischen Systemen.

Durch diese umfassende theoretische und numerische Analyse trägt die vorliegende Arbeit wesentlich zu einem vertieften Verständnis der grundlegenden physikalischen Prinzipien bei, welche die Stabilität magnetischer Hopfionen bestimmen.

ÁGRIP

Megin viðfangsefni þessarar ritgerðar eru segul Hopf-eindir, en það eru þrívíðar stakeindir sem einkennast af Hopf-fastanum, stærð sem lýsir því hvernig ferlar með tilteknu gildi á segulvæginu fléttast í rúminu. Þessar áhugaverðu stakeindir samsvara staðbundnum orkulágmörkum í sumum seglandi efnum og eru afleiðing af stríðandi skiptaverkunum. Rannsóknir á þeim geta því gefið upplýsingar um grundvallar eðliseiginleika en það er líka mögulegt að þær verði notaðar í háþróuðum spunarásum. Lykilatriðið varðandi hagnýtingu Hopf-einda er að kanna hvernig þær eyðast og þá hver líftími þeirra er við tiltekið hitastig.

Í ritgerðinni er notað atómskala líkan af Heisenberg gerð með stríðandi skiptaverkunum til að fá fram Hopf-eindir og kanna tímaframvindu spunakerfisins. Sérstaklega er kjörsveifilsnálgun virkjunarástandskenningarinnar (HTST) notuð, en það er skilvirk og öflug aðferð til að fá mat á líftíma staðbundinna segulástanda sem og hvarfganginum við eyðingu þeirra.

HTST aðferðafræðin er ennfremur útvíkkuð með því að taka til greina varmadrifnar færslur kerfisins í gegnum virkunarástandið. Þessi útvíkkun aðferðafræðinnar gefur betri lýsingu og mat á líftíma segulástanda með því að taka til greina flökt vegna hitastigs auk pólveltunnar. Grundvallar dæmi um mikilvægi þessa er snúningur staks spuna með stefnuhneigð (t.d. harður segull) þar sem HTST nálgunin bregst þar eð hún spáir engum líkum á hvarfi. Til að lýsa þessum segulbreytingum á magnbundinn hátt eru reikniaðferðir innleiddar svo sem gagnvega hnippt teygjuband (GNEB) tengt við aðlagaða tvennuaðferð til að ákvarða virkjunarástönd nákvæmlega og þar með samsvarandi orkuhóla fyrir eyðingu Hopf-einda. Í samræmi við viðtekna aðferðafræði, eru fyrstu gráðu söðulpunktar fundnir á orkulandslaginu. Þeir sýna að eyðing Hopf-eindanna felur í sér myndun Bloch punkta sem síðan ferðast um efnið. Rannsóknirnar sýna að stöðugleiki Hopf-eindanna fer eftir stærð þeirra miðað við grindarfastann, þannig að stærri eindir eyðast síður.

Rannsóknarverkefnið felur einnig í sér ýmsa útvíkkun og endurbætur á aðferðarfræðinni sem er notuð í reikningunum, þar með: (i) skilvirka lýsingu og túlkun á Goldstone háttum sem koma fram vegna samhverfu Hopf-eindanna, og (ii) skilvirka reikninga á gisnu jákvæðu ákveðunni í forstuðli líftímalíkingarinnar sem tengd er entrópíu. Með því að yfirstíga þessar áskoranir gefa niðurstöður reikninganna ekki

bara tölulega spá um líftíma Hopf-eindanna heldur gefa þær líka innsýn í samspil orku og entrópíu í þessum kerfum.

Þær kennilegu og tölulegu greiningar sem ritgerðin setur fram bæta verulega við skilning okkar á þeim grundvallar þáttum sem hafa áhrif á stöðugleika Hopf-einda

CONTENTS

1 Introduction **19**
- 1.1 Geometry . . . 26
- 1.2 The Heisenberg Hamiltonian . . . 28
- 1.3 Equation of motion . . . 29
  - 1.3.1 The linearized thermal LLG equation . . . 31
- 1.4 Computing the time-evolution of the LLG equation . . . 34
  - 1.4.1 Choosing a time step . . . 36
  - 1.4.2 Time reversibility . . . 37
- 1.5 Energy Minimization . . . 41

2 Saddle point searches **44**
- 2.1 The geodesic nudged elastic band method . . . 45
- 2.2 Minimum Mode Following Method . . . 48
  - 2.2.1 The NEB dimer method . . . 49
  - 2.2.2 Components of the dimer movement . . . 50
  - 2.2.3 Backtracking line search for the dimer method 53
- 2.3 Finding extremal eigenpairs via direct optimization . . . 55
- 2.4 Alternative Saddle Point Search Methods . . . 56
  - 2.4.1 Gradient Extremals . . . 59
  - 2.4.2 Gentlest Ascent Dynamics . . . 61
  - 2.4.3 Cosine square ridge following . . . 63

3 Rate theory **66**
- 3.1 Transition state theory . . . 67
- 3.2 Harmonic transition state theory . . . 68
  - 3.2.1 The entropic contribution . . . 70
  - 3.2.2 The dynamical contribution . . . 71
- 3.3 Single anisotropic spin flip . . . 78
- 3.4 Computation of determinants of large matrices . . . 80
  - 3.4.1 Positive definite determinants . . . 80
  - 3.4.2 Sparse decomposition methods . . . 81
  - 3.4.3 Statistical sampling with the Hutchinson trace estimator . . . 87
- 3.5 Goldstone modes . . . 88
  - 3.5.1 Transition between zero-modes and harmonic modes . . . 88
- 3.6 Mode volumes of solitons . . . 91
  - 3.6.1 Constructing modes . . . 93

3.6.2 Zero-mode volume of a translation 95
3.6.3 Zero-mode volume of a rotation 96

4 Hopfions in magnets **98**
4.1 The RKBDMB-model 100
4.2 Energy barriers of Hopfions in the RKBDMB-model . 102
4.3 Lifetimes of Hopfions in the RKBDMB-model 102
4.3.1 Zeromode analysis 104
4.3.2 Determinant computation 111
4.3.3 Lifetimes 115

5 Conclusion **118**

A Appendix **121**
A.1 HTST rate for the flip of a single spin with uniaxial anisotropy 121
A.2 Colorcode for spin isosurfaces 122
A.3 Used software packages 122

Bibliography **124**

NOTATION

Most of the thesis will *try* to stick to a consistent notation, outlined in Tab. 0.1.

TABLE 0.1
Notation guide for the present thesis. Note the, perhaps unusual, distinction between vectors with three-components (3D vectors), denoted with an arrow (e.g. $\vec{x}$) and general vectors, with any number of components, denoted in boldface (e.g. $\boldsymbol{x}$).

Quantity	Explanation	Example(s)
Scalar variables	*Cursive* lower case latin	x, y
3D vectors	*Cursive* lower case latin with an arrow	$\vec{v}$, $\vec{u}$
Normalized 3D vectors	*Cursive* lower case latin with a hat	$\hat{v}$, $\hat{u}$
Vectors	**Bold**, *cursive* lower case latin	$\boldsymbol{v}$, $\boldsymbol{u}$
Normalized vectors	**Bold**, *cursive* lower case latin with a hat	$\hat{\boldsymbol{v}}$, $\hat{\boldsymbol{u}}$
Matrices	*Cursive* **bold** upper case latin	$\boldsymbol{H}$, $\boldsymbol{M}$
Components of vectors	Indices in lower case greek	x_α, v_γ
"Skew symmetrization" of a 3D vector	Transforms a 3D vector into skew symmetric 3×3 matrix, whose action is the cross-product with the vector.	$\mathrm{skew}(\vec{a})\,\vec{b} = \vec{a}\times\vec{b}$
Matrix sub block	One integer pair per index. First number identifies the *start* index of block; second number specifies the *length* of block	$\boldsymbol{M}_{[1,3][2,1]}$
Trace of a matrix		$\mathrm{tr}(\boldsymbol{M})$
Determinant of a matrix		$\det(\boldsymbol{M})$
Positive definite determinant	Product of greater than zero eigenvalues	$\det^+(\boldsymbol{M})$
Direction of a spin	Symbol $\hat{s}$ for the spin, superscript for the index of the spin	$\hat{s}^i$
Component of a spin	Greek subscript for the component	$\hat{s}^i_\alpha$
Heisenberg Hamiltonian	Calligraphic H	$\mathcal{H}$
Spin manifold	Calligraphic S	$\mathcal{S}$
Angle between vectors		$\cos\angle(\boldsymbol{a},\boldsymbol{b}) := \frac{\boldsymbol{a}\cdot\boldsymbol{b}}{\lvert\boldsymbol{a}\rvert\lvert\boldsymbol{b}\rvert}$

ABBREVIATIONS

A small list of abbreviations is provided in Tab. 0.2.

TABLE 0.2
List of abbreviations and acronyms, used in the present thesis.

Abbreviation	Explanation
GPU	Graphics Processing Unit
CPU	Central Processing Unit
LLG	Landau-Lifshitz-Gilbert (equation)
(H)TST	(Harmonic) Transition State Theory
RQ	Rayleigh Quotient
GRQ	Generalized Rayleigh Quotient
PES	Potential energy surface
MEP	Minimum energy path
GNEB	Geodesic nudged elastic band method
DFT	Density functional theory
MMF	Minimum mode following
GAD	Gentlest ascent dynamics

LIST OF FIGURES

1.1 The geometry of an isotropic toroidal Hopfion 23
1.2 Two Hopfions with $Q_{\mathrm{H}} = 6$. 24
1.3 Three dimensional magnetic objects 24
1.4 The Bravais lattice. 27
1.5 Single spin in an external magnetic field 30
1.6 Verification of the dynamical matrix 35
1.7 Accuracy of solvers. 38
1.8 Forward and backward trajectories 39
1.9 Flowchart of Suzuki-Trotter solver 41
1.10 Torque versus iterations in energy minimization. . . . 43

2.1 Minimum energy path illustration 46
2.2 Components of dimer force 51
2.3 Hessian action from finite difference 57
2.4 Benchmark Grassmann L-BFGS MMF 58
2.5 Flowchart Grassmann L-BFGS MMF 59
2.6 Application Grassmann L-BFGS with magnetostatics . 60
2.7 Cosine square ridges 65

3.1 HTST illustration 69
3.2 Convergence of orthogonal velocity. 75
3.3 Lifetime of isolated spin with uniaxial anisotropy . . 79
3.4 Mean first passage time at $2\ \mathrm{K}$ 79
3.5 Shifted log determinant versus shift value 86
3.6 Determinant from the Hutchinson sampler 89
3.7 Transition between a Goldstone mode and a harmonic mode 92
3.8 Spectrum of Hessian eigenvalues at the minimum . . 97

4.1 Parameters with Hopfions as local minima. 103
4.2 Structure of Hopfions and saddle points 104
4.3 Energy barriers for Hopfion collapse 105
4.4 Eigenspectrum of hopfion 107
4.5 Diagonally shifted determinants for Hopfion 112
4.6 Diagonally shifted determinants for saddle point . . . 113
4.7 Determinant contribution to rate pre-factor 114
4.8 Predicted lifetimes 116
4.9 Arrhenius lifetime plot 117

A.1 Color code 123

LIST OF TABLES

0.1 Notation guide 12
0.2 Abbreviations 13

1.1 System parameters for dynamical matrix verification 34

4.1 Parameters for the lifetime calculations of Hopfions in frustrated exchange magnets. The J_i parameter is the strength of symmetric exchange interactions with the i-th neighbor shell in the simple cubic lattice. The characteristic length r_0 and symmetry parameter γ are computed from Eqs. (4.2) and (4.5). 106
4.2 Volumes of zeromodes at the local minimum, as well as the achieved quality factors q, computed from Eq. (4.14). The parameters, in each column, correspond to the ones shown in Tab. 4.1. 110
4.3 Volumes of zeromodes at the saddle points, as well as the achieved quality factors q, computed from Eq. (4.14). The parameters, in each column, correspond to the ones shown in Tab. 4.1 110
4.4 Parameters of Hopfions for lifetime calculation in arbitrary units of J_0. The first three rows correspond to the parameter set, studied by Lobanov & Uzdin [127]. All of these parameters correspond to the same micromagnetic units $a\mathcal{A} = 2.1$, $\mathcal{B}/a = 0.02958(3)$ and $\mathcal{C}/a = 2\mathcal{B}$ 114

INTRODUCTION 1

Magnets and magnetic phenomena lie at the heart of many technologies we rely on today, from data storage devices to sensors, mobility, energy technology and even medical imaging. The key features that make magnets so versatile are the collective behavior of their constituent atomic spins in combination with the dependence of energy on the direction of magnetisation, which can organize the ensemble into a variety of intricate patterns and domains often referred to as spin or magnetisation textures. Understanding and controlling these spin textures at the atomic scale is a primary goal of spintronics – an innovative use-inspired research field that seeks to leverage the spin degree of freedom, rather than (or in addition to) the charge of the electron, for next-generation electronic devices. By harnessing spin-based effects, spintronic devices aim to achieve faster operation speeds, lower energy consumption, higher data storage densities and novel functionalities compared to conventional electronics.

In the search for new ways to store, process, and transmit information, topological solitons have become a central focus. These are localized spin configurations that cannot be continuously deformed into the trivial (uniform) state without passing through an energy barrier or creating singularities. Solitons, in general, emerge in systems that exhibit both nonlinearity and dispersion [1–4]. They appear in a wide range of physics contexts because core equations in different fields often share comparable mathematical structures. For example, the nonlinear Schrödinger equation – fundamental to nonlinear optics – closely parallels the Landau-Lifshitz-Gilbert (LLG) equation in isotropic and uniaxially anisotropic magnetic materials, thus giving rise to analogous soliton phenomena in optics and magnetism[5, 6].

In magnetics, a whole zoo of solitons has been investigated and verified experimentally, such as (i) domain walls (DWs), which are kink-type solitons [7–11], (ii) vortices [12–17], (iii) bubbles [18–22], and (iv) Skyrmions [23–38]. Each of these solitonic textures exhibits unique properties that could be exploited for data processing or other forms of spin manipulation. From a fundamental perspective, exploring these exotic states expands our understanding of how topology and magnetism intertwine, and from a practical viewpoint, it inspires

novel device concepts beyond the traditional thin-film geometries.

Under the time-evolution, as governed by the conservative LLG equation (zero Gilbert damping), both fixed points (static solitons) and limit cycles (dynamic solitons) can be sustained, whereas the non-conservative LLG model [39, 40] only supports static solitons as stable solutions. Dynamical solitons, including vortex-antivortex pairs [16, 41], droplets [42–46], and dynamical skyrmions [47–49], have attracted particular interest, bolstered by experimental findings showing that spin-transfer torque (STT) [50] can offset Gilbert losses in non-conservative magnetic systems, thereby sustaining these dynamic states.

One famous example of a static soliton is the magnetic Skyrmion – a swirling vortex-like arrangement of spins with remarkable stability and small size, which are properties that make Skyrmions very attractive for data storage. In so-called racetrack memories[8, 32, 33, 51, 52], for instance, Skyrmions (also other structures like, for instance, domain walls) can be shuttled along magnetic nanotracks with minimal current, offering a promising path toward high-density, low-energy memory devices. The robust topological protection of Skyrmions helps ensure that they are less prone to being destroyed by defects or thermal fluctuations, making them strong candidates for practical applications. In addition to racetrack memories, other spintronic applications where such topological states (or simpler spin arrangements) can play a role include magnetoresistive random-access memories (MRAMs)[53–62], spin-torque oscillators [63–68], and spin logic devices [69–72]. MRAMs, for example, rely on controlling magnetic states in thin layers, often through spin-transfer or spin-orbit torques, to store information. A high degree of control over individual spins or nanoscopic spin textures is crucial here, and the atomistic Heisenberg Hamiltonian offers a powerful tool for understanding these phenomena at a fine level of detail. By explicitly treating spin interactions among atoms, this model helps identify how microscopic parameters – exchange interactions, anisotropies, Dzyaloshinskii-Moriya interactions, and more – dictate the macroscopic magnetic behavior.

While the Skyrmion is an inherently two-dimensional object, as underscored by its characterization via the two-dimensional winding number, recent years have seen a surge in interest in three-dimensional magnetic structures – some of which are showcased in Fig. 1.3.

The present work is concerned with a soliton from these ranks – the magnetic Hopfion. Magnetic Hopfions are fully three-dimensional, localized magnetization textures whose stability is rooted in topology. Similarly to the Skyrmion, Hopfions are associated with their own topological invariant – the Hopf index [73]. We will denote this index as Q_{H}.

While for the Skyrmion the magnetization points in every possible

direction exactly once, for the Hopfion the magnetization points in any fixed direction on closed spatial loops. These curves are called pre-images. An intuitive description of the Hopf index, is that any two such loops (or pre-images) link exactly Q_{H} times. There is a subtlety related to boundary conditions related to the linking number interpretation, which will be addressed in the more rigorous definition below.

From a more rigorous point of view, the **Hopf index** arises from the third homotopy group

$$\pi_3(S^2) = \mathbb{Z}. \tag{1.1}$$

This means it classifies equivalence classes of continuous maps from the three-dimensional sphere S^3 to the two-dimensional sphere S^2. In the context of **magnetism**, the Hopf index emerges naturally when we consider magnetization fields defined over physical space $\mathbb{R}^3$. To classify the topology of these fields, we compactify physical space by adding a point at infinity, forming a sphere S^3:

$$\mathbb{R}^3 \cup \{\infty\} \overset{\text{compactification}}{\cong} S^3. \tag{1.2}$$

This compactification can be intuitively visualized using a stereographic projection. The magnetization field can then be regarded as a continuous map from this compactified space (S^3) to the space of possible spin directions (S^2), giving rise to a map:

$$S^3 \longrightarrow S^2, \tag{1.3}$$

whose topological classification is precisely measured by the integer-valued Hopf index.

To ensure a well-defined compactification, the magnetization field must approach a constant vector at infinity, i.e., satisfy uniform boundary conditions:

$$\lim_{|x|\to\infty} \mathbf{m}(x) = \mathbf{m}_0. \tag{1.4}$$

This guarantees continuity of the resulting map $S^3 \to S^2$, allowing the classification via the (integer-valued) Hopf index.

In Fig. 1.1 the example of a toroidal Hopfion with Hopf number $Q_{\mathrm{H}} = 1$ is shown – these will be the object of study for this thesis. The general concept of the Hopfion is of course not constrained to such toroidal geometries (in fact non-toroidal Hopfions have been predicted by Rybakov *et al.* [74]), therefore, Fig. 1.2 shows two Hopfions with different geometry but equivalent Hopf index ($Q_{\mathrm{H}} = 6$) side-by-side.

Fig. 1.1 hopefully makes it plausible that the Hopf index cannot always be easily identified "by visual inspection", even if the pre-images have already helpfully been analyzed and colored.

Fortunately, this index can, alternatively, be computed analytically from the magnetization field using the Whitehead formula [75]

$$Q_{\mathrm{H}}[\hat{s}] = -\frac{1}{(8\pi)^2}\int_{\mathbb{R}^3} \vec{F}\cdot\vec{A}\,\mathrm{d}\vec{r}. \tag{1.5}$$

$\vec{F}$ and $\vec{A}$ are auxiliary fields. The solenoidal field $\vec{F}$ is defined as

$$F_\alpha = \varepsilon_{\alpha\beta\gamma}\,\hat{s}\cdot\left(\frac{\partial\hat{s}}{\partial r_\beta}\times\frac{\partial\hat{s}}{\partial r_\gamma}\right) \quad \text{with} \quad \alpha,\beta,\gamma\in\{x,y,z\}.$$

The field $\vec{A}$ is implicitly defined via the equation $\nabla\times\vec{A}=\vec{F}$. Here, $\varepsilon_{\alpha\beta\gamma}$ is the antisymmetric 3D Levi-Civita tensor. Many authors have come up with clever ways to solve this integral numerically, see e.g. Refs. [74, 76–78].

If the boundary condition Eq. (1.4) is removed, it is not possible to define the compactification in the same way, since the limit $|\vec{r}|\to\infty$ cannot be mapped to a single point on S^3. For a conical background, for example, it maps to a line on the sphere [79]. In some cases, it is nonetheless possible to apply the Whitehead formula (1.5), in this different setting, to compute a number and to define pre-images or flux-tubes [79] et cetera. In such a case the Hopf number is no longer integer valued and structures with fractional Hopf numbers can be realized [79, 80]. Such a classification is, naturally, different from the stricter setting of the homotopy group.

Several distinct microscopic ingredients have been shown to stabilize nanoscale hopfions. One route relies on chiral Dzyaloshinskii-Moriya interactions: by taking a twisted skyrmion line and closing it into a loop (for example, in a thin film or nanocylinder with strong interfacial DMI and perpendicular anisotropy), one can nucleate a toroidal hopfion; either in chiral ferromagnets [76, 82–85] or chiral magnets with a conical background [86]. A second class emerges in purely Heisenberg models with competing (frustrated) exchange couplings: When ferromagnetic and antiferromagnetic interactions extend over different neighbor shells, the ground-state phase diagram can admit localized three-dimensional solitons as local minima [74, 77, 87, 88]. Finally, beyond-Heisenberg terms – such as four-spin or biquadratic couplings inspired by Faddeev's original model – introduce higher-order gradient contributions to the micromagnetic energy, which directly lower the cost of three-dimensional twisting and yield metastable hopfions in materials with strong orbital magnetism [89, 90]. Another intriguing class of structures are combined objects, for example Hopfion threaded by Skyrmion/Meron tubes [91–95]. Despite their different origins, each mechanism shares the feature that the effective continuum functional acquires extra spatial-derivative terms that energetically favor a finite-size, knotted $\hat{s}$ field – creating a finite energy barrier for its collapse to the ground state. Besides

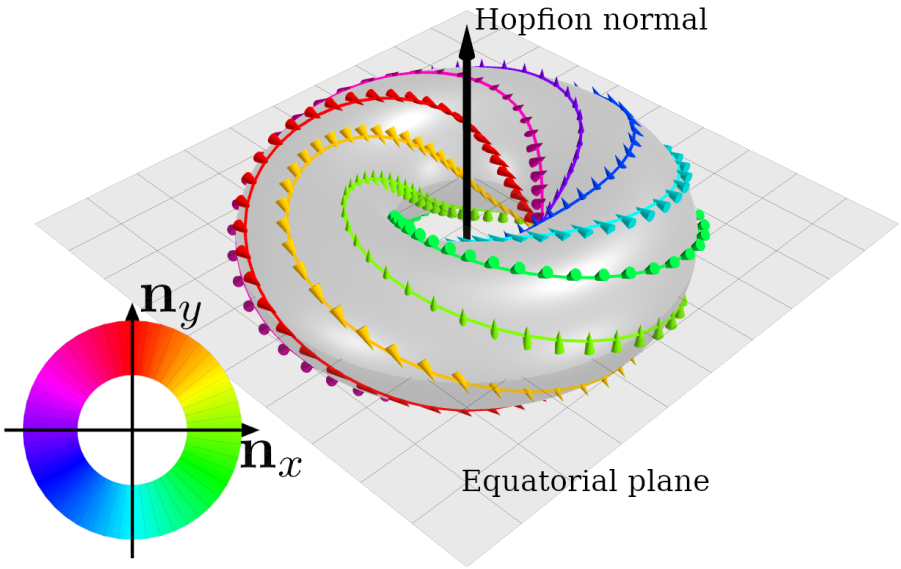


FIGURE 1.1
Illustration of the geometry of an isotropic toroidal Hopfion with unit Hopf invariant. The toroid is formed by the $\hat{s}_z = 0$ isosurface of the spin direction $\hat{s}(\vec{r})$. Further indicated are the equatorial plane and one of its normals passing through the center point of the toroid. The latter is called the Hopfion normal. The colored curves (and cones) are depictions of pre-images, spatial curves along which the spin direction is constant and points into the direction of the cone tip. The color is chosen according to the spin orientation as indicated in the inset. Since this Hopfion has a Hopf invariant of $Q_{\mathrm{H}} = 1$, each pair of pre-images is linked exactly once. Figure adapted from Sallermann *et al.* [81].

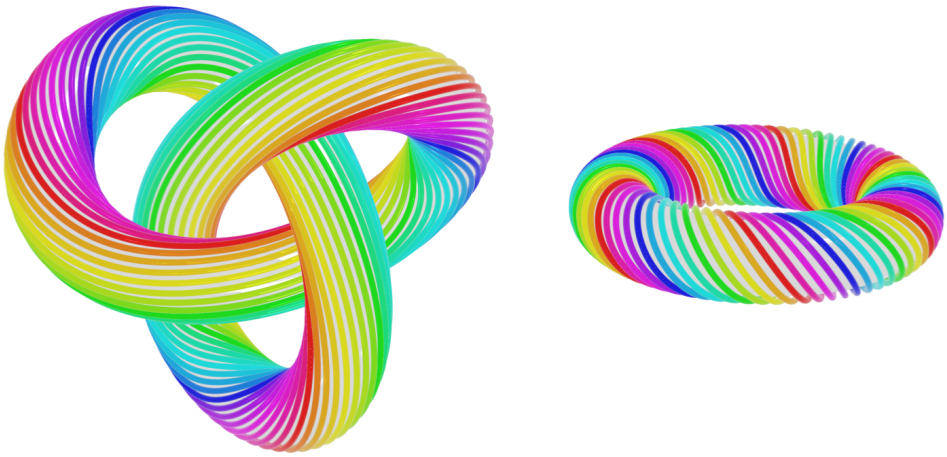


FIGURE 1.2
Illustration of two Hopfions with Hopf invariant $Q_{\mathrm{H}} = 6$. *Left:* Trefoil shaped Hopfions, where each pre-image winds around the trefoil knot thrice (as defined on the basis of the Frenet frame). Here the pre-images are indicated by colored tubes, using the same color code as Fig. 1.1. *Right:* Toroidal Hopfion, where each pre-image winds around the torus six times, thus creating six links per pair of pre-images.

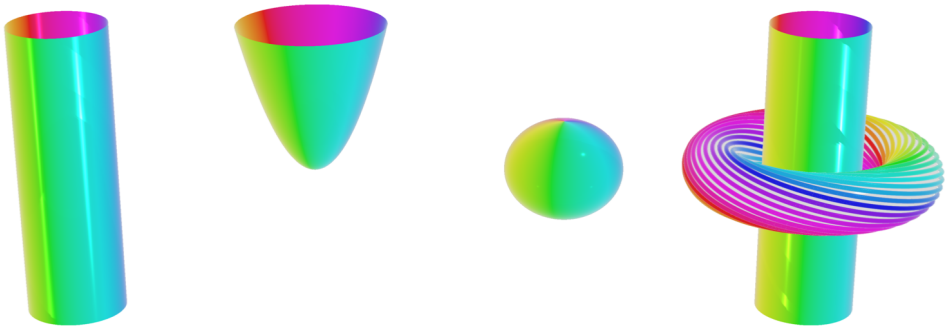


FIGURE 1.3
Commonly encountered objects in three-dimensional magnetism. From left to right: A Skyrmion tube, a chiral bobber, a magnetic globule, a Hopfion on Skyrmion tube.

the question of their stability, the interaction of Hopfions with spin polarized currents [96–103] and to external magnetic fields [93, 104, 105] has been the subject of theoretical studies.

Even though numerical studies and one confined-geometry experiment (see Ref. [106]) provide convincing evidence for Hopfion formation in constrained geometries, an unbound, freely mobile Hopfion remains to be observed in bulk magnets. This gap prompts a key question: *Does the Hopf invariant confer an inherently weaker thermodynamic stability than the two-dimensional Skyrmion charge and is the Hopfion too short-lived for an experimental observation?*

One fundamental limitation to topological protection arises from the discrete nature of the crystal lattice. Strictly speaking, topological invariants apply to a continuously varying field $\hat{s}(\vec{r})$, but real magnets consist of atomic moments $\{\hat{s}_i\}$ localized at sites i. The continuum approximation is valid only when adjacent spins differ by small angles relative to their separation distance. However, as a topological soliton contracts toward the ferromagnetic configuration at the saddle point, this small-angle condition often fails [51, 107, 108]. A related decay mechanism is the nucleation of (paired) Bloch points near these saddle configurations [107]. In three dimensions, the phase-space available for Bloch-point formation is larger than in two, suggesting that hopfions may access more decay routes than Skyrmions. Nevertheless, for geometrically constrained Hopfions (e.g in a cylindrical nanodisk), calculations predict a substantial energy barrier for the conversion into a magnetic toron under an applied field [85], consistent with the observations of Kent *et al.* [106].

Clearly, the emerging interest in Hopfions as metastable topological states is a strong motivations for more research questions than can be addressed in one thesis. Therefore, we will focus on magnets with competing exchange interactions, which are the, seemingly, strongest candidate systems for isolated, mobile Hopfions [74].

From the viewpoint of experimental measurements, it is crucial to have an understanding of the lifetime (governed by the stability against thermal fluctuations) of metastable Hopfions, which depending on parameters could range from femtoseconds to years. Therefore, the overarching goal of this thesis is to understand the relationship between lifetime and exchange parameters and to develop, extend and enhance the necessary methods to perform these calculations.

The remainder of this chapter will serve as a brief introductory guide to common jargon, notation and definitions employed in the subsequent chapters. This includes the definition of the Heisenberg Hamiltonian and the Landau-Lifshitz-Gilbert equation (LLG) as well as its linearization, the geometry of the spin manifold and a few words on energy minimization procedures.

Chapter 2 is concerned with the identification of first order saddle points on the potential energy landscape (as described by the Heisen-

berg Hamiltonian). These points are non-trivial to find in a numerical optimization, but they are of special importance for the study of long time-scale dynamics and transitions.

Chapter 3 deals with the approximation of transition rates and, therefore, lifetimes of topological solitons, within the framework of harmonic transition state theory (HTST). The HTST for atomistic is re-derived in a manner suitable for some additional theoretical modifications of the theory and these new theoretical contributions are, of course, also discussed. They are (i) a treatment of the thermal barrier crossing and (ii) some considerations regarding the contribution of Goldstone modes to the rate-pre-factor.

In Chapter 4, the lifetimes of Hopfions in bulk magnets with competing exchange interactions are investigated using the HTST formalism and saddle points previously identified by the author [81].

Lastly, in Chapter 5 a summary of the thesis is provided and conclusions are drawn.

Chapter A forms the appendix, containing a loose collection of tangentially relevant details, which would have otherwise disrupted the flow of the main text.

1.1 Geometry

The simulations in this work involve a finite number of classical spins (which can be thought of as normalized three dimensional vectors), positioned on a fixed crystalline lattice with a basis.

The lattice is given by translations of a unit cell and for the translation vectors we write

$$\vec{R}_{\alpha\beta\gamma} = \alpha\,\vec{a} + \beta\,\vec{b} + \gamma\,\vec{c} \text{ with } \alpha, \beta, \gamma \in \mathbb{Z} \tag{1.6}$$

where the three Bravais vectors are $\vec{a}$, $\vec{b}$ and $\vec{c}$. Additionally, we assume N_{cell} basis vectors $\vec{\tau}_i$.

At this point it is worthwhile to discuss the space of all possible spin directions, which we shall call the *spin manifold* and denote by the symbol $\mathcal{S}$.

Since the lengths of the spins are constant, this space is a collection of spherical surfaces:

$$\mathcal{S} = \bigotimes_{1}^{N} \mathbb{S}_2 \subset \mathbb{R}^{3N} \tag{1.7}$$

For the purpose of numerical simulations, it is generally favorable to work in the embedding space $\mathbb{R}^{3N}$.Working in the embedding space (as opposed to some internal coordinate system, like a pair of angles for each spin) comes at the cost of having more variables than physical degrees of freedom. The reason for doing so anyways is that

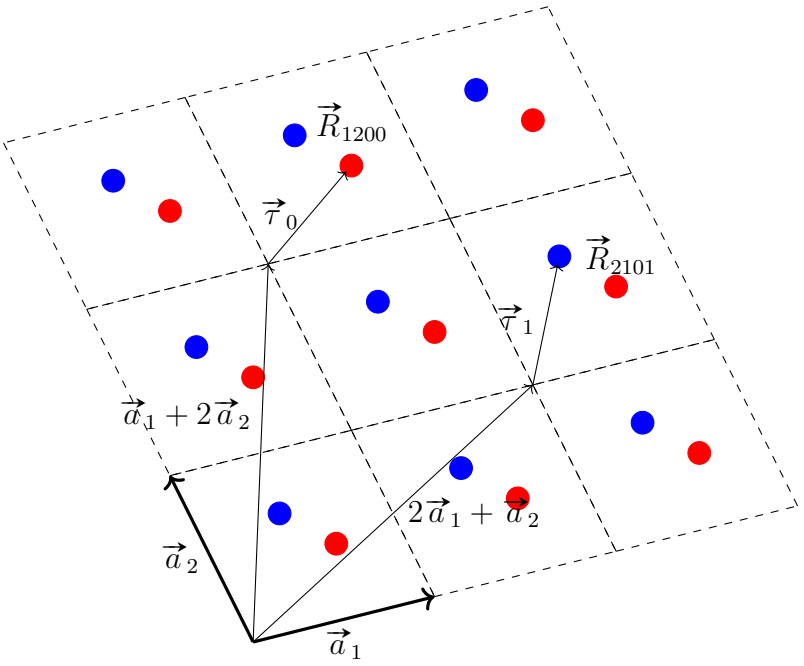


FIGURE 1.4
Example of a two-dimensional geometry with $N_1 = 3$, $N_2 = 3$, $N_3 = 1$, $N_{\text{basis}} = 2$ and $N_{\text{spin}} = 18$. The Bravais vectors $\vec{a}_1$ and $\vec{a}_2$ are indicated by thick black arrows. Each basis cell (outlined by the dashed lines) contains two spins: One at $\vec{\tau}_0$ (blue dots) and another at $\vec{\tau}_1$ (red dots). The position of each atom within the lattice is given by the vector $\vec{R}_{n_1 n_2 n_3 \alpha} = n_1 \vec{a}_1 + n_2 \vec{a}_2 + n_3 \vec{a}_3 + \vec{\tau}_\alpha$.

it eases the use of vectorized linear algebra operations, which are more efficient than the manipulation of non-linear coordinates. In the context of spin dynamics, this approach has been followed (amongst others) by *Müller* [109], but it is also a common wisdom in more general computational settings [110]. Summarily, we represent a point $s \in \mathcal{S}$ either as a sequence of N three dimensional vectors

$$s \doteq \{\hat{s}_i\}_{i=1\ldots N} \quad |\hat{s}_i| = 1 \; \forall i \in [1, N] \tag{1.8}$$

or, occasionally, as a single $3N$ dimensional vector

$$s \doteq \boldsymbol{s} \in \mathbb{R}^{3N} \quad |\boldsymbol{s}_{[3i,3]}| = 1 \; \forall i \in [1, N]. \tag{1.9}$$

The tangent space at the point $s \in \mathcal{S}$ will be denoted by $\mathcal{T}_s$. It is $2N$ dimensional and can be identified with $\mathbb{R}^{2N}$

$$\mathcal{T}_s \sim \mathbb{R}^{2N}. \tag{1.10}$$

A point within the tangent space $p \in \mathcal{T}_s$ is represented either by a $3N$ dimensional vector, with orthogonality constraints

$$p \doteq \boldsymbol{v} \in \mathbb{R}^{3N} \text{ where } \boldsymbol{v}_{[3i,3]} \cdot \boldsymbol{s}_{[3i,3]} = 0 \; \forall i \in [1, N], \tag{1.11}$$

or, simply, by a $2N$ dimensional vector, with an implicit basis for the tangent space $\mathcal{T}_s$

$$p \doteq \boldsymbol{t} \in \mathbb{R}^{2N}. \tag{1.12}$$

We can transform between the two representations (1.12) and (1.11) by using the tangent space basis, expressed as a $2N \times 3N$ matrix $\boldsymbol{T}$

$$\boldsymbol{t} = \boldsymbol{T}\boldsymbol{v}, \tag{1.13}$$

with $\boldsymbol{v} \in \mathbb{R}^{3N}, \boldsymbol{t} \in \mathbb{R}^{2N}$ and $\boldsymbol{T} \in \mathbb{R}^{2N \times 3N}$.

The tangent basis transformation matrix $\boldsymbol{T}$ is block-diagonal with one 2×3 block per spin and depends on the point $s \in \mathcal{S}$, whose tangent space we are interested in. In order for the transformed vector to fulfill the conditions in (1.11), the blocks of $\boldsymbol{T}$ must fulfill

$$\boldsymbol{T}_{[3i,3][2i,2]} \boldsymbol{s}_{[3i,3]} = 0. \tag{1.14}$$

Further, we require orthonormality

$$\left(\boldsymbol{T}_{[3i,3][2i,2]}\right)^T \boldsymbol{T}_{[3i,3][2i,2]} = \boldsymbol{I}_2. \tag{1.15}$$

1.2 The Heisenberg Hamiltonian

The extended Heisenberg Hamiltonian encapsulates the relationship between a configuration of classical spins (which can be thought of as normalized three-dimensional vectors and can therefore be identified

with a point $s \in \mathcal{S}$ on the spin manifold) and the energy. It can include many terms. In the following expression only the most common terms are included:

$$\begin{aligned}\mathcal{H} = &- \sum_i \vec{B} \cdot \vec{m}_i - \sum_{ij} K_j (\hat{K}_j \cdot \hat{s}_i)^2 \\ &- \sum_{\langle ij \rangle} J_{ij} (\hat{s}_i \cdot \hat{s}_j) - \sum_{\langle ij \rangle} \vec{D}_{ij} \cdot (\hat{s}_i \times \hat{s}_j) \\ &- \frac{\mu_0}{4\pi} \sum_{i<j} \frac{3(\vec{m}_i \cdot \hat{r}_{ij})(\vec{m}_j \cdot \hat{r}_{ij}) - \vec{m}_i \cdot \vec{m}_j}{r_{ij}^3},\end{aligned} \tag{1.16}$$

where we define the normalized spin directions $\hat{s}_i$ with associated magnetic moments $\vec{m}_i = \mu_i \hat{s}_i$, which are positioned at $\vec{r}_i$. The first term corresponds to the Zeeman energy of a magnetic moment in an external magnetic field $\vec{B}$, the second term to the magnetic anisotropy with $\hat{K}_j$ being the axes of the uniaxial anisotropies of the basis cell and K_j being the respective strengths. Further terms are the symmetric exchange energy between two spins with strength J_{ij} and the antisymmetric exchange – or Dzyaloshinskii-Moriya – energy as given by the vectors $\vec{D}_{ij}$. The last term is the dipolar energy, due to the finite magnetic dipole moments $\vec{m}_i$. The notation $\langle ij \rangle$ is used to indicate *unique* interaction pairs.

1.3 Equation of motion

The Landau-Lifshitz-Gilbert (LLG) equation, governing the dynamics, of our magnetic systems is[1]

$$\begin{aligned}\frac{\partial \hat{s}_i}{\partial t} = &- \frac{\gamma}{(1+\alpha^2)\mu_i} \hat{s}_i \times \vec{b}_i^{\text{eff}} \\ &- \frac{\gamma\alpha}{(1+\alpha^2)\mu_i} \hat{s}_i \times (\hat{s}_i \times \vec{b}_i^{\text{eff}}),\end{aligned} \tag{1.17}$$

where γ is the gyromagnetic ratio, α is the Gilbert damping parameter, μ_i is the magnetic moment of spin $\hat{s}_i$ and $\vec{b}_i^{\text{eff}}$ is the effective magnetic field felt by that spin $\hat{s}_i$. The effective field $\vec{b}_i^{\text{eff}}$ is composed of a deterministic contribution $\vec{b}_i$, stemming from the Heisenberg Hamiltonian, and a thermal contribution $\vec{b}^{\text{th}}$, such that

$$\vec{b}_i^{\text{eff}} = \vec{b}_i + \vec{b}_i^{\text{th}}(t). \tag{1.18}$$

[1] Note that, for a more impressive looking equation, torques from spin polarized currents could have also been included. For better or worse, these are not relevant to the present work and therefore the LLG equation in its full glory is not on display here (but can be found e.g in Ref. [109] and others).

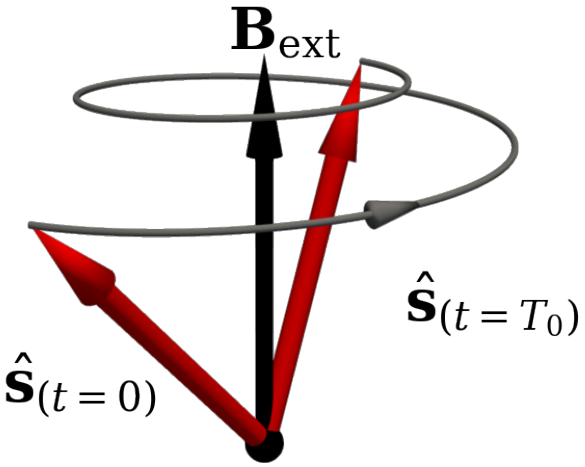


FIGURE 1.5
A single spin in an external magnetic field, evolving in time under the Landau-Lifshitz-Gilbert equation at zero temperature. The direction of the external field is indicated by a black arrow and the direction of the spin at $t = 0$ and a later time $t = T_0$ are shown by red arrows. The trajectory is indicated by a gray line. Please note that the shown counterclockwise rotation corresponds to a negative gyromagnetic ratio (like we find in the example of the spin of an isolated electron). For a positive gyromagnetic ratio, the trajectory would be reversed and a clockwise rotation would occur. The spin will precess around the magnetic field value with a finite precession time τ, determined by the magnetic moment of the spin and the strength of the external field. Due to the finite value of the Gilbert damping, however, its direction will eventually align with the magnetic field, since this configuration minimizes the energy.

The Hamiltonian contribution to the effective field drives the precession and is given by

$$\vec{b}_i = -\frac{\partial \mathcal{H}}{\partial \hat{s}_i}. \tag{1.19}$$

The thermal contribution depends on the diffusion coefficient D, which in turn depends on the Gilbert damping α, the magnetic moment μ_i and the temperature T,

$$\vec{b}^{\,\mathrm{th}}(t) = \sqrt{2D}\,\vec{\xi}\,(t) = \sqrt{\frac{2\alpha k_b T \mu_i}{\gamma}}\,\vec{\xi}\,(t), \tag{1.20}$$

where $\vec{\xi}$ is a noise term with each of its component drawn from independent standard normal distributions.[2] This ensures that $\vec{b}^{\,\mathrm{th}}$ fulfills the dissipation-fluctuation theorem

$$\left\langle \vec{b}^{\,\mathrm{th}}(t) \right\rangle = 0 \tag{1.21}$$

$$\left\langle \vec{b}^{\,\mathrm{th}}(t)\, \vec{b}^{\,\mathrm{th}}(0) \right\rangle = \frac{2\alpha k_b T \mu_i}{\gamma}\delta(t), \tag{1.22}$$

where $\delta(t)$ is the Dirac delta function.

For a visual depiction of the time evolution induced by the LLG equation refer to Fig. 1.5, where the dynamics of a single spin in an external magnetic field are shown.

1.3.1 The linearized thermal LLG equation

Especially in the context of rate theory calculations with harmonic transition state theory (HTST) (which is covered in Chapter 3) the linearization of the LLG equation is important.

Conceptually, we inspect small time dependent deviations $\vec{x}_i(t)$ around fixed spin directions $\hat{s}_i$, giving

$$\vec{n}_i(t) = \hat{s}_i + \vec{x}_i(t), \tag{1.23}$$

where $x \in \mathcal{T}_s$ is an element of the tangent space of the spin manifold at the point $s \in \mathcal{S}$, and, therefore, $\hat{s}_i \cdot \vec{x}_i = 0$.

In the LLG equation this leads to

$$\begin{aligned}
\partial_t \vec{n} &= -\gamma' \vec{n} \times \vec{b}^{\,\mathrm{eff}} - \gamma' \alpha\, \vec{n} \times \vec{n} \times \vec{b}^{\,\mathrm{eff}} \\
\partial_t \vec{x} &= \underbrace{-\gamma'(\hat{s} + \vec{x}) \times \vec{b}^{\,\mathrm{eff}}}_{\partial_t \vec{x}^{\,\mathrm{P}}} \underbrace{-\gamma' \alpha (\hat{s} + \vec{x}) \times \left[(\hat{s} + \vec{x}) \times \vec{b}^{\,\mathrm{eff}} \right]}_{\partial_t \vec{x}^{\,\mathrm{D}}},
\end{aligned} \tag{1.24}$$

[2] Meaning zero mean and unity variance.

where, for notational convenience, we dropped the subscript i and defined

$$\gamma' = \frac{\gamma}{(1+\alpha^2)\mu_i}. \tag{1.25}$$

Further, we split the equation into a precessional part $\partial_t \vec{x}^{\mathrm{P}}$ and a damping part $\partial_t \vec{x}^{\mathrm{D}}$. For the precessional part we get

$$\partial_t \vec{x}^{\mathrm{P}} = -\gamma' \left(\hat{s} \times \vec{b}^{\mathrm{eff}} + \vec{x} \times \vec{b}^{\mathrm{eff}} \right), \tag{1.26}$$

and the damping contribution is

$$\begin{aligned}
\partial_t \vec{x}^{\mathrm{D}} &= -\gamma'\alpha(\hat{s} + \vec{x}) \times \Big[(\hat{s} + \vec{x}) \times \vec{b}^{\mathrm{eff}} \Big] \\
&= -\gamma'\alpha \Big[\hat{s} \times (\hat{s} \times \vec{b}^{\mathrm{eff}}) + \hat{s} \times (\vec{x} \times \vec{b}^{\mathrm{eff}}) \\
&\qquad + \vec{x} \times (\hat{s} \times \vec{b}^{\mathrm{eff}}) + \vec{x} \times (\vec{x} \times \vec{b}^{\mathrm{eff}}) \Big] \\
&= -\gamma'\alpha \Big[(\hat{s} \cdot \vec{b}^{\mathrm{eff}})\hat{s} - (\hat{s}^2)\, \vec{b}^{\mathrm{eff}} \\
&\qquad + (\hat{s} \cdot \vec{b}^{\mathrm{eff}})\vec{x} - (\hat{s} \cdot \vec{x})\, \vec{b}^{\mathrm{eff}} \\
&\qquad + (\vec{x} \cdot \vec{b}^{\mathrm{eff}})\hat{s} - (\vec{x} \cdot \hat{s})\, \vec{b}^{\mathrm{eff}} \\
&\qquad + \mathcal{O}(\vec{x}^2) \Big] \\
&= -\gamma'\alpha \Big[-\vec{b}^{\mathrm{eff}} + (\hat{s} \cdot \vec{b}^{\mathrm{eff}})\vec{x} + \mathcal{O}(\vec{x}^2) \Big],
\end{aligned} \tag{1.27}$$

where, for the last step, we used the vector identity

$$\vec{a} \times (\vec{b} \times \vec{c}) = (\vec{a} \cdot \vec{c})\, \vec{b} - (\vec{a} \cdot \vec{b})\, \vec{c}$$

and the fact that $\vec{x} \cdot \hat{s} = 0$.

The dynamical matrix

A further approximation that can be made to (1.24) is to approximate the energy by a Taylor series up to second order and to subsequently drop terms of the order $\mathcal{O}(\vec{x}^2)$ as well as the stochastic noise term. This recasts the LLG equation into the form of a matrix-vector multiplication and gives rise to the so-called dynamical matrix (or velocity matrix in some contexts).

The dynamical matrix can be derived by plugging

$$\vec{b}_i^{\mathrm{eff}} = -\frac{\partial}{\partial \hat{s}_i}\mathcal{H} = -\vec{g}_i - \sum_j \boldsymbol{H}^{ij}\vec{x}_j, \tag{1.28}$$

into (1.24). Note that the gradient $\vec{g}_i$ and the Hessian $\boldsymbol{H}^{ij}$ live on the spin-manifold and are therefore different from the embedding space quantities. Namely, the gradients are projected orthogonally to the spin directions

$$\vec{g}_i \to \vec{g}_i - (\vec{g}_i \cdot \hat{s}_i)\hat{s}_i \tag{1.29}$$

and the Hessian acquires a correction on the diagonal

$$\boldsymbol{H}^{ij} \to \boldsymbol{H}^{ij} - (\vec{g}_i \cdot \hat{s}_i)\boldsymbol{I}_3. \tag{1.30}$$

We start with the precessional contribution:

$$\begin{aligned}
\partial_t \vec{x}_i^{\,\mathrm{P}} &= -\gamma' \left[(\hat{s}_i + \vec{x}_i) \times \left(-\vec{g}_i - \sum_j \boldsymbol{H}^{ij} \vec{x}_k \right) \right] \\
&= \gamma' \left[(\hat{s}_i + \vec{x}_i) \times \vec{g}_i + \sum_j \hat{s}_i \times \boldsymbol{H}^{ij} \vec{x}_j \right] \\
&= \vec{v}_i^{\,\mathrm{P}} + \sum_j \boldsymbol{V}^{\mathrm{P}}|^{ij} \vec{x}_j,
\end{aligned} \tag{1.31}$$

where in the last line we defined a constant offset vector $\vec{v}_i^{\,\mathrm{P}}$ and the precessional contribution to the dynamical matrix $\boldsymbol{V}^{\mathrm{P}}|^{ij}$. Explicitly, these two quantities are

$$\vec{v}_i^{\,\mathrm{P}} = \gamma' \hat{s}_i \times \vec{g}_i \tag{1.32}$$

and

$$\boldsymbol{V}^{\mathrm{P}}|^{ij} = \gamma' \left[\mathrm{skew}(\hat{s}_i) \boldsymbol{H}^{ij} - \delta_{ij} \,\mathrm{skew}(\vec{g}_i) \right], \tag{1.33}$$

where the skew operator maps from $\mathbb{R}^3$ to $\mathbb{R}^{3\times 3}$ and is defined such that

$$\mathrm{skew}(\vec{a})\,\vec{b} := \vec{a} \times \vec{b} \tag{1.34}$$

or, equivalently,

$$\mathrm{skew}(\vec{a}) := \begin{pmatrix} 0 & -a_3 & a_2 \\ a_3 & 0 & -a_1 \\ -a_2 & a_1 & 0 \end{pmatrix}. \tag{1.35}$$

Repeating the process for the damping contribution results in

$$\begin{aligned}
\partial_t \vec{x}_i^{\,\mathrm{D}} &= -\gamma' \alpha \left[-\vec{b}_i^{\,\mathrm{eff}} + (\hat{s}_i \cdot \vec{b}_i^{\,\mathrm{eff}}) \vec{x}_i \right] \\
&= -\gamma' \alpha \left[\vec{g}_i + \sum_j \boldsymbol{H}^{ij} \vec{x}_j - (\hat{s}_i \cdot \vec{g}_i) \vec{x}_i \right] + \mathcal{O}(x^2) \\
&= \vec{v}_i^{\,\mathrm{D}} + \sum_j \boldsymbol{V}^{\mathrm{D}}|^{ij} \vec{x}_j,
\end{aligned} \tag{1.36}$$

with

$$\vec{v}_i^{\,\mathrm{D}} = -\gamma' \alpha \, \vec{g}_i \tag{1.37}$$

and

$$\boldsymbol{V}^{\mathrm{D}}|^{ij} = -\gamma' \alpha \left[\boldsymbol{H}^{ij} - \delta_{ij} (\hat{s}_i \cdot \vec{g}_i) \boldsymbol{I}_3 \right]. \tag{1.38}$$

An attentive reader, comparing to Müller [109], may notice that the expressions for the dynamical matrix, given in equations (1.64)

and (1.67) of Ref. [109], are different from the ones derived here. For a verification of the equations, presented here, see Fig. 1.6.

Finally, we remark on a subtlety of applying the linearized LLG to non-stationary points.[3] In such a case the loss of orthogonality between $\vec{x}_i$ and $\hat{s}_i$ is linear in $\vec{x}_i$ as is easily seen by inspecting, e.g the precessional contribution[4]

$$\begin{aligned} \hat{s}^T \partial_t \vec{x}^{\,\mathrm{P}} &= \hat{s}^T \gamma' (\hat{s} \times \vec{b}^{\,\mathrm{eff}} + \vec{x} \times \vec{b}^{\,\mathrm{eff}}) \\ &= \gamma' \left[\hat{s}^T (\vec{x} \times \vec{g}) + \mathcal{O}(x^2) \right] \end{aligned} \tag{1.39}$$

When applying the linearized LLG *around a stationary point*, the loss of orthogonality is a second order effect (meaning the only terms of $\propto x^n$, with $n > 2$, contribute), however, and therefore irrelevant to the dynamical matrix. In Chapter 3, we will only linearize the LLG around such stationary points. We shall, therefore, not worry about this subtlety in this work.

TABLE 1.1
System parameters used for the verification of the dynamical matrix in Fig. 1.6. The system consists of two spins, separated along the x-axis.

Quantity	Value	Unit
α	0.3	-
J_{ij}	1	meV
$\vec{D}$	$\hat{e}_x$	meV
μ_1	1.3	μ_B
$\vec{B}$	$(5, 0, 0)$	T
$\vec{K}$	$(0, 0, 0.5)$	meV
$\vec{r}_1$	$(0, 0, 0)$	Å
$\vec{r}_2$	$(1, 0, 0)$	Å

1.4 Computing the time-evolution of the LLG equation

Solving the LLG equation numerically, and thus evolving a spin system in time, is commonly achieved by specialized prediction-correction type methods, like Depondt's method [111], the "semi-implicit method B" by Mentink *et al.* [112], or, even general purpose

[3] Meaning the gradient does not vanish at the point of linearization, and therefore $\vec{g} \neq 0$ in (1.28).
[4] The same will happen in the damping contribution.

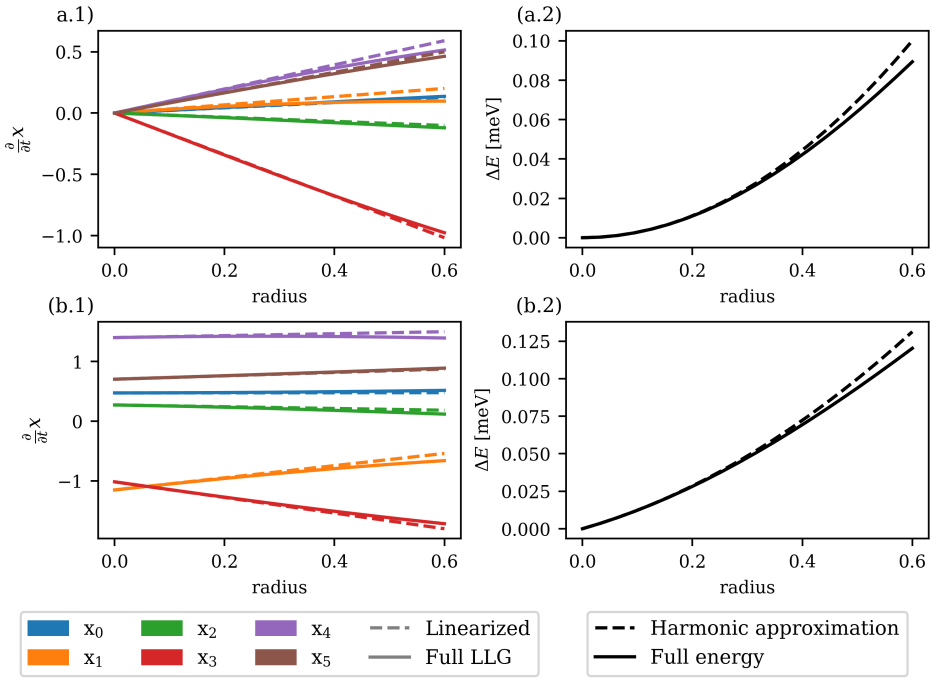


FIGURE 1.6

Verification of the dynamical matrix in a system with two spins, including exchange interaction, DMI, uniaxial anistropy and a magnetic field and damping. For details of the system parameters see Tab. 1.1. The top two plots show the linearization around a local energy minimum ($\hat{s}_1 = (0.289, 0.277, 0.916)$, $\hat{s}_2 = (0.289, -0.277, 0.916)$). The subplot (a.1) shows the time dependence of the deviation of all six spin components in the embedding space [continuously labeled as x_1 to x_6, adhering to the notation of (1.24)], where the solid lines correspond to actual simulations with the full dynamics (where the values x_i have been found by computing the differences of components from the initial value) and the dashed lines correspond to the prediction by the dynamical matrix. Note that x_0/x_1 and x_4/x_5 are nearly on top of each other. The right plot (a.2) shows the energy dependence which is harmonic, with a vanishing linear contribution (as is expected of a local minimum). In the bottom row the same has been repeated for a non-stationary point [$\hat{s}_1 = (0.186, 0.297, 0.937)$ and $\hat{s}_2 = (0.517, -0.054, 0.854)$]. This time, the linear contribution to the energy dependence is clearly visible, since it is not a stationary point.

methods (coupled with re-normalizing each spin after every iteration) like Heun's method [113] and Runge-Kutta methods. We will not go into detail of any of these methods here – small reviews can be found in Refs. [109, 114].

The hallmark of the specialized methods is that they try to incorporate information about the equation being solved into the update step (as opposed to being formulated simply on the assumption of a general objective function, with gradient information, like the "general" methods). For example, Depondt's method updates each spin in the system, based on the trajectory expected from the precessional contribution of the LLG. The advantage of such methods is that they fulfill conservation laws in *special cases*. These conservation laws may for example be the conservation of spin length (making the renormalization step after each iteration unnecessary[5]), energy[6] or total magnetic moment.[7] A disadvantage is that these special cases are often removed from the actual systems being simulated and that the physical intuition built into these methods does not result in an increased accuracy of the trajectory of interest. On the other hand, simulations over very long time scales may still benefit from being constrained in this way – although in such cases results may be considered unreliable in any case.

1.4.1 Choosing a time step

Choosing a timestep for the integration of the LLG equation is far from trivial.[8] This is especially the case in systems where the analytical trajectory is not known a priori, which is practically every system studied numerically.

The main complication stems from the fact that, in order to test different time steps for their accuracy, a reference solution is required. Here, we will describe a method to circumvent this complication and to determine optimal time steps in arbitrary systems:

We take inspiration from the Richardson extrapolation method [116]. Let us assume an analytical solution of the LLG equation is given by

$$\hat{s}_i(t) \text{ with } t \in [0, T] \; \forall \; i \in [1, N], \tag{1.40}$$

and denote the solution, via a discretized scheme with timestep Δt,

[5] Although, due to numerical instabilities it may still necessary to re-normalize the spin directions, especially when running simulations in single precision, like it is common on GPU hardware.

[6] Naturally, only in the absence of Gilbert damping.

[7] As expected in systems with only isotropic exchange interactions and zero damping

[8] Please note that this section has been adapted from Sallermann *et al.* [115]

by

$$\hat{s}_i(t_j|\Delta t) \text{ with } t_j = j\Delta t. \tag{1.41}$$

Now, we try to compute the error ε at the endpoint of the trajectory ($t = T$), while keeping only the term of lowest polynomial order

$$\hat{s}_i(t_j|\Delta t)_\alpha = \hat{s}_i(t_j)_\alpha + \varepsilon_{i\alpha} \tag{1.42}$$

$$\approx \hat{s}_i(t_j)_\alpha + k\Delta t^n + \mathcal{O}(\Delta t^{n+1}), \tag{1.43}$$

where $\alpha \in \{x, y, z\}$, n is the integer order of the numerical scheme and k is a constant pre-factor to the error term.

By generating trajectories with three different time steps ($2\Delta t$, Δt and $\Delta t/2$) and neglecting all errors of higher order than n, we can solve for the three unknowns k, n and $\hat{s}_i(t)_\alpha$, resulting in

$$n = \log_2 \left(\frac{\hat{s}_i(T|2\Delta t)_\alpha - \hat{s}_i(T|\Delta t)_\alpha}{\hat{s}_i(T|\Delta t)_\alpha - \hat{s}_i\left(T|\Delta t/2\right)_\alpha} \right) \tag{1.44}$$

$$k = \frac{1}{\Delta t^n} \frac{\hat{s}_i(T|2\Delta t)_\alpha - \hat{s}_i(T|\Delta t)_\alpha}{2^n - 1}. \tag{1.45}$$

Note: Of course, frequently, we are already aware of the order n of the integration scheme. In such cases the error estimate can be obtained from only two trajectory samples. It is nonetheless not a bad idea to verify our assumptions about the order of a given integration scheme, especially since numerical instabilities can, in practice, lead to a different behavior than would be expected a priori.

Consequently, we obtain an order $\mathcal{O}(\Delta t^{n+1})$ estimate for the maximum error over all spin components:

$$\varepsilon(\Delta t) = \max_{i,\alpha}(\varepsilon_{i\alpha}) \approx \max_{i,\alpha}(k\Delta t^n) + \mathcal{O}(\Delta t^{n+1}). \tag{1.46}$$

In Fig. 1.7 we verify this scheme by comparing it with exact errors, obtained via the analytical trajectory of a single spin in an external field, and observe that the error estimates found by the extrapolation and the analytical trajectory are in good agreement.

The advantage of the proposed extrapolation method, in comparison to generating a reference trajectory with extremely low time steps, is that it is (i) more time efficient and (ii) less sensitive to numerically induced errors occurring in update schemes with extremely low time steps. A further application of the extrapolation method is to find optimal time steps for a given system and integrator.

1.4.2 Time reversibility

In this last subsection[9] of the introduction, we shall address a (perhaps) more esoteric property, which might be desirable in a numerical

[9] Please note that this section has been adapted from Sallermann *et al.* [115]

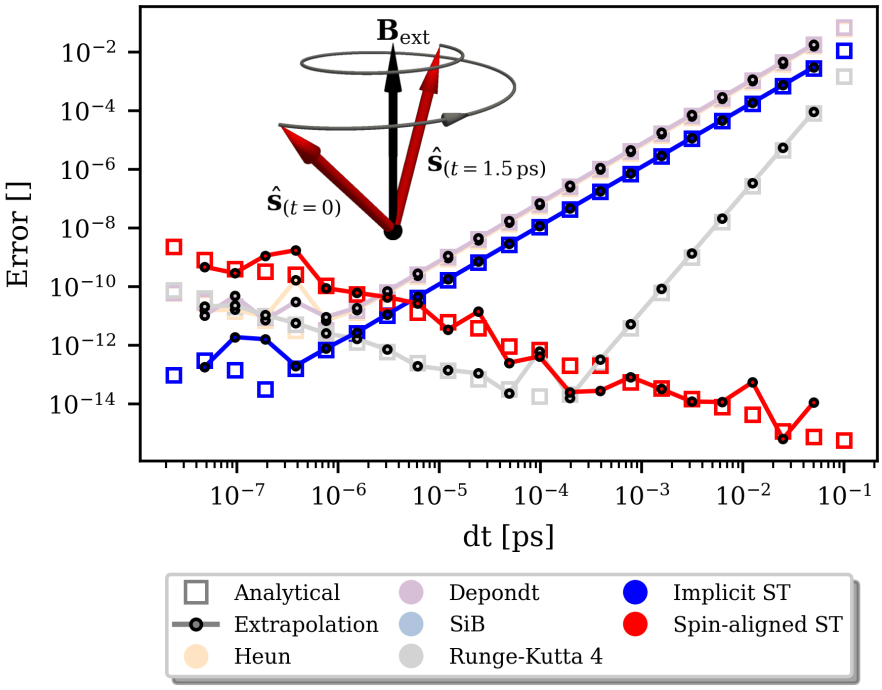


FIGURE 1.7
Accuracy over timestep for different solvers in the case of an isolated, damped spin in an external magnetic field. The field has been chosen such that the precession time is exactly $1\,\text{ps}$. Different colors, correspond to different solvers. Continuous lines with dots denote errors found via the extrapolation method, while hollow squares denote errors found via the analytical solution of the trajectory. The inset illustrates the trajectory. The second order Suzuki-Trotter (blue) shows similar performance to the second order predictor-corrector schemes, while, unsurprisingly, being worse than the fourth order Runge-Kutta solver (gray). This figure has been taken from the preprint by Sallermann *et al.* [115].

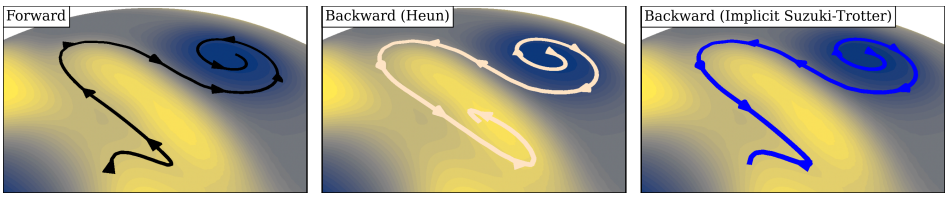


FIGURE 1.8
Illustration of forward and backward time trajectories calculated using the Heun solver and the Suzuki-Trotter decomposition within a simple two-dimensional energy landscape composed of several anisotropic Gaussian contributions. The two forward trajectories (black, left panel) shown in this illustration are indistinguishable. In contrast, the backward trajectories display a notable difference: the Heun solver (middle panel, beige) deviates from the forward trajectory and fails to return to the initial configuration, whereas the Suzuki-Trotter solver accurately reproduces the initial configuration. Figure from the preprint by Sallermann *et al.* [115].

integration of the LLG equation – time reversibility.

First, a definition is in order. In this context, time reversibility refers to the property that knowing the direction of all spins at a time t_2, should allow one to deduce the direction of all spins at an earlier time $t_1 < t_2$. We can accomplish such a feat by numerically simulating the trajectory going *backwards in time* by inverting the direction of the torques. However, different solvers are able to reconstruct these trajectories with varying levels of success. For an illustration, consult Fig. 1.8 which shows a situation where a trajectory, going forward in time (shown in black), is being reconstructed from a point near a local minimum, with two different solvers. The first solver (with a beige time-reversed trajectory) is the aforementioned Heun solver, while the second solver is the so-called Implicit Suzuki-Trotter solver. We have, so far, not mentioned this solver, we shall however briefly discuss it briefly below. For now, it suffices to say that it can, by construction, reconstruct the forward trajectory up to numerical precision.

The reason for bothering with time reversibility, in the first place, is that it enables the computation of certain corrections to the harmonic transition state theory (namely recrossing corrections) by initiating trajectories in the transition state and evolving them backwards in time to verify if they actually originate from the initial minimum (as assumed by transition state theory). There are *several* problems when attempting this in practice, not least of which is that the time reversibility, as described in this section, is actually not very applicable with finite Gilbert damping since then trajectories contract in the configuration space and become, numerically speaking, less and less

reversible as the trajectory evolves.[10] In the extreme case where the trajectory ends in a local minimum it is, of course, not reversible at all since it could have originated from a rather arbitrary set of points in the vicinity of the minimum. At zero Gilbert damping, the connection to lifetime calculations, however, becomes less clear since a finite damping is required for the Langevin-style thermostat of the stochastic LLG equation (1.17). Ignoring these issues for the moment, we can still find a time-reversible integration scheme at zero Gilbert damping.

The usual predictor-corrector methods perform adequately well as long as $t_2 - t_1$ is a relatively small time span, but after not too long the trajectory evolved back is different from the forward trajectory (as is on display in Fig. 1.8).

One way to achieve better time-reversibility is splitting the update of all spin directions by a time step Δt into *two* series of single spin updates: First, each spin is evolved by $\Delta t/2$ traversing over the spins in some arbitrary order, and then each spin is updated a second time (again by $\Delta t/2$) but in reverse order. Crucially, the effective magnetic field is recomputed after each update of a single spin.[11] This corresponds to a second order Suzuki-Trotter decomposition. A flowchart, showing this algorithm can be found in Fig. 1.9. More details can be found in Ref. [115]. The remaining question is how to update the single-spins in a time-reversible manner. In order to do this, an implicit midpoint scheme can be used where the spin is updated on the basis of the field at the midpoint:

$$\hat{s}_i\left(t + \frac{\Delta t}{2}\right) \approx \hat{s}_i(t) + \frac{\Delta t}{2}\vec{F}_i\left(\frac{\hat{s}_i(t) + \hat{s}_i\left(t + \frac{\Delta t}{2}\right)}{2}\right). \tag{1.47}$$

where $\boldsymbol{F}_i$, depends on the effective magnetic field and is defined exactly such that

$$\frac{\mathrm{d}\hat{s}_i}{\mathrm{d}t} = \vec{F}_i(\hat{s}_1 \ldots \hat{s}_N) \tag{1.48}$$

is equivalent to the LLG equation (1.17).

[10] In some sense this situation is analogous to the condition number of a matrix and its inverse being anti-proportional.

[11] This is drastically different from the approach taken by the predictor-corrector methods, where the magnetic field is calculated in bulk either before or after updating all of the spins by a time Δt. In the Suzuki-Trotter decomposition we end up computing the magnetic field at many intermediate configurations, which cannot be clearly associated to either t or $t + \Delta t$. Since we only ever change one spin, this update of the magnetic field can be implemented in a reasonably efficient way, but a certain overhead, compared to the "bulk computation" is unavoidable – especially when including long-range magnetostatic interactions.

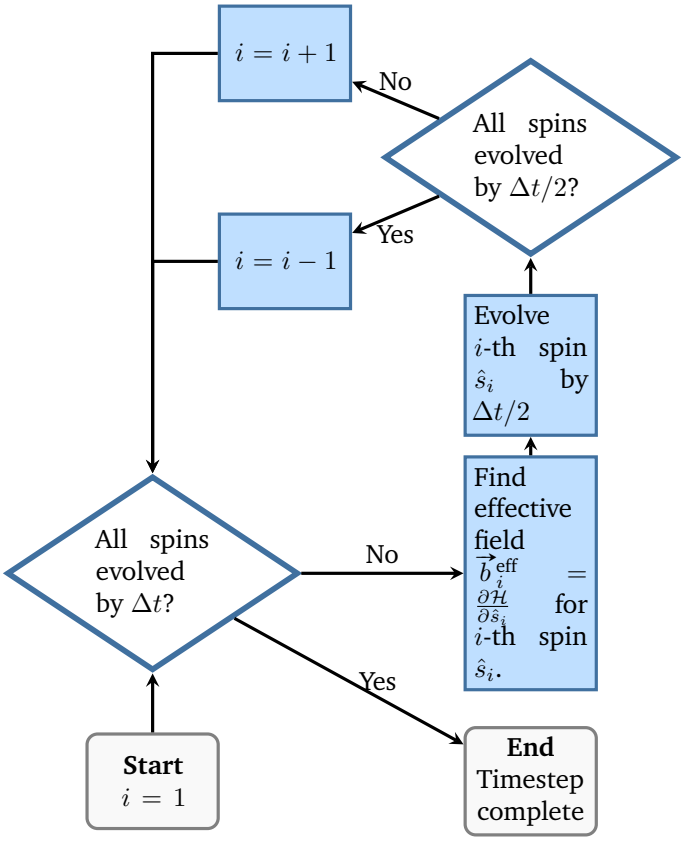


FIGURE 1.9
Flowchart of the second order Suzuki-Trotter decomposition applied to the LLG equation.

Since Eq. (1.47) is symmetric under the substitutions

$$\begin{aligned} \Delta t &\to -\Delta t \\ \hat{s}_i\left(t + \frac{\Delta t}{2}\right) &\to \hat{s}_i\left(t\right) \\ \hat{s}_i\left(t\right) &\to \hat{s}_i\left(t + \frac{\Delta t}{2}\right), \end{aligned}$$

it is time-reversible.

1.5 Energy Minimization

In atomistic spin dynamics simulations, accurately identifying metastable states is crucial for understanding the magnetic properties and behaviors of materials. As discussed in preceding sections, a critical constraint in atomistic spin dynamics is the requirement for constant spin length. This constraint ensures that the magnitude of each spin vector remains unchanged, preserving the physical integrity of the system.

Mathematically, this is expressed as

$$|\hat{s}_i| = 1 \tag{1.49}$$

where $\hat{s}_i$ is the direction of the spin vector at site i.

This constraint must be satisfied throughout the minimization process to ensure that the energy landscape is accurately navigated and the physical properties of the metastable states are preserved.

The most basic way to minimize the energy of a spin configuration is to simulate its dynamics under the LLG equation with finite Gilbert damping and zero temperature (potentially even disabling the precession contribution to the LLG) – over time the system will relax into a local energy minimum. Such approaches are very common, but tend to be inefficient. This inefficiency stems from the fact that such methods do not make use of the fact that the energy minimization allows arbitrary (even unphysical) intermediate steps, which can lead us to the energy minimum much faster than damped dynamics.

One method with improved efficiency is the velocity projection (VP) method [114, 117], which allows the minimization to increase its step size if subsequent update directions have significant overlap.

For this work, however, we have implemented the Limited-memory Broyden-Fletcher-Goldfarb-Shanno (L-BFGS) method [118], coupled with a coordinate transformation which inherently preserves Eq. (1.49), in Spirit [114, 119]. The L-BFGS method is a quasi-Newton method for solving unconstrained optimization problems. This method is very similar to the one described by Ivanov *et al.* [120].

It is particularly well-suited for large-scale problems due to its efficiency in both memory usage and computational cost. L-BFGS approximates the Hessian matrix (which represents the second-order partial derivatives of the objective function) using information from previous iterations. This approximation is updated iteratively without the need to store the full Hessian matrix, making it memory-efficient. The key steps in L-BFGS include initialization of spin configurations and gradients, iterative updates using the gradient of the energy function and a search direction computed from the approximated Hessian, and the use of correction pairs that represent the curvature information of the objective function. The algorithm iterates until convergence criteria, such as gradient norm tolerances, are met. Details can be found in most numerical optimization textbooks [121, 122] and, for the coordinate transform, in Ivanov *et al.* [123].

For a comparison of the VP method and the L-BFGS method as implemented in Spirit, see Fig. 1.10. Evidently, the L-BFGS solvers are much more performant for this particular system. We have found that this assertion seems to hold true for a wide class of systems as well. The wall time overhead, due to the more complex update scheme in the L-BFGS algorithm, which is not depicted in Fig. 1.10, seems to

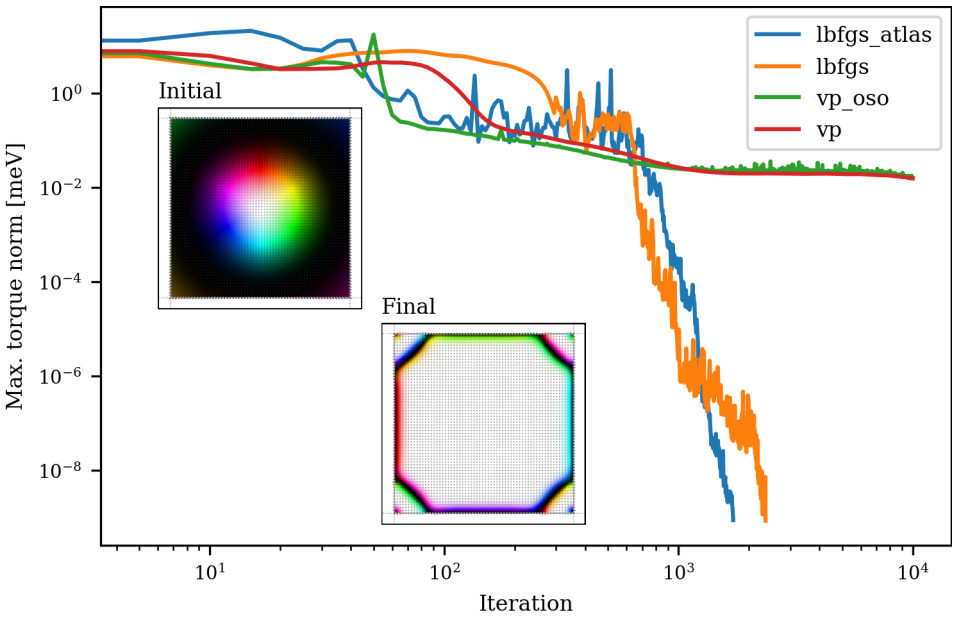


FIGURE 1.10
The maximum torque over all spins versus the number of steps in an energy minimization simulation of a rather arbitrary system. The two L-BFGS solvers differ only in the type of coordinate transform, where the orange line ("lbfgs") refers to the transform as described by Ivanov *et al.* [123] and the blue line ("lbfgs_atlas") uses stereographic coordinates instead. The velocity projection solver is represented in two variants as well. One (green, "vp_oso") uses the coordinate transform by Ivanov *et al.* [123], the other uses no coordinate transform, but re-normalizes the spin directions after each step.

be negligible in face of the drastically reduced number of required iterations.

SADDLE POINT SEARCHES 2

Potential energy surfaces (PES), over a suitable coordinate space, provide a versatile framework for interpreting the dynamics and stability of complex systems. In the field of atomistic spin models the PES is an invaluable tool. Here, the energy is mapped as a function of the spin configurations governed by the extended Heisenberg Hamiltonian. The PES reveals not only the stable, low-energy states but also the critical configurations – saddle points – that delineate the pathways for transitions. Such transitions are analogous to chemical reactions, with the decay of a magnetic soliton occurring as the system overcomes an energy barrier defined by these saddle points.

The concept of using energy surfaces to understand transition mechanisms originated in chemical kinetics. Early in the 20th century, researchers like Eyring [124] and Wigner [125] advanced the ideas behind transition state theory, which posits that the highest-energy point along a reaction coordinate (the activated complex) is central to determining reaction rates. Although these initial studies were rooted in chemistry, the underlying principles have found a natural extension in magnetism. In magnetic systems, the idea of a PES became particularly relevant with the study of nontrivial spin configurations. Pioneering theoretical work, such as that by Bogdanov & Yablonskiui [126], began to reveal that competing interactions – like the Dzyaloshinskii-Moriya term – could stabilize vortex-like structures in magnets. Over time, the analogy between chemical reaction pathways and the decay of topological magnetic solitons has been developed further and many applications can be found in the literature [51, 108, 127–144].

In any system described by a PES, saddle points are defined as stationary points where the gradient vanishes, but the curvature [as quantified by the eigenvalues of the matrix of second derivatives (the Hessian)] is mixed. For a first-order saddle point, there is exactly one direction in which the curvature is negative – this unstable direction corresponds to the decay or transition path.

The Hamiltonian under consideration typically includes contributions from exchange interactions, magnetic anisotropy, the Dzyaloshinskii-Moriya interaction, and Zeeman terms. The interplay

among these contributions leads to a rich PES landscape where complex magnetic configurations, such as Skyrmions, reside in local energy minima. The decay process of these solitons, driven by thermal fluctuations, is therefore understood in terms of overcoming an energy barrier characterized by a saddle point. As a result, the stability and lifetime of these magnetic structures are directly related to the height of the energy barrier and the curvature of the PES in the vicinity of the saddle point.

Techniques, originally devised for exploring chemical reaction pathways, have been adapted to study magnetic transitions [117, 145]. For example, methods like the nudged elastic band (NEB) [146, 147] and its variants have proven effective in tracing the minimum energy paths between distinct magnetic states. In magnetic systems, specialized adaptations such as the geodesic nudged elastic band (GNEB) method [117] are employed to navigate the curved configuration space inherent to spin systems.

Saddle point search algorithms can be divided into two broad categories: *Single-ended saddle point searches* and double-ended saddle point searches. In single-ended saddle point searches typically work based on local information in one point of the configuration space[1] and try to move this one point towards a saddle point. These methods can be employed to explores saddle points, and therefore possible transitions, around a local minimum. The minimum mode following (MMF) method is an example of such an algorithm. *Double-ended saddle point searches* on the other hand work on a multitude of points in the configuration space, interpolating between the two "ends" of a chain of states. They try to find the saddle point as an energy maximum along this chain of states. An example is the (G)NEB method.

A few of these methods will be discussed in the following sections.

2.1 The geodesic nudged elastic band method

In this section,[2]the GNEB method is briefly revised. This method is a scheme for finding minimum energy paths (MEPs) between minima corresponding to initial and final states [117] – and hence it is a double-ended saddle point search method. A minimum energy path connects two minima on an energy landscape, while minimizing the

[1] Optimization routines which maintain a history of past updates like the L-BFGS solver muddy this picture.

[2] Please note that parts of this section have been adapted from Sallermann *et al.* [81].

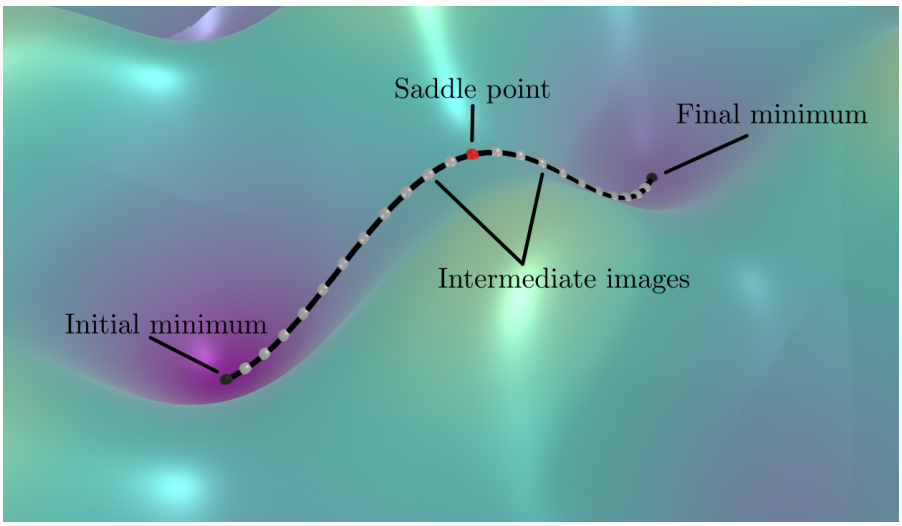


FIGURE 2.1
An illustration of a minimum energy path (MEP), which can be found with (geodesic) nudged elastic band method (G)NEB. The MEP (black line) connects two local minima (the initial and the final minium, shown as black spheres) of the two dimensional energy land scape (shown as a colored surface, the height represents energy and with low energies colored in blue and high energy regions colored in green to yellow) while minimizing the energy orthogonally to the path tangent. The intermediate images, employed by the (G)NEB method are visualized as gray spheres. The saddle point, which is the point of highest energy along the MEP is depicted as a red sphere.

energy orthogonally ot the path tangent. An illustration of such a path is shown in Fig. 2.1. The GNEB method arranges several replicas of the spin system, called images, in a chain, thereby providing a discretized interpolation between the initial and final configuration. To achieve convergence to an MEP, effective forces, acting on the entirety of the chain of images, are introduced, and the chain is iteratively optimized ("nudged") until convergence.

For a chain of N_{images} images with N_{spin} spins per image, the total effective force acting on image ν of the chain is a vector with $3N_{\text{spin}}$ components and given by

$$\boldsymbol{f}_\nu = \boldsymbol{s}_\nu + \boldsymbol{g}_\nu^\perp \quad \text{with} \quad \nu \in 2, ..., N_{\text{images}} - 1, \tag{2.1}$$

where $\boldsymbol{s}_\nu$ is called the spring force and $\boldsymbol{g}_\nu^\perp$ is the gradient force, $\boldsymbol{g} = -\boldsymbol{\nabla}\mathcal{H}$, projected orthogonally to the path tangent $\hat{\boldsymbol{t}}_\nu$. Notice that the endpoints of the chain ($\nu = 1$ and $\nu = N_{\text{images}}$) are excluded in (2.1) and remain fixed. The spring force $\boldsymbol{s}_\nu$ ensures that, during the iterative optimization, the discrete images remain distributed equidistantly along the chain and is defined as

$$\boldsymbol{s}_\nu = \Delta_{\nu,\nu+1}\hat{\boldsymbol{t}}_\nu, \tag{2.2}$$

where $\Delta_{\nu,\nu+1}$ is a measure of distance between image ν and image $\nu+1$ and $\hat{\boldsymbol{t}}_\nu$ is the tangent to the path at image ν. The distance between two adjacent images ν and $\nu+1$ is computed from the angles between spins,

$$\Delta_{\nu,\nu+1} = \sqrt{\sum\nolimits_i \angle\left(\hat{s}_i^{(\nu+1)}, \hat{s}_i^{(\nu)}\right)^2}, \tag{2.3}$$

where $\hat{s}_i^{(\nu)}$ is the i-th spin of image ν. The tangent $\hat{\boldsymbol{t}}_\nu$ is found from the central finite difference between image $\nu+1$ and image $\nu-1$, which is then orthogonally projected to image ν,

$$\hat{\boldsymbol{t}}_\nu = \begin{pmatrix} \left[\vec{d}_1^{(\nu-1,\nu+1)} - \left(\vec{d}_1^{(\nu-1,\nu+1)} \cdot \hat{s}_1^{(\nu)}\right)\hat{s}_1^{(\nu)}\right]_\alpha \\ \vdots \\ \left[\vec{d}_N^{(\nu-1,\nu+1)} - \left(\vec{d}_N^{(\nu-1,\nu+1)} \cdot \hat{s}_N^{(\nu)}\right)\hat{s}_N^{(\nu)}\right]_\alpha \end{pmatrix}, \tag{2.4}$$

where

$$\vec{d}_i^{(\nu-1,\nu+1)} = \hat{s}_i^{(\nu+1)} - \hat{s}_i^{(\nu-1)},$$

and $\alpha \in \{x, y, z\}$.
Note that the tangent found in Eq. (2.4) is additionally normalized as a $3N$ vector.

Further note, that Eq. (2.4) is not the only possible choice of tangent definition and more sophisticated choices can be made by taking the energy of individual images into account. In practice, a definition according to Ref. [147] may reduce undesirable features, like kinks, in the optimized path.

The gradient force acting on a spin $\hat{s}_i^{(\nu)}$ is found by taking the negative of the partial derivative of the energy, given by the Heisenberg Hamiltonian Eq. (1.16), with regards to the spin direction. The gradient force vector $\boldsymbol{g}_\nu$ is the composition of these single spin forces

$$\boldsymbol{g}_\nu = \begin{pmatrix} -\left[\boldsymbol{\nabla}_{\hat{s}_1^{(\nu)}} \mathcal{H}\right]_\alpha \\ \vdots \\ -\left[\boldsymbol{\nabla}_{\hat{s}_N^{(\nu)}} \mathcal{H}\right]_\alpha \end{pmatrix}. \tag{2.5}$$

We can form the projected gradient force $\boldsymbol{g}_\nu^\perp$ by removing the component parallel to the path tangent

$$\boldsymbol{g}_\nu^\perp = \boldsymbol{g}_\nu - (\boldsymbol{g}_\nu \cdot \hat{\boldsymbol{t}}_\nu)\hat{\boldsymbol{t}}_\nu. \tag{2.6}$$

The climbing image variant of the GNEB method (CI-GNEB) can be used to place one of the images exactly at the maximum of the MEP and therefore at a saddle point [148]. In the CI-GNEB method the spring force $\boldsymbol{s}_\nu$, acting on a selected "climbing" image, is deactivated

and replaced by the inverted component of the gradient force along the tangent.

One disadvantage of the GNEB method is that both states, the initial and the final state, need to be known in advance. Another drawback is that typically the entire path has to be discretized, which makes the calculations expensive and possibly leads to a low resolution around the saddle point. One approach to deal with this reduced resolution around the saddle point is to introduce energy weighted spring forces [120, 148], which increase the density of images near energy peaks of the path.

2.2 Minimum Mode Following Method

The minimum mode following method is a general framework for single-ended saddle points searches, explicitly targeting the softest vibrational mode (the mode of lowest curvature) at each step [149, 150]. In a minimum-mode following algorithm, one iteratively identifies the direction of lowest curvature on the potential energy surface and then ascends along that direction while relaxing (descending) in all perpendicular directions. By doing so, the algorithm "follows" the minimum-curvature mode out of a potential well, eventually reaching a first-order saddle point. This strategy is sometimes called "eigenvector-following" in the literature, since it effectively follows an eigenvector of the Hessian (the matrix of second derivatives), albeit without explicitly computing the full Hessian at each step. Early eigenvector-following techniques required full Hessian calculations (e.g., the method of Cerjan and Miller for transition states [151]), but minimum-mode following generalizes this idea to large systems by using only iterative updates of the softest mode direction [152].

In practical terms, minimum-mode following algorithms reverse the force component along the current lowest-curvature mode. A representative equation of motion for such an algorithm is:

$$\dot{\boldsymbol{x}} = -\boldsymbol{\nabla} V(\boldsymbol{x}) + 2\big[\boldsymbol{\nabla} V(\boldsymbol{x}) \cdot \hat{\boldsymbol{\tau}}\big]\hat{\boldsymbol{\tau}}, \tag{2.7}$$

where $-\boldsymbol{\nabla} V(\boldsymbol{x})$ is the negative gradient (the usual steepest descent search direction for minimizing the energy) and $\hat{\boldsymbol{\tau}}$ is the unit vector along the minimum-curvature mode at the current point [153].

The application to magnetic systems is straight forward and has been demonstrated by Müller *et al.* [145], where $-\boldsymbol{\nabla} V(\boldsymbol{x})$ is replaced by $-\boldsymbol{\nabla}_{\perp}\mathcal{H}(s) \in T_s$, which is the projection of the gradient of the Hamiltonian energy into the tangent space of the spin manifold.

Equation (2.7) indicates that the force component along $\hat{\boldsymbol{\tau}}$ is inverted (the term in brackets is the projection of the gradient along $\hat{\boldsymbol{\tau}}$, which is then given a positive sign to push uphill), while components orthogonal to $\hat{\boldsymbol{\tau}}$ retain their usual downhill direction. In effect, the

optimizer climbs *gently uphill* along the softest mode and downhill along all other directions. This evolution drives the system toward a first order saddle point since the only direction in which the energy is not minimized is the $\hat{\boldsymbol{\tau}}$ direction.

Determining the minimum mode is a partial diagonalization problem, which may be solved in a number of ways – for example with the Lanczos method, Davidson method, Jacobi-Davidson method, the dimer method or other iterative Rayleigh-Ritz optimization techniques [153–157].

2.2.1 The NEB dimer method

The GNEB method can be connected to the MMF methods, more specifically to a variant of the dimer method as described by Sallermann *et al.* [81].[3] This can be accomplished by using only two images (the endpoints), turning the chain into a dimer while simultaneously allowing the endpoints to move. There are several advantages to this method, when comparing it to the GNEB method: On one hand, it allows for arbitrary resolution around the saddle point, and on the other hand the computational effort is greatly reduced since fewer images are needed.

In the NEB variant of the dimer method, the forces on the two images, 1 and 2, are given by

$$\boldsymbol{f}_{1/2} = \boldsymbol{s}'_{1/2} + \boldsymbol{g}^{\perp}_{1/2} + \boldsymbol{t}_{1/2}. \tag{2.8}$$

The different force contributions are discussed below. Compared to the regular GNEB method, the spring forces $\boldsymbol{s}'_{1/2}$ are modified and an equilibrium distance δ is introduced, which prevents the two images from collapsing into each other, leading to

$$\boldsymbol{s}'_{1/2} = \pm(\Delta_{1,2} - \delta)\hat{\boldsymbol{t}}_{1/2}. \tag{2.9}$$

To estimate the path tangents $\boldsymbol{t}_{1/2}$, a forward/backward difference is used, as opposed to the central finite differences from the GNEB method. The definitions of the projected gradient forces $\boldsymbol{g}^{\perp}_{1/2}$ are identical to the regular GNEB method [see Eq. (2.6)]. Lastly, we define the translational forces $\boldsymbol{t}_{1/2}$ which move the dimer towards an energy maximum along the tangent, without changing the relative distance of the endpoints. They are constructed by inverting the average of the gradient forces of both endpoints and projecting it along the tangent. Before taking the average, the forces are rotated

[3] Please note that parts of this section have been adapted from Sallermann *et al.* [81].

into the tangent frame of the respective spin configurations giving

$$\boldsymbol{t}_{1/2} = \left[-\frac{1}{2}\left(\boldsymbol{g}_{1/2} + \boldsymbol{R}_{2/1\to 1/2}\boldsymbol{g}_{2/1}\right)\cdot\boldsymbol{t}_{1/2}\right]\boldsymbol{t}_{1/2}, \tag{2.10}$$

where $\boldsymbol{R}_{1/2\to 2/1}$ denotes the transformation from the tangent frame of one endpoint configuration into the other. The transformation $\boldsymbol{R}_{1\to 2}\boldsymbol{g}_1$ is found by applying the 3×3 rotation matrices $\boldsymbol{R}_i^{(1,2)}$, which rotate the i-th spin of the first image $\hat{s}_i^{(1)}$ into the i-th spin of the second image $\hat{s}_i^{(2)}$, to the component vectors of the gradient force resulting in

$$\boldsymbol{R}_{1\to 2}\boldsymbol{g}_1 := \begin{pmatrix} -\left[\boldsymbol{R}_1^{(1,2)}\,\boldsymbol{\nabla}_{\hat{s}_1^{(1)}}\,\mathcal{H}\right]_\alpha \\ \vdots \\ -\left[\boldsymbol{R}_N^{(1,2)}\,\boldsymbol{\nabla}_{\hat{s}_N^{(1)}}\,\mathcal{H}\right]_\alpha \end{pmatrix}. \tag{2.11}$$

The per-spin 3×3 rotation matrices $\boldsymbol{R}_i^{(1,2)}$ can be defined by using axes $\hat{s}_i^{(1)}\times\hat{s}_i^{(2)}$ and angles $\angle\left(\hat{s}_i^{(1)},\hat{s}_i^{(2)}\right)$ together with Rodrigues' formula [158]. For the inverse transformation $\boldsymbol{R}_{2\to 1}\boldsymbol{g}_2$ these per-spin rotation matrices are simply transposed.

2.2.2 Components of the dimer movement

It can be useful to split the forces on the dimer given by Eq. (2.8) into four components

1. Rotation into the minimal mode
2. Relaxation orthogonally to the dimer tangent
3. Parallel uphill climbing along the dimer tangent
4. Spring forces preserving a constant distance between the images

When the force contributions in Eq. (2.8) are split in this way, it allows us to define individual coefficients to control the strength of each contribution. This can be useful to fine tune strategies to escape convex regions, e.g. around local energy minima. The parallel uphill climbing and the spring force contribution are already evident from Eq. (2.8).

To obtain the rotation and orthogonal relaxation, as separate contributions, we define a symmetrized gradient force

$$\boldsymbol{g}_{1/2}^S = \frac{1}{2}\left(\boldsymbol{g}_1 + \boldsymbol{g}_2\right) \tag{2.12}$$

and an anti-symmetrized gradient force

$$\boldsymbol{g}_{1/2}^A = \frac{1}{2}\left(\boldsymbol{g}_1 - \boldsymbol{g}_2\right). \tag{2.13}$$

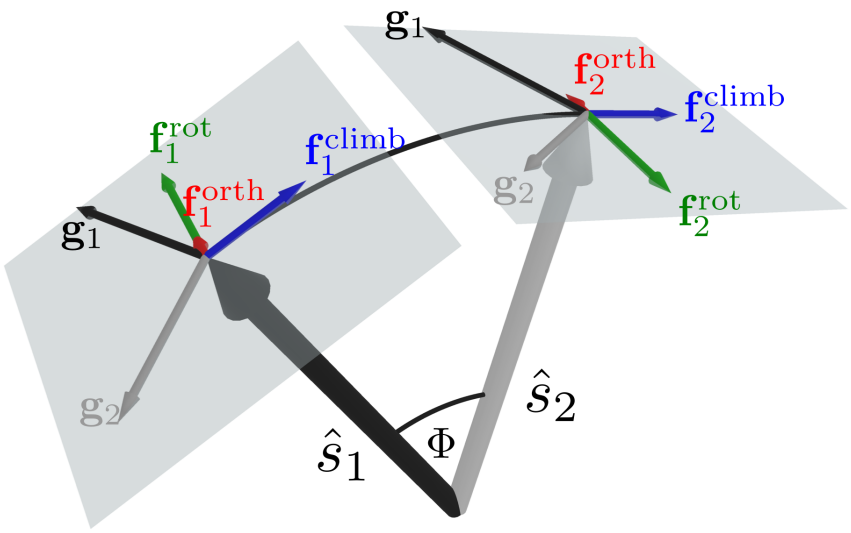


FIGURE 2.2

The components of the forces on a dimer. Two spins $\hat{s}_1$ and $\hat{s}_2$ are shown (big black and gray arrow, respectively). For each spin, the tangent plane is indicated. The components of the dimer force are shown individually for the two tangent planes. They are: (i) the uphill climbing force in blue, (ii) the orthogonal relaxation force in red and (iii) the rotational force in green. All of these forces, in the respective tangent frames, can be constructed by parallel transport of the gradient forces from one tangent frame to another. In this case, the gradient force $\boldsymbol{g}_1$ acting on $\hat{s}_1$, needs to be transported from the tangent frame of $\hat{s}_1$ to the tangent frame of $\hat{s}_2$ by applying a rotation around an axis $\hat{s}_1 \times \hat{s}_2$ by the angle Φ (which is the angle between the two spins, also indicated in the illustration). Then the forces in the tangent frame of $\hat{s}_2$ can be constructed using the parallel transported $\boldsymbol{g}_1$. To construct the forces in the tangent frame of $\hat{s}_1$, the inverse operation has to be applied to the gradient force $\boldsymbol{g}_2$ acting on $\hat{s}_2$. The gradient forces in the respective tangent frames are indicated by smaller black and gray arrows respectively.

Note that, like depicted in Fig. 2.2, the symmetrized and anti-symmetrized gradient need to be defined separately for each of the two tangent frames.

Of course, the gradient force can be easily reconstructed by re-combining the anti-symmetric and symmetric contributions

$$\boldsymbol{g}_{1/2} = \boldsymbol{g}^S_{1/2} \pm \boldsymbol{g}^A_{1/2}. \tag{2.14}$$

Further, it is obvious that the translational force $\boldsymbol{t}_{1/2}$ is merely the symmetrized gradient projected along the tangent

$$\boldsymbol{t}_{1/2} = -\left(\boldsymbol{g}^S_{1/2} \cdot \boldsymbol{t}_{1/2}\right) \boldsymbol{t}_{1/2}. \tag{2.15}$$

Overall, the effective force on the dimer endpoints, Eq. (2.8), can be represented as

$$\begin{aligned} \boldsymbol{f}_{1/2} = \; & \boldsymbol{g}^S_{1/2} - \left(\boldsymbol{g}^S_{1/2} \cdot \boldsymbol{t}_{1/2}\right) \boldsymbol{t}_{1/2} \\ & \pm \left[\boldsymbol{g}^A_{1/2} - \left(\boldsymbol{g}^A_{1/2} \cdot \boldsymbol{t}_{1/2}\right) \boldsymbol{t}_{1/2}\right] \\ & - \left(\boldsymbol{g}^S_{1/2} \cdot \boldsymbol{t}_{1/2}\right) \cdot \boldsymbol{t}_{1/2} \\ & + \boldsymbol{s}_{1/2} \\ = \; & \boldsymbol{f}^{\text{orth}}_{1/2} + \boldsymbol{f}^{\text{rot}}_{1/2} + \boldsymbol{f}^{\text{climb}}_{1/2} + \boldsymbol{s}_{1/2} \end{aligned}, \tag{2.16}$$

where the first contribution causes the dimer to relax orthogonally, the second contribution causes it to rotate its tangent into the direction of the minimum mode, the third contribution causes it to climb up the energy surface in the direction of the tangent and the last contribution is the spring force, keeping the endpoints at the equilibrium distance. In Fig. 2.2, the different components of the dimer force are visualized on the example of a system with two spins.

The curvature of the energy surface in the direction of the dimer tangent $\hat{\boldsymbol{t}}$, and therefore the current approximation for the lowest Hessian eigenvalue, is given by the Rayleigh quotient (RQ)

$$R = \frac{\hat{\boldsymbol{t}}^T \boldsymbol{H} \hat{\boldsymbol{t}}}{\hat{\boldsymbol{t}}^T \hat{\boldsymbol{t}}}, \tag{2.17}$$

where $\boldsymbol{H}$ is the Hessian matrix. The Rayleigh quotient can be estimated from the anti-symmetrized gradients by expressing the action of the Hessian as a finite difference of gradients

$$\boldsymbol{H}(\boldsymbol{x})\hat{\boldsymbol{t}} \approx \boldsymbol{g}(\boldsymbol{x} + \hat{\boldsymbol{t}}) - \boldsymbol{g}(\boldsymbol{x}), \tag{2.18}$$

leading to

$$R \approx \frac{2\hat{\boldsymbol{t}}^T \boldsymbol{g}^A}{\Delta}, \tag{2.19}$$

where Δ is the difference in reaction coordinates as defined in Eq. (2.3). It does not matter at which endpoint of the dimer Eq. (2.19) is evaluated.

2.2.3 Backtracking line search for the dimer method

Line searches in numerical optimization are iterative methods that find optimal step sizes. They ensure convergence and stability and are often used in gradient descent or quasi-Newton methods, to minimize objective functions.

Consider an update step,

$$\boldsymbol{x} \to \boldsymbol{x}(\omega) = \boldsymbol{x} + \omega\boldsymbol{\Delta}, \tag{2.20}$$

where $\boldsymbol{x}$ is the current iterate and a suitable search direction $\boldsymbol{\Delta}$ has been determined (often from the gradient of the objective function), such that the only unknown is the step size ω.

Choosing an optimal step length is key for global convergence. The goal is to choose a step size ω that is neither too small (otherwise the optimization will be slow) or too big (otherwise the optimization will be unstable). A popular way to choose the step size is the class of algorithms known as line searches.

One problem, we are faced with when trying to apply line searches to saddle point searches, is that we *lack an objective function* and thus the step direction $\boldsymbol{\Delta}$ is not directly connected to a monotonically increasing/decreasing quantity. This is problematic since many of the widely used line searches rely on imposing certain conditions on the objective function values at candidate step sizes (one example are the Wolfe conditions [159, 160]).

Technically, one could use the square of the gradient $|\boldsymbol{\nabla}\mathcal{H}(\boldsymbol{x})|^2$ as an objective function as is done in gradient squared descent methods [161], however this objective function is minimized by local minima, saddle points and *inflection points* – leading to "false positives". It might nonetheless be worth further exploration.

Here, we review a line search method which may be applied to saddle point searches with the dimer method. It is called the backtracking line search [122] and is based on the idea of iteratively reducing the step size, starting from an initially optimistically large value. This technique is especially suited for quasi-Newton methods since a natural choice for the initial step size is simply $\omega = 1$.

The line search works as follows: For each trial step size ω, compute the gradients $\boldsymbol{g}(0)$ and $\boldsymbol{g}(\omega)$ and the energies $E(0)$ and $E(\omega)$.[4] We may then construct a parabolic approximation of the energy surface

[4] Note that the energy is *not* an objective function in the saddle point search, but, nonetheless, the search direction is derived from its gradient. Therefore, it makes sense to restrict the step size to regions, where the local assumptions about the energy landscape hold approximately true.

in the search direction as

$$E^{\text{aprx}}(\omega) - E(0) = a\omega + b\omega^2, \tag{2.21}$$

with

$$a = \boldsymbol{g}(0)^T \boldsymbol{\Delta} \tag{2.22}$$

$$b = \frac{1}{2}\left[\boldsymbol{g}(\omega)^T \boldsymbol{\Delta} - a\right]. \tag{2.23}$$

For each trial value of ω, the line search checks the following condition:

$$\left|\frac{E^{\text{aprx}}(\omega) - E(\omega)}{E(\omega) - E(0)}\right| := \frac{\Delta E_\omega(\omega)}{\Delta E_0(\omega)} := R(\omega) < \tau \tag{2.24}$$

If Eq. (2.24) is fulfilled, the trial step size ω is accepted and the iterate $\boldsymbol{x}$ is updated according to (2.20), if it is not fulfilled a new trial step size ω' is constructed by multiplying ω by a shrinking factor α such that $\omega' = \alpha\omega$ is constructed and the condition is checked again. A common choice is $\alpha = \frac{1}{2}$.

Intuitively, Eq. (2.24) measures how much the actual energy $E(\omega)$ at a candidate step size ω agrees with the value expected from a parabolic prediction based on the current value of the iterate. Thus, the step size is reduced when the energy landscape is an-harmonic.

For $\omega \to 0$, the numerical error on $R(\omega)$ will get larger than the tolerance τ. This defines a region of applicability for this line search. The numerical error depends on the floating point precision ε, which is the difference between 1.0 and the next nearest number that can be represented by the floating point format.

We can model this numerical error for an arbitrary floating point number A as

$$A = A_0(1 + \xi),$$

where A_0 is the "true" value of A, and $\xi \sim \mathcal{N}(0, \varepsilon^2)$ is a Gaussian noise term with zero mean and standard deviation ε.

Using error propagation formulas, we can now estimate the error on $\Delta E_0(\omega)$

$$\sigma_{\Delta E(\omega)} = \sqrt{\sigma^2_{E(\omega)} + \sigma^2_{E(0)}} \tag{2.25}$$

$$= \sqrt{\sigma^2_{E(\omega)} + \sigma^2_{E(0)}} \tag{2.26}$$

$$\approx \sqrt{2}\sigma_{E_0} \tag{2.27}$$

$$= \sqrt{2}E_0\varepsilon \tag{2.28}$$

Therefore, it is sensible to introduce an applicability criterion depending on the current energy and the floating point representation

$$\tau > \kappa E_0 \varepsilon,$$

where κ is an arbitrary constant. If this criterion is fulfilled, we can apply the line search. If it is not fulfilled, we are likely very close to a stationary point of our optimization. In these cases quasi-Newton steps with $\omega = 1$ tend to be well behaved.

Since the numerical error is almost certainly larger than the bare floating point error ε and the analysis of the error, above, is more illustrative than quantitative, it is advisable to choose a generously large value for κ (say $\kappa > 10^3$).

To apply this line search to several images at once, one energy parabola has to be constructed *per image* and the step size should be taken as the minimum step size over all images

$$\omega = \min_{1 \leq i \leq N_{\text{images}}} \omega_i. \tag{2.29}$$

2.3 Finding extremal eigenpairs via direct optimization

Reading the previous section[5] should have made it clear that efficiently obtaining the lowest Hessian eigenvalues (and their eigenvectors) is crucial in the MMF method.

Besides finding only the lowest eigenvector/value it can be hugely beneficial to also compute the *second lowest* eigenpair, because it not only identifies the true "minimum mode" for stable uphill convergence but also provides the second mode needed to detect and smoothly navigate any near-degenerate mode crossings, ensuring robust, first-order saddle point convergence.

As mentioned before, there are plenty of methods, which can perform a partial diagonalization efficiently [155–157]. Crucially, these methods do not need knowledge of the full Hessian matrix, but only need to know how to apply the Hessian to a vector, meaning they need to be able to perform the operation

$$\boldsymbol{y} = \boldsymbol{H}\boldsymbol{x}. \tag{2.30}$$

This is extremely important since explicitly constructing the full $2N_{\text{spin}} \times 2N_{\text{spin}}$ Hessian matrix requires $\mathcal{O}(N_{\text{spin}}^2)$ memory and up to $\mathcal{O}(N_{\text{spin}}^2)$ - $\mathcal{O}(N_{\text{spin}}^3)$ computational effort, which becomes prohibitive for systems with $N_{\text{spin}} \gtrsim 10^5$ spins.

The Hessian-vector product can be evaluated without ever forming the full matrix by taking a finite-difference of the energy gradient. In

[5] Please note that the present section discusses results which are detailed more closely in Schrautzer *et al.* [154].

its simplest form one writes

$$\boldsymbol{H}\boldsymbol{x} \;\approx\; \frac{\boldsymbol{\nabla}\mathcal{H}(\boldsymbol{s}+\epsilon\,\boldsymbol{x}) \;-\; \boldsymbol{\nabla}\mathcal{H}(\boldsymbol{s})}{\epsilon}, \tag{2.31}$$

where $\epsilon \ll 1$ and $\boldsymbol{x}$ is the trial direction. For a spin system one replaces the shift $\boldsymbol{s} \to \boldsymbol{s} + \epsilon\boldsymbol{x}$ by the corresponding retraction (rotation of each moment), computes the new gradient, parallel-transports it back to the original tangent space, and then forms the difference. This yields an $\mathcal{O}(N_{\text{spin}})$ evaluation of $\boldsymbol{H}\boldsymbol{x}$ without ever constructing the $2N_{\text{spin}} \times 2N_{\text{spin}}$ Hessian. Please refer to Fig. 2.3 for an illustration of this process.

Especially, when magnetostatics are important and need to be explicitly simulated (meaning the Hessian matrix is not sparse) this is a feasible option as evidenced by Fig. 2.4, which shows how the wall time of evaluating the gradient of the RQM (which includes the action of the Hessian) scales with system size. The same benefits can, of course, be harvested for most (flexible enough) implementations of a partial diagonalization.

A flowchart presenting the most important steps in the MMF algorithm, together with the direct optimization of the (generalized) RQ is presented in Fig. 2.5. For details refer to the preprint by Schrautzer, Sallermann, Bessarab & Jónsson [154].

Lastly, Fig. 2.6 demonstrates the effectiveness of the method by applying the MMF algorithm to a three-dimensional system *with magnetostatics interactions* – computed via the convolution theorem and fast fourier transforms. Thus, a network of saddle points between metastable states is uncovered and the MEPs between the metastable states are found thereafter.

2.4 Alternative Saddle Point Search Methods

In addition to the GNEB method and the dimer approach discussed above, several other techniques have been developed for locating saddle points on potential energy surfaces. None of them are directly applied in this work, instead, they are briefly acknowledged in the following sections.

These methods provide complementary strategies for finding transition states and reaction pathways, especially in cases where the nudged elastic band or standard dimer method may be inefficient or inapplicable. Here we highlight three such approaches – the *minimum mode following* method, *gradient extremal* paths, and *gentlest ascent dynamics* – emphasizing their application to saddle point searches and their relation to the previously discussed methods.

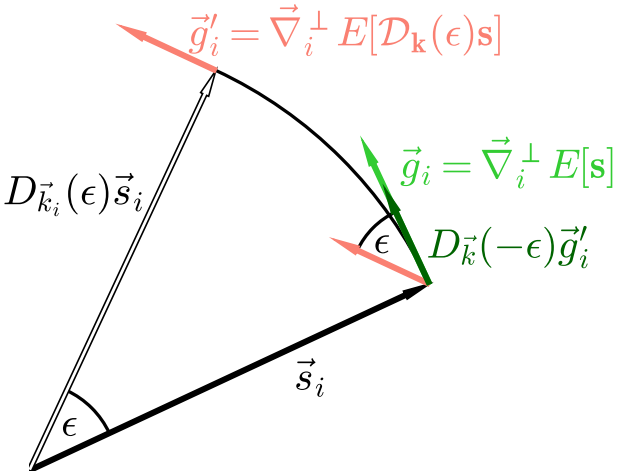


FIGURE 2.3
Illustration of the quantities involved in calculating the action of the Hessian by forward finite difference approximation with a displacement parameter ϵ for a single magnetic moment $\boldsymbol{s}_i$. To calculate the finite difference of the gradient $\boldsymbol{g}_i$ along a given direction, the magnetic moment is first displaced (rotated) along this direction and the gradient $\boldsymbol{g}_i^{'}$ is calculated for the rotated magnetic moment $D_{\boldsymbol{k}_i}(\epsilon)\boldsymbol{s}_i$. Parallel transport ($\mathcal{D}_{\hat{k}_i}(-\epsilon)\boldsymbol{g}_i^{'}$) is then applied towards the tangent space of the initial magnetic moment $\boldsymbol{s}_i$ to ensure that both gradients are defined within the same tangent space for the calculation of the finite difference. Figure taken from the preprint by Schrautzer, Sallermann, Bessarab & Jónsson [154].

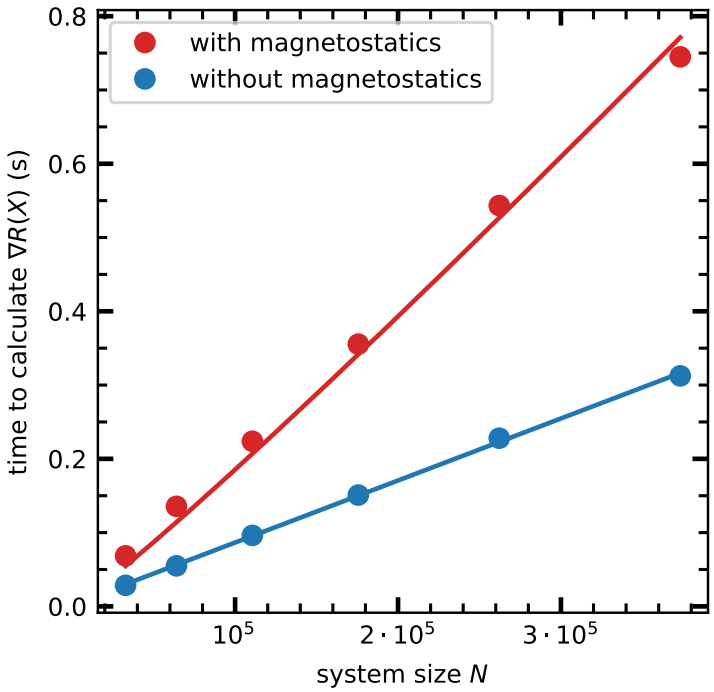


FIGURE 2.4
Mean wall time required for a single evaluation of the Rayleigh quotient gradient $\nabla R(X)$ as a function of the number of magnetic moments N in a cubic system with and without magnetostatic interactions, as indicated in the legend. The blue (red) line shows the linear ($N \log N$) fit. Figure taken from the preprint by Schrautzer, Sallermann, Bessarab & Jónsson [154].

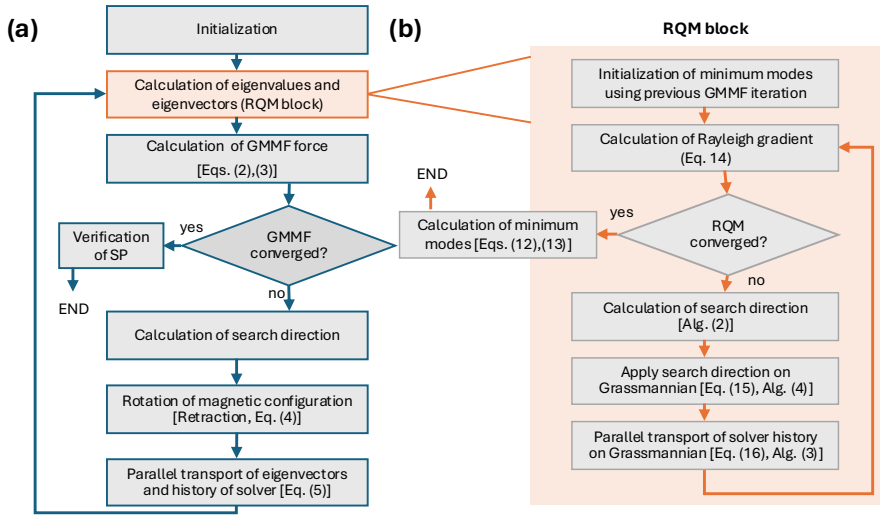


FIGURE 2.5
Flowchart for the algorithm of the GMMF method (a) and for the RQM eigensolver method (b) as presented in the preprint by Schrautzer, Sallermann, Bessarab & Jónsson [154]. In each GMMF iteration, the RQM block is executed to calculate the eigenvalues and eigenvectors of the Hessian for the current magnetic configuration. Figure taken from the preprint by Schrautzer, Sallermann, Bessarab & Jónsson [154].

2.4.1 Gradient Extremals

Gradient extremals are another tool used to investigate reaction pathways and the topography of potential energy surfaces. A *gradient extremal* (GE) is defined as a continuous path on the surface along which the gradient vector is everywhere aligned with a principal axis of curvature of the potential. More formally, if $\boldsymbol{H}(\boldsymbol{x})$ is the Hessian matrix at point $\boldsymbol{x}$, then along a gradient extremal the condition

$$\boldsymbol{H}(\boldsymbol{x})\,\boldsymbol{\nabla}V(\boldsymbol{x}) = \lambda(\boldsymbol{x})\,\boldsymbol{\nabla}V(\boldsymbol{x}) \tag{2.32}$$

holds for some scalar $\lambda(\boldsymbol{x})$ that varies along the path. In other words, the force $-\boldsymbol{\nabla}V$ at each point is collinear with one of $\boldsymbol{H}$'s eigenvectors. This definition implies that the direction of steepest descent (the gradient) is an extremal direction with respect to the surface's curvature. Intuitively, a gradient extremal tends to follow either a valley floor or a ridge line on the potential energy surface: if the gradient's norm is minimized in the directions perpendicular to the path, the GE will trace the bottom of a valley, whereas if it is maximized, the GE runs along a ridge [162].

In the context of reaction pathways, gradient extremals can serve as representations of possible reaction routes, especially in situations where the minimum-energy path (MEP) might be ambiguous or bifurcate. For a simple, well-behaved reaction, the MEP (often obtained via

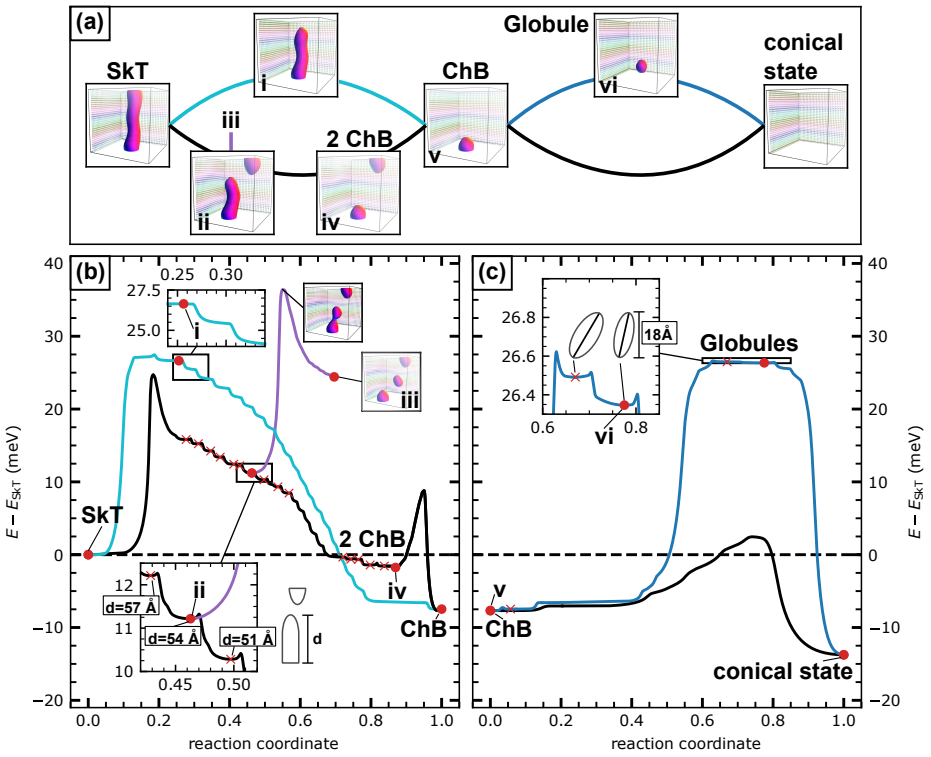


FIGURE 2.6

(a): Graph showing metastable configurations (insets) and possible transitions between them in the 3D system with magnetostatic interactions, as obtained with the GMMF method. The magnetic configurations are visualized by the isosurfaces of $s_z = 0$. (b): Energy variation along calculated MEPs connecting the Skyrmion tube (SkT) state with the chiral bobber (ChB) state and the metastable state involving a globule between two chiral bobbers. The insets show zoomed-in views of the plots, magnetic configurations at specific points along the MEPs, and a sketch of the two-bobber state. (c): Energy variation along calculated MEPs connecting the chiral bobber (ChB) state and the conical state. The insets show a zoomed-in view of the plot and sketches of the globule states. The red crosses mark position of the energy minima. The energy minima corresponding to metastable configurations shown in (a) are indicated with red dots. The reaction coordinate is defined as a normalized displacement along the MEP. Different normalization factors are used for each transition to align energy minima corresponding to the same magnetic configurations. The dashed line shows the zero energy level corresponding to the relaxed Skyrmion tube configuration. Figure taken from the preprint by Schrautzer, Sallermann, Bessarab & Jónsson [154].

the intrinsic reaction coordinate from a saddle point) lies in the valley floor and a gradient extremal coinciding with that valley will closely match the MEP. However, if a valley on the potential energy surface splits into two sub-valleys (a phenomenon known as a valley–floor bifurcation), the steepest descent path from the saddle point will branch into two directions, each leading to different minima. In such cases, a single "reaction coordinate" is no longer unique. Gradient extremal analysis is useful here: one can follow a GE starting from a reactant minimum in the direction of rising energy, and the GE may naturally veer toward one or the other valley floor as the valley splits. In practice, locating a saddle point via gradient extremals might involve following the GE until the gradient $|\boldsymbol{\nabla} V|$ reaches a turning point or becomes very small, indicating proximity to a stationary point (saddle or local maximum/minimum). Thus, while gradient extremals are not a direct algorithm for saddle search in the same sense as the dimer or NEB methods, they identify "valley floor" routes and possible ridges, guiding where one might initiate a focused saddle search. In summary, gradient extremals complement MEP-based methods by revealing alternative pathways and helping to predict the existence or location of saddle points when the reaction pathway is complex or branching. This makes them a useful theoretical construct for reaction path analysis, which can inform practical saddle point searches (for example, by suggesting initial guesses for NEB or minimum-mode following calculations in cases of multiple possible products).

2.4.2 Gentlest Ascent Dynamics

Gentlest ascent dynamics (GAD) is a modern algorithmic approach for directly finding saddle points by simulating a modified dynamical system. In contrast to the static path-following nature of gradient extremals, GAD formulates the search for a saddle as a continuous dynamics that a point on the potential energy surface will follow. The key idea, introduced by Weinan E and coworkers [163], is to couple the system's coordinates to an auxiliary direction vector (similar to $\hat{\boldsymbol{\tau}}$ in the minimum-mode method) and to design equations of motion such that the system climbs out of a potential well along the gentlest (lowest-curvature) ascent direction. In essence, GAD implements the minimum-mode following principle (Eq. 2.7) in a time-dependent fashion. One part of the GAD equation of motion ensures that the search direction vector $\boldsymbol{\tau}(t)$ continuously aligns with the current lowest-eigenvalue mode of the Hessian (using an iterative procedure analogous to a power method for finding eigenvectors), while another part updates the position $\boldsymbol{x}(t)$ by moving uphill along that direction and downhill along all others. By construction, any stable fixed point of this dynamical system is an index-1 saddle point

of the original potential, meaning that if one integrates the GAD equations starting from a point near a minimum, the trajectory will eventually converge to a nearby saddle point (the "escape" saddle out of that basin).

One can appreciate the difference between GAD and gradient extremal pathways as follows: GAD is an *algorithmic* tool to pinpoint a saddle (it will drive a single configuration to the saddle), whereas gradient extremals define a *geometric path* on the surface (potentially connecting a minimum and a saddle, but requiring integration of a condition rather than converging to a point). In practice, GAD shares similarities with the dimer/min-mode methods – for example, it does not require knowledge of the product state and it avoids full Hessian calculations by iteratively updating the ascent direction. However, instead of taking discrete optimization steps, GAD treats the search as a continuous dynamics, which can be advantageous for coupling with molecular dynamics or when a smooth escape trajectory is desired. Another distinction is that gradient extremals demand the gradient to align with a curvature eigenvector at every point along a path, which usually necessitates calculating second derivatives during path following. GAD, on the other hand, only enforces the alignment in a local, dynamical sense and often uses a simpler update (like a constrained force iteration) to adjust the direction vector, making it more tractable for high-dimensional systems.

In terms of application, gentlest ascent dynamics is used to locate transition states much like the dimer method: one typically starts GAD from a local minimum (or a configuration in its vicinity) and lets the dynamics evolve. The trajectory will initially behave like ordinary gradient descent in most directions but will slowly drift uphill along one special direction – the direction that requires the least uphill force (hence "gentlest" ascent). Over time, the configuration climbs out of the attraction basin of the minimum and approaches the saddle point; once near the saddle, the net force approaches zero, signaling that the saddle point has been found. GAD has been demonstrated on model systems and in some cases combined with other techniques (e.g. combining GAD with the dimer method or with molecular dynamics) to enhance exploration of complex energy landscapes. For the purposes of this chapter, GAD can be seen as a complementary single-ended saddle search method: like the dimer-based minimum-mode following approach, it requires only an initial state and finds a transition state by exploiting the lowest-curvature mode. Its continuous dynamics formulation provides an alternative way to achieve the same goal, and the method can be particularly useful in verifying that a found saddle is indeed the only attractor from a given basin or in exploring the mechanism of escape from a metastable state.

2.4.3 Cosine square ridge following

Another method (on which the author has worked) is dubbed the $\cos^2$ ridge following method. This method attempts to find saddle points by tracing out paths defined as ridges of the following function

$$C^2(\boldsymbol{x}) = \left(\frac{\boldsymbol{\nabla} V(\boldsymbol{x})}{|\boldsymbol{\nabla} V(\boldsymbol{x})|} \cdot \hat{\boldsymbol{\tau}} \right)^2, \tag{2.33}$$

where $\hat{\boldsymbol{\tau}}$ is the direction of the minimum mode and $\boldsymbol{\nabla} V(\boldsymbol{x})$ is, again, the gradient of the potential function with respect to the coordinates of the current point $\boldsymbol{x}$. The name of the method comes from the fact that the function C^2 can alternative be written as

$$C^2(\boldsymbol{x}) = \cos^2(\theta), \tag{2.34}$$

where θ is the angle between the gradient direction and the minimum mode. Ridges are defined as paths through the configuration space, where the path tangent is the direction in which $C^2(\boldsymbol{x})$ increases the most (or decreases the least).

The algorithm roughly adheres to the following ridge-tracking strategy:

Given a current positions $\boldsymbol{x}$ as well as an initial guess for the direction of the ridge tangent $\boldsymbol{d}_0$, the constrained optimization problem

$$\boldsymbol{d}^* = \arg \max_{\|\boldsymbol{d}\|=1} C^2 \left(\boldsymbol{x}_k + r\, \boldsymbol{d} \right), \tag{2.35}$$

where r is a predefined step size. This problem is solved by locally maximizing the C^2 function (using an initial guess of $\boldsymbol{d} = \boldsymbol{d}_0$) with a conjugate gradient solver (employing stereographic coordinates to maintain the $\|\boldsymbol{d}\| = 1$ constraint). Once a suitable direction has been identified the iterate $\boldsymbol{x}$ is updated to $\boldsymbol{x} + \boldsymbol{d}$ and the process is repeated.

However, there are some serious caveats to this method and presently it cannot be considered applicable to anything but toy systems. Fig. 2.7 shows a result from such a toy system. The brown path, which starts from the local minimum at $((x, y) \approx (0.6, -0.5))$, bifurcates first into the red path (which leaves the plot at the bottom) and then later into the pink path (near a point of degeneracy). Following the pink path to its end leads to a saddle point. However, along the way it also bifurcates into the green path which ends at yet another saddle point – but not without bifurcating into the blue path, which ultimately ends up in another local minimum. More paths are present in the figure. Summarily, it should quickly become obvious that many bifurcations need to be followed. Further, it can be seen that, near points of degeneracy, numerically tracing out the ridge is not always reliable (observe for example the pink path). In higher dimensions these problems are likely to be worse.

To avoid spurious maxima when the two lowest Hessian eigenvalues λ_0, λ_1 are nearly degenerate, one can subtract a smooth Gaussian penalty and work with

$$\tilde{C}^2(\boldsymbol{x}) = C^2(\boldsymbol{x}) - A \exp\Big[-\tfrac{1}{2}\left((\lambda_1 - \lambda_0)\,\sigma\right)^2\Big] \tag{2.36}$$

where A and σ and tune the strength and width of the penalty. This ensures that when the soft mode and next mode become nearly equal in curvature, the algorithm still favours genuine ridges of high alignment rather than artifacts of accidental degeneracy.

Further, ridges can split into multiple branches or simply end. To flag a potential bifurcation at step k, one tracks:

- the ridge "width" W_k, i.e. the directional derivative of $\tilde{C}^2$ in the direction orthogonal to the current step;
- the change in alignment $C^2(\boldsymbol{x}_k)$ relative to its previous values;
- the turning angle between successive tangent guesses.

If two distinct directions on the ring yield nearly equal maxima of $\tilde{C}^2$, or if W_k and the turning angle both exceed user-defined tolerances, the algorithm records the current position and the two competing directions as a bifurcation point. These points are stored in a list for subsequent branch tracing, allowing the method to follow multiple competing ridge paths emanating from a single saddle region.

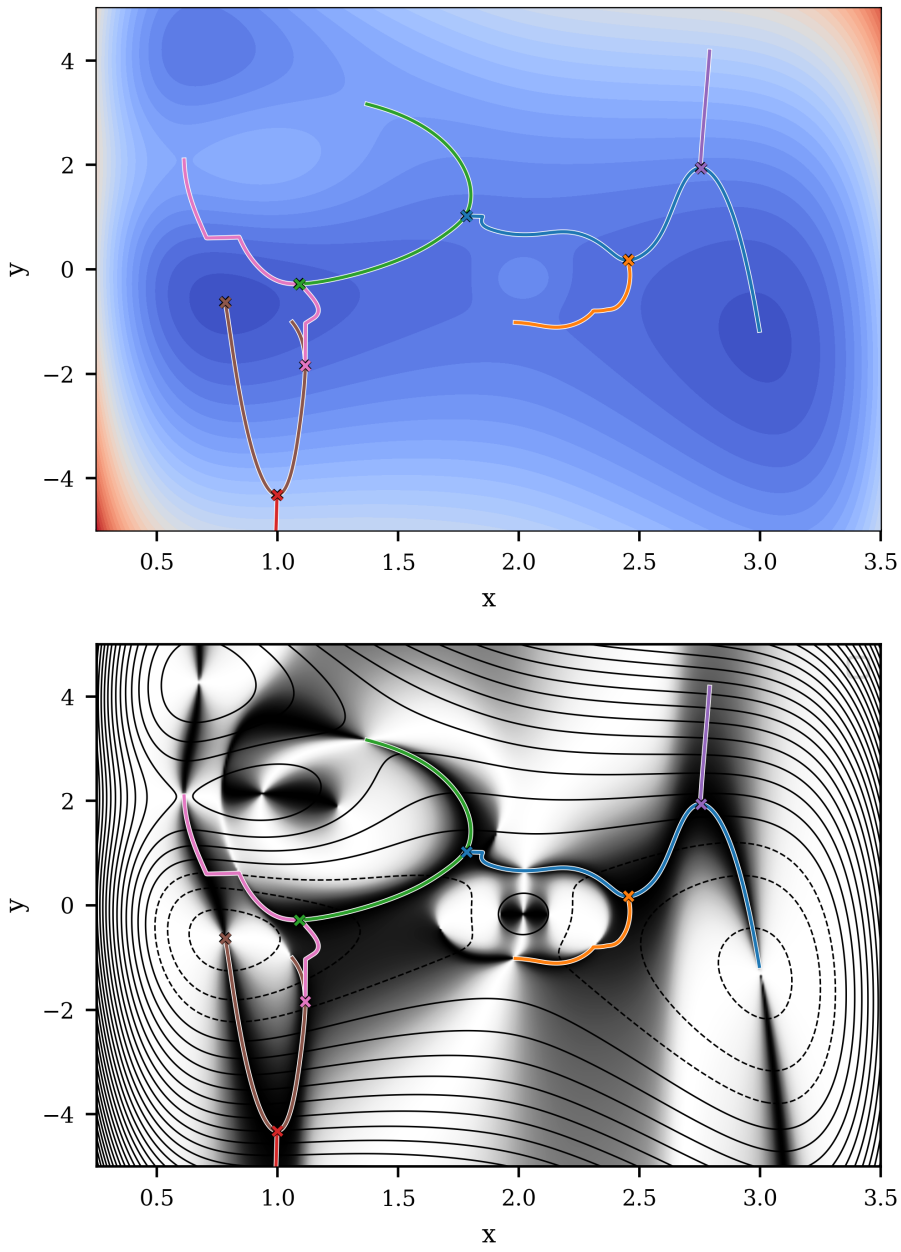


FIGURE 2.7
Cosine square ridge following paths from a preliminary algorithm on a two-dimensional toy surface. Each colored line represents one invocation of the ridge tracing with detected bifurcation points marked with a cross. The top plot overlays the paths on the energy surface (blue for low energy, red for high energy), while the bottom plot overlays them on a plot of the $C^2(\boldsymbol{x})$ function (white for $C^2(\boldsymbol{x}) = 0$, black for $C^2(\boldsymbol{x}) = 1$).

RATE THEORY 3

Obtaining the reaction rates of rare[1] processes via computer simulations is a difficult task and is commonly tackled via statistical means. In many systems, the underlying dynamics span a broad spectrum of timescales. The fast dynamics, which govern the fundamental physical interactions, occur on timescales that are orders of magnitude shorter than those associated with the slow, rare events of interest. For example, the Larmor precession of magnetic moments around an external magnetic field may occur with periodic times of a few tens of picoseconds. On the other hand, the decay of a Skyrmion may take up to several years. This inherent separation poses a significant challenge: directly simulating every fast-scale motion while waiting for a rare event to occur is computationally prohibitive. As a consequence, it is necessary to employ statistical approaches that allow one to bridge the gap between these disparate scales [164]. This potentially allows for capturing the essential physics without the need for exhaustive dynamical simulation over prohibitively long periods.

We will dive into the specifics of (harmonic) transition state [124, 125] theory in the context of atomistic spin dynamics. In doing so, the discussion will not only outline the general framework that has been traditionally employed to analyze rare events but also highlight the adaptations required when dealing with the intricacies of spin systems.

The presentation of the harmonic transition state theory, here, is different from other treatments in the atomistic spin simulation literature [109, 114, 127, 129, 165] in two ways: (i) The derivation is undertaken by connecting the problem at hand to the well-known properties of multivariate Gaussian probability distributions[2] and (ii)

[1] Rare means that we deal with a large separation of timescales: One slow timescale on which the process of interest takes place and a fast timescale on which the physics, driving the process, happen. In the context of a simulation this makes it difficult to obtain reaction rates via direct simulation, since the discrete timestep in any dynamics algorithm needs to be able to resolve the driving (fast) physics.

[2] This is natural since the canonical ensemble in a harmonic potential takes the form of a multivariate Gaussian.

the dynamical contribution to the transition rate in harmonic transition state theory is derived without neglecting thermal fluctuations in the linearized LLG equation. This approach allows us to retain some of the influence of the thermal fluctuations inherent in the system, which have been ignored in previous works.

Another consideration is the challenge of computing positive-definite sparse determinants of extremely large[3] sparse Hessian matrices in the presence of Goldstone modes, which are eigenvectors of the Hessian matrix with an eigenvalue of zero.

Further, this chapter contains some derivations of zero-mode volumes for non-translational Goldstone modes. Moreover, a criterion is derived that helps to decide if a soft mode may be approximated as a Goldstone mode.

3.1 Transition state theory

Due to the separation of timescales (usually a pitfall in brute force simulations) it is possible to obtain a meaningful estimate of the transition rate by honing in on a subregion of the configuration space, which at the same time should (i) separate the initial from the final configuration and (ii) be very unlikely to be occupied (due to a high energy cost). Such a region is called a transition state or dividing surface.

In transition state theory (TST), the rate is estimated by gauging the flux from the transition state towards the final state – this simplifies the bookkeeping since the transition state has one dimension less than the configuration space. A fundamental approximation of TST is the assumption that a trajectory, which leaves the transition state in the direction of the final configuration, never crosses it again. It is, however, possible to add so-called recrossing corrections by simulating dynamics near the transition state [166].

The transition rate, in transition state theory [125], Γ^{TST} is given by

$$\Gamma^{\mathrm{TST}} = \frac{1}{Z} \int v_{\perp}(\boldsymbol{n}) \theta\left(v_{\perp}(\boldsymbol{n})\right) \delta\left(f(\boldsymbol{n})\right) \exp\left(-\frac{E(\boldsymbol{n})}{k_B T}\right) \mathrm{d}\boldsymbol{n}, \tag{3.1}$$

where the transition state is defined by the hypersurface $f(\boldsymbol{n}) = 0$ and, further, we define the perpendicular velocity $v_{\perp}(\boldsymbol{n})$ as the velocity leading out of the transition state, thus pointing along the normal of the hypersurface and $\theta(x)$ as the Heaviside step function, which is used due to the assumption of no re-crossings. Moreover, Z is the

[3] A small three-dimensional system may, for example, contain 50^3 spins leading to a Hessian matrix with $4 \cdot (2 \cdot 50^3)^2$ entries.

canonical partition function of the system

$$Z = \int_{\boldsymbol{n}\in C\subset\mathcal{S}} \exp\left(-\frac{E\left(\boldsymbol{n}\right)}{k_B T}\right) \mathrm{d}\boldsymbol{n}, \tag{3.2}$$

where C is the subset of the spin manifold that is enclosed by the transition state. If we define the canonical partition function with respect to the transition state, as

$$Z^{\mathrm{TS}} = \int \delta(f(\boldsymbol{n})) \exp\left(\frac{-E(\boldsymbol{n})}{k_B T}\right) \mathrm{d}\boldsymbol{n}, \tag{3.3}$$

we can rewrite (3.1) as

$$\Gamma^{\mathrm{TST}} = \frac{Z^{\mathrm{TS}}}{Z} \langle v_\perp \theta(v_\perp)\rangle_{\mathrm{TS}}, \tag{3.4}$$

where $\langle ...\rangle_{\mathrm{TS}}$ denotes the expectation value, taken with respect to the transition state, i.e.

$$\langle A\rangle_{\mathrm{TS}} = \frac{1}{Z^{\mathrm{TS}}} \int \exp\left(-\frac{E(\boldsymbol{n})}{k_B T}\right) \delta(f(\boldsymbol{n})) A(\boldsymbol{n}) \mathrm{d}\boldsymbol{n}.$$

In the form of Eq. (3.4) the rate can, intuitively, be understood as consisting of an entropy factor $\frac{Z^{\mathrm{TS}}}{Z}$, which determines the "probability of the system to reach the transition surface", and a dynamical contribution $\langle v_\perp \theta(v_\perp)\rangle_{\mathrm{TS}}$, which determines the rate with which the system leaves the transition state into a direction which *does not lead back into the initial subspace* C.

3.2 Harmonic transition state theory

To move from the full transition state theory (TST) to the harmonic approximation (HTST), we start by approximating the integrals over the spin manifold by integrals in the tangent space of stationary points, meaning that, instead of integrating over points on the spin manifold $n \in \mathcal{S}$, we integrate over vectors $\boldsymbol{x} \in \mathcal{T}_{n_0}$ in the tangent space of n_0. In HTST we work with two distinguished, stationary points, the local minimum n_{min} and a first order saddle point n_{sp}.

The energy is approximated by a Taylor expansion up to second order in the vector of tangent space perturbations $\boldsymbol{x} \in \mathcal{T}_{\boldsymbol{n_0}}$

$$E(\boldsymbol{x}) \approx E_0 + \frac{1}{2}\boldsymbol{x}^T \boldsymbol{H} \boldsymbol{x}, \tag{3.5}$$

where $\boldsymbol{H}$ is the $2N \times 2N$ Hessian matrix.

Transforming into the eigenbasis of the Hessian $\boldsymbol{H}$ simplifies the expression to

$$E(\boldsymbol{x}) \approx E_0 + \frac{1}{2}\sum_i \lambda_i q_i^2 + \mathcal{O}(\boldsymbol{x}^3), \tag{3.6}$$

where $\boldsymbol{x} = \sum q_i \boldsymbol{v_i}$ and $(\lambda_i, \boldsymbol{v_i})$ are the eigenpairs of the Hessian.

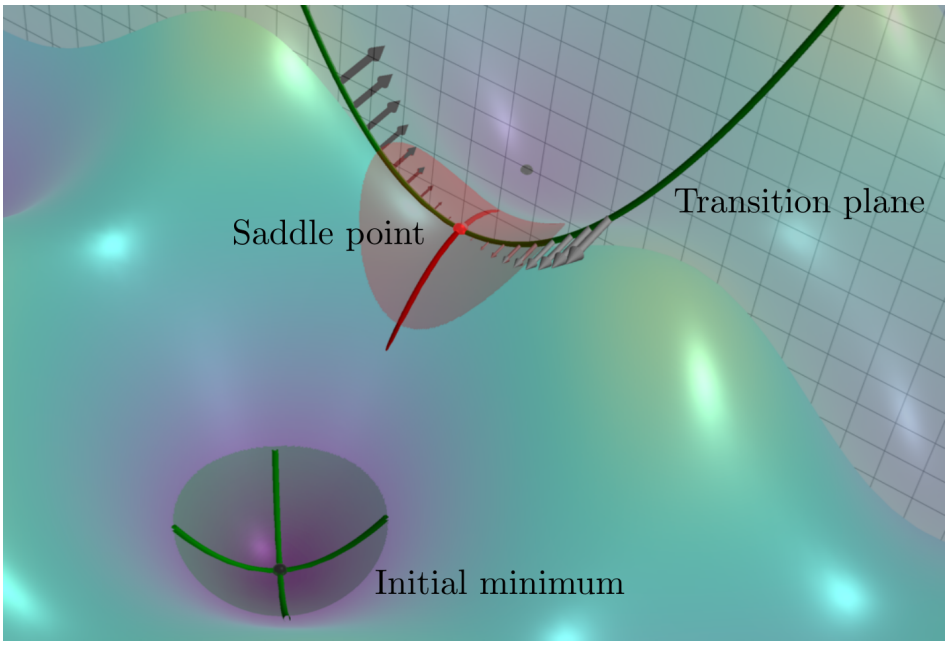


FIGURE 3.1
Illustration of harmonic transition state theory (HTST). In HTST, the rate is derived from harmonic expansions of the energy landscape (colored surface) around two stationary points – the initial minimum (black sphere) and the saddle point (red sphere). The harmonic expansion around the minimum/saddle point is indicated by a transparent (green/red surface). Additional parabolas are indicated along the two eigenvectors of the Hessian at the minimum and at the saddle point. These parabolas are colored red if the hessian eigenvalue is negative and green if it is positive. The transition plane hypersurface is indicated as a transparent white plane with rectangular grid lines. The perpendicular velocities for points within the transition plane are indicate by black arrows if they point towards the final state and gray arrows if they point towards the initial state. The further the point within the transition state is from the saddle point, the higher the perpendicular velocity.

3.2.1 The entropic contribution

In the canonical ensemble, the probability density function for the vector $\boldsymbol{x}$, up to normalization, in the harmonic approximation thus becomes

$$P(\boldsymbol{x}) \propto \exp\left(-\frac{1}{k_b T}\left[E_0 + \frac{1}{2}\boldsymbol{x}^T \boldsymbol{H} \boldsymbol{x}\right]\right), \tag{3.7}$$

which is easily recognized as a scaled $2n$-variate Gaussian distribution

$$\boldsymbol{x} \sim C \exp\left(-\frac{E_0}{k_b T}\right) \mathcal{N}(0, \boldsymbol{\Sigma}) \tag{3.8}$$

with zero mean and covariance matrix

$$\boldsymbol{\Sigma} = k_b T \boldsymbol{H}^{-1}. \tag{3.9}$$

At this point, it is important to realize that the probability density function $\mathcal{N}(0, \boldsymbol{\Sigma})$ is only defined if $\boldsymbol{\Sigma}$ is positive definite. If this is not the case, it is common practice to restrict the distribution to the $\operatorname{rank}(\boldsymbol{\Sigma})$-dimensional subspace over which $\boldsymbol{\Sigma}$ is positive definite.

In practical terms this means removing the zero-modes of the Hessian matrix [$\lambda_i = 0$ in (3.6)] from the integration domain. Even though the zero-modes are removed from the determinants, they still contribute to the rate expression via their configuration space volume, denoted by V_0 (for details see section 3.5). Overall, we compute the partition function as

$$\begin{aligned} Z &= \int \exp\left(-\frac{E(\boldsymbol{x})}{k_b T}\right) \mathrm{d}^{2n}\boldsymbol{x} \\ &= V_0 \exp\left(-\frac{E_0}{k_b T}\right) \int_{\boldsymbol{x}\in X^+} \exp\left(-\frac{1}{2}\boldsymbol{x}^T (\boldsymbol{\Sigma}^+)^{-1} \boldsymbol{x}\right) \mathrm{d}^k \boldsymbol{x}, \end{aligned} \tag{3.10}$$

where we factored out the zeromode volume V_0 and restricted the domain of integration to the subspace over which $\boldsymbol{\Sigma}$ is positive definite (hence the new symbol $\boldsymbol{\Sigma}^+$) and k is the number of non-zero modes of $\boldsymbol{H}$.

The last integral in (3.10) is well known from the normalization of multivariate Gaussians

$$\begin{aligned} &\int \exp\left(-\frac{1}{2}\boldsymbol{x}^T (\boldsymbol{\Sigma}^+)^{-1} \boldsymbol{x}\right) \mathrm{d}^k \boldsymbol{x} \\ =&\sqrt{2\pi}^k \sqrt{\det{}^+ \boldsymbol{\Sigma}}, \end{aligned} \tag{3.11}$$

where, in the last line, we introduced the $\det^+$ symbol, denoting a positive definite determinant. For further details on the computation of these, see Section. 3.4.1.

Using (3.11) to simplify (3.10), results in the final result for the partition functions

$$\begin{aligned} Z &= V^0 \exp\left(-\frac{E_0}{k_b T}\right) \sqrt{2\pi}^k \sqrt{\det{}^+ \boldsymbol{\Sigma}} \\ &= V^0 \exp\left(-\frac{E_0}{k_b T}\right) \sqrt{2\pi k_b T}^k \frac{1}{\sqrt{\det{}^+ \boldsymbol{H}}}. \end{aligned} \tag{3.12}$$

The ratio of partition functions becomes

$$\begin{aligned} \frac{Z^{\text{TS}}}{Z} &= \frac{V^{\text{SP}}}{V^{\text{M}}} \sqrt{2\pi k_b T}^{k^{\text{SP}} - k^{\text{M}}} \sqrt{\frac{\det{}^+ \boldsymbol{H}^{\text{M}}}{\det{}^+ \boldsymbol{H}^{\text{SP}}}} \exp\left(-\frac{E^{\text{SP}} - E^{\text{M}}}{k_b T}\right) \\ &= \frac{V^{\text{SP}}}{V^{\text{M}}} \sqrt{2\pi k_b T}^{N_0^{\text{M}} - N_0^{\text{SP}} - 1} \sqrt{\frac{\det{}^+ \boldsymbol{H}^{\text{M}}}{\det{}^+ \boldsymbol{H}^{\text{SP}}}} \exp\left(-\frac{\Delta E}{k_b T}\right), \end{aligned} \tag{3.13}$$

where $N_0^{\text{SP/M}}$ is the number of zero modes at the minimum and saddle point respectively.

Note: The additional -1 appearing in the exponent of $\sqrt{2\pi k_b T}$ in the second line of Eq. (3.13) stems from the fact that the integration domain to compute the partition function of the saddle point has one dimension less than the domain for the local minimum. This is because the saddle point has exactly one direction of negative curvature, which is excluded from the integration.

3.2.2 The dynamical contribution

The next task is to determine the dynamical contribution, which is the expected value of the positive part of the perpendicular velocity $v_\perp$,

$$\langle v_\perp \theta(v_\perp) \rangle_{\text{TS}} \tag{3.14}$$

which quantifies the rate at which the trajectories leave the transition state into the direction of the product state.

Like previous treatments of HTST, in atomistic spin dynamics, in the literature [109, 114, 129], we will derive it from a linearization of the LLG equation (1.24). Going further than these references, however, we will also include the *thermal* contributions to the perpendicular velocity, which result from including the stochastic noise term in the effective field of the linearized LLG.

As previously stated, the perpendicular velocity $v_\perp$ is the component of the velocity pointing along the transition state normal. In the harmonic approximation, the transition state is a hyperplane, passing through a first order saddle point[4] with its normal pointing along

[4] A first order saddle point is a stationary point (the gradient is zero) with exactly one direction of negative energy curvature.

the unstable mode at the saddle point configuration. Let the saddle point configuration be $s \in \mathcal{S}$ with Hessian $\boldsymbol{H}$, then the unstable mode $\boldsymbol{q} \in \mathcal{T}_s$ is the single eigenvector, with a negative eigenvalue

$$\boldsymbol{H}\boldsymbol{q} = \lambda^{-}\boldsymbol{q} \text{ where } \lambda^{-} < 0. \tag{3.15}$$

Since we require a first order saddle point, there exists exactly one such direction. In the following we represent q as a $3N_{\text{spin}}$ vector with N_{spin} constraints (see Sec. 1.1 for details), given by

$$\vec{q}_i \cdot \hat{s}s_i = 0 \quad \forall i. \tag{3.16}$$

First, we find an expression for the perpendicular velocity $v_\perp$ in the embedding space. Here, the unstable mode is a set of N_{spin} three-component vectors $\partial_t \vec{x}_i$, each of which is orthogonal to the saddle point spins $\hat{s}_i$ and the perturbations in the transition hyperplane.

The perpendicular velocity is found by computing the component of the rate of tangent space perturbations along the direction of the unstable mode:

$$\begin{aligned} v_\perp(x) &= \sum_i \vec{q}_i \cdot \partial_t \vec{x}_i \\ &= \sum_i \vec{q}_i \cdot \partial_t \vec{x}_i^{\text{P}} + \vec{q}_i \cdot \partial_t \vec{x}_i^{\text{D}}, \end{aligned} \tag{3.17}$$

where $\partial_t \vec{x}^{\text{P}}$ and $\partial_t \vec{x}^{\text{D}}$ are found according to the linearized LLG equation.

To derive the perpendicular velocity including thermal fluctuations, we make use of the linearized LLG equation [Equations (1.31) and (1.36)] and use the current realization of the stochastic noise as the gradient[5]

$$\vec{g}_i = \sqrt{2D}\vec{\xi}_i. \tag{3.18}$$

Obtaining the precessional contribution to the perpendicular velocity is straight forward and we get

$$\begin{aligned} v_\perp^{\text{P}}(\boldsymbol{x}, \boldsymbol{\xi}) =& \gamma'\sqrt{2D}\sum_i \vec{q}_i^T \operatorname{skew}(\hat{s}_i)\vec{\xi}_i \\ &-\gamma'\sqrt{2D}\sum_i \vec{q}_i^T \operatorname{skew}(\vec{\xi}_i)\vec{x}_j \\ &+\gamma'\sum_{ij} \operatorname{skew}(\hat{s}_i)\boldsymbol{H}^{ij}\vec{x}_j. \end{aligned} \tag{3.19}$$

The damping contribution only enters via the stochastic noise term. To see this, recognize that the integration variable $\boldsymbol{x}$ is constrained to

[5] Since the saddle point is a stationary point the gradient is purely stochastic and would vanish at zero temperature.

the hypersurface and, therefore, always orthogonal to $\boldsymbol{q}$

$$\boldsymbol{q}^T\boldsymbol{x} = \sum_i \vec{q}_i^{\,T}\vec{x}_i = 0. \tag{3.20}$$

Further, $\boldsymbol{q}$ has been chosen as an eigenvector of the Hessian matrix $\boldsymbol{H}$ and, therefore, the transition hyperplane is an invariant subspace of $\boldsymbol{H}$, meaning[6]

$$\boldsymbol{q}^T\boldsymbol{H}\boldsymbol{x} = \sum_{ij} \vec{q}_i\boldsymbol{H}^{ij}\vec{x}_j = 0 \quad \forall \boldsymbol{x} \in \ddagger. \tag{3.21}$$

Note: The symbol ‡ is a common shorthand for the transition hyperplane.

Using these two identities simplifies the damping contribution to the perpendicular velocity to

$$v_\perp^{\mathrm{D}}(\boldsymbol{\xi}) = -\gamma'\alpha\sqrt{2D}\sum_i \vec{q}_i^{\,T}\vec{\xi}_i. \tag{3.22}$$

Summarily, the perpendicular velocity depends on the perturbation within the transition hyperplane $\boldsymbol{x}$ and the instantaneous realization of the stochastic noise $\boldsymbol{\xi}$ and is given by the expression

$$\begin{aligned} v_\perp(\boldsymbol{x},\boldsymbol{\xi}) =& \gamma'\sqrt{2D}\sum_i \vec{q}_i^{\,T}\,\mathrm{skew}(\hat{s}_i)\vec{\xi}_i \\ &-\gamma'\sqrt{2D}\sum_i \vec{q}_i^{\,T}\,\mathrm{skew}(\vec{\xi}_i)\vec{x}_i \\ &+\gamma'\sum_{ij} \vec{q}_i^{\,T}\,\mathrm{skew}(\hat{s}_i)\boldsymbol{H}^{ij}\vec{x}_j \\ &-\gamma'\alpha\sqrt{2D}\sum_i \vec{q}_i^{\,T}\vec{\xi}_i. \end{aligned} \tag{3.23}$$

In the following, it will be useful to express the velocity as

$$v_\perp(\boldsymbol{x},\boldsymbol{\xi}) = \boldsymbol{a}^T\boldsymbol{x} + \boldsymbol{b}^T\boldsymbol{\xi} + \boldsymbol{x}^T\boldsymbol{Q}\boldsymbol{\xi} \tag{3.24}$$

where

$$\vec{a}_i = \gamma'\sum_j \boldsymbol{H}^{ij}\,\mathrm{skew}(\hat{s}_j)\vec{q_j}, \tag{3.25}$$

$$\vec{b}_i = -\gamma'\sqrt{2D}\left[\mathrm{skew}(\hat{s}_i)\vec{q_i} + \alpha\vec{q_i}\right], \tag{3.26}$$

and

$$\boldsymbol{Q}^{ij} = -\gamma'\sqrt{2D}\delta_{ij}\,\mathrm{skew}(\vec{q_i}). \tag{3.27}$$

[6] Intuitively, this means for perturbations within the transition hyperplane, the velocity always points back towards the saddle point.

The variance of the perpendicular velocity

For the dynamical contribution to the rate pre-factor we have to integrate over the stochastic noise terms. In other words: It is necessary to evaluate the expectation value

$$\langle v_\perp(\boldsymbol{x}, \boldsymbol{\xi})\theta[v_\perp(\boldsymbol{x}, \boldsymbol{\xi})]\rangle_{\boldsymbol{x},\boldsymbol{\xi}}, \tag{3.28}$$

where, both, $\boldsymbol{x}$ and $\boldsymbol{\xi}$ are multivariate Gaussian variables

$$\boldsymbol{x} \sim \mathcal{N}(\mathbf{0}, k_b T \boldsymbol{H}^{-1}), \tag{3.29}$$

and

$$\boldsymbol{\xi} \sim \mathcal{N}(\mathbf{0}, \boldsymbol{I}_{3N}). \tag{3.30}$$

We should remark on the dimensionality of $\boldsymbol{x}$, which is a vector in the tangent space of the saddle point configuration and, therefore, has $2N$ degrees of freedom. In the equations for the perpendicular velocity, however, we use the constrained $3N$ representation for ease of notation. When computing the variance, we have to keep in mind that not all $3N$ degrees of freedom are independent random variables. We rather have the following relationship

$$\boldsymbol{x}|^{\mathrm{3N}} = \boldsymbol{T}^T \boldsymbol{x}|^{\mathrm{2N}}, \tag{3.31}$$

with $\boldsymbol{x}|^{\mathrm{3N}} \in \mathbb{R}^{3N}$, $\boldsymbol{x}|^{\mathrm{2N}} \in \mathbb{R}^{2N}$ and where $\boldsymbol{T} \in \mathbb{R}^{3N\times 2N}$ is the tangent basis transformation.

If the distribution of the perpendicular velocity $v_\perp$ is Gaussian as well, the expectation value needed for the dynamical contribution can be computed by utilizing the one-dimensional Gaussian integral

$$\langle v_\perp \theta(v_\perp)\rangle = \frac{1}{\sigma\sqrt{2\pi}} \int_0^\infty v_\perp \exp\left(-\frac{v_\perp^2}{2\sigma^2}\right) \mathrm{d}v_\perp = \frac{\sigma}{\sqrt{2\pi}}, \tag{3.32}$$

where $\sigma = \sqrt{\mathrm{Var}(v_\perp)}$ is the standard deviation of $v_\perp$.

Unfortunately, $v_\perp$ only follows a Gaussian distribution if the stochastic noise term is neglected.[7] The good news is that the matrix $\boldsymbol{Q}$ is block diagonal and, thus, we are handed a big sum of non-Gaussian variables. Consequentially, we will make use of the central limit theorem, trusting that higher order moments will vanish, and approximate the distribution of the perpendicular velocity $v_\perp$ as Gaussian, which turns out to be an excellent approximation very quickly (see Fig. 3.2).

To make use of Eq. (3.32), we have to find the mean and variance of $v_\perp$. While the mean is trivially zero, the variance requires some simple algebra.

[7] Or more specifically, if $\boldsymbol{Q} = 0$ in (3.24) If this is not the case, the distribution of $v_\perp$ goes by the name of Generalized Chi-Square distribution.

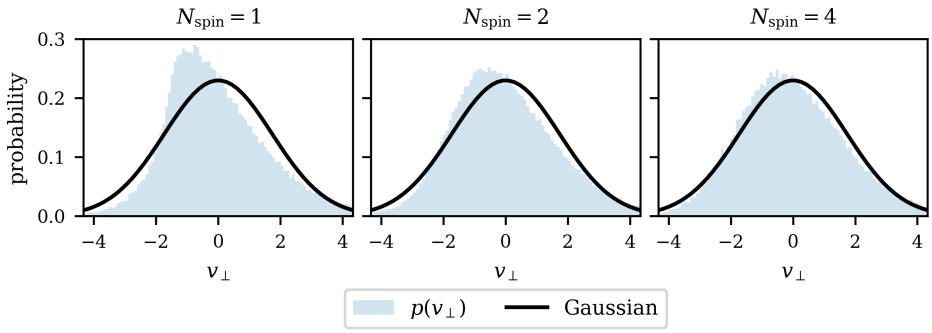


FIGURE 3.2
An illustration of how the probability density function of the perpendicular velocity $v_\perp$ approaches a Gaussian distribution as the number of spins increases. The reason is that the non-Gaussian contributions (due to interactions between thermal excitations in out of the transition-hypersurface and harmonic modes) decompose into a sum of non-Gaussian contributions over the number of spin components. As the number of spins increases the total probability distribution thus quickly approaches a Gaussian distribution, due to the central limit theorem.

First we will use the addition theorem of variances

$$\begin{aligned}\mathrm{Var}(v_\perp) = &\mathrm{Var}\left(\boldsymbol{a}^T\boldsymbol{x} + \boldsymbol{b}^T\boldsymbol{\xi} + \boldsymbol{x}^T\boldsymbol{Q}\boldsymbol{\xi}\right)\\ &= \mathrm{Var}\left(\boldsymbol{a}^T\boldsymbol{x}\right) + \mathrm{Var}\left(\boldsymbol{b}^T\boldsymbol{\xi}\right)\\ &+ \mathrm{Var}\left(\boldsymbol{x}^T\boldsymbol{Q}\boldsymbol{\xi}\right)\\ &+ 2\,\mathrm{Cov}\left(\boldsymbol{a}^T\boldsymbol{x}, \boldsymbol{x}^T\boldsymbol{Q}\boldsymbol{\xi}\right)\\ &+ 2\,\mathrm{Cov}\left(\boldsymbol{b}^T\boldsymbol{\xi}, \boldsymbol{x}^T\boldsymbol{Q}\boldsymbol{\xi}\right).\end{aligned} \tag{3.33}$$

Because the means of both Gaussian distributions are zero, the covariances in the equation above are also zero, as can be easily verified:

$$\begin{aligned}&\mathrm{Cov}\left(\boldsymbol{a}^T\boldsymbol{x}, \boldsymbol{x}^T\boldsymbol{Q}\boldsymbol{\xi}\right)\\ =&\langle \boldsymbol{a}^T\boldsymbol{x}\boldsymbol{x}^T\boldsymbol{Q}\boldsymbol{\xi}\rangle\\ =&\sum_{ikj}\langle a_i x_i x_j Q_{jk}\xi_k\rangle\\ =&\sum_{ikj}\langle a_i x_i x_j Q_{jk}\rangle \underbrace{\langle \xi_k\rangle}_{=0}\\ =&0.\end{aligned} \tag{3.34}$$

For the other term, the calculation looks much the same.

Hence, we simply add the variances of the three contributions. The variance of the first two terms in (3.24) is given by

$$\mathrm{Var}\left(\boldsymbol{a}^T\boldsymbol{x}\right) = k_B T \boldsymbol{a}^T\boldsymbol{H}^{-1}\boldsymbol{a} \tag{3.35}$$

and

$$\mathrm{Var}(\boldsymbol{b}^T\boldsymbol{\xi}) = \boldsymbol{b}^T\boldsymbol{I}_{3N}\boldsymbol{b} = \boldsymbol{b}^T\boldsymbol{b}. \tag{3.36}$$

And while the third term contains *products* of Gaussian distributions and, therefore, is *not* normal distributed itself. We can, of course, still compute the variance.

We start by finding the variance of two generic random vectors $\boldsymbol{u}^T\boldsymbol{v}$ under the assumption that $\boldsymbol{u}$ and $\boldsymbol{v}$ are distributed according to multivariate Gaussian distributions with zero mean and covariance matrices $\boldsymbol{\Sigma}_1$ and $\boldsymbol{\Sigma}_2$ respectively:

$$\boldsymbol{x} \sim \mathcal{N}(\boldsymbol{0}, \boldsymbol{\Sigma}_1) \tag{3.37}$$
$$\boldsymbol{y} \sim \mathcal{N}(\boldsymbol{0}, \boldsymbol{\Sigma}_2) \tag{3.38}$$

The variance of the scalar product of the two vectors is

$$\mathrm{Var}(\boldsymbol{x}^T\boldsymbol{y}) = \langle(\boldsymbol{x}^T\boldsymbol{y})^2\rangle - \underbrace{\langle\boldsymbol{x}^T\boldsymbol{y}\rangle^2}_{=0} \tag{3.39}$$
$$= \sum_{ij}\langle x_i x_j y_i y_j\rangle \tag{3.40}$$
$$= \sum_{ij}\langle x_i x_j\rangle\langle y_i y_j\rangle \tag{3.41}$$
$$= \sum_{ij}(\boldsymbol{\Sigma}_1)_{ij}\,(\boldsymbol{\Sigma}_2)_{ij} \tag{3.42}$$
$$= \mathrm{tr}\left[\boldsymbol{\Sigma_1}\boldsymbol{\Sigma_2}\right]. \tag{3.43}$$

Lastly, we use the fact that a linear transformation of a random variable distributed according to a multivariate Gaussian is a multivariate Gaussian itself:

$$\boldsymbol{y} \sim \mathcal{N}(\boldsymbol{\mu}, \boldsymbol{\Sigma}) \to \boldsymbol{Q}\boldsymbol{y} \sim \mathcal{N}(\boldsymbol{Q}\boldsymbol{\mu}, \boldsymbol{Q}^T\boldsymbol{\Sigma}\boldsymbol{Q}). \tag{3.44}$$

From (3.43) and (3.44), the variance of $\boldsymbol{x}^T\boldsymbol{Q}\boldsymbol{\xi}$ is readily obtained as

$$\mathrm{Var}(\boldsymbol{x}^T\boldsymbol{Q}\boldsymbol{\xi}) = k_bT\,\mathrm{tr}[\boldsymbol{H}^{-1}\boldsymbol{Q}^2]. \tag{3.45}$$

Summarily, we find the variance of the perpendicular velocity as

$$\mathrm{Var}(v_\perp) = k_bT\boldsymbol{a}^T\boldsymbol{H}^{-1}\boldsymbol{a} + \boldsymbol{b}^T\boldsymbol{b} - k_bT\,\mathrm{tr}\left[\boldsymbol{H}^{-1}\boldsymbol{Q}^2\right] \tag{3.46}$$

and, consequentially, the dynamical contribution is

$$\langle v_\perp\theta[v_\perp]\rangle_{\mathrm{TS}} = \sqrt{\frac{1}{2\pi}\,\mathrm{Var}(v_\perp)}. \tag{3.47}$$

If diffusion over the barrier is neglected [that means only taking the first term in (3.46)], the well known rate expression for HTST

in atomistic spin systems is recovered (compare e.g. to the original publication by Bessarab [129] or the more detailed presentation in Ref. [109]).

Remark: In the absence of diffusion over the barrier, the computation of the action of the inverse Hessian in Eq. (3.47) is not necessary, which is computationally advantageous. One simply has to expand the right-hand side $\boldsymbol{a}$-vector in the first term

$$\begin{aligned} &\boldsymbol{a}^T \boldsymbol{H}^{-1} \boldsymbol{a} \\ =&\boldsymbol{a}^T \boldsymbol{H}^{-1} \boldsymbol{H} \boldsymbol{p} \\ =&\boldsymbol{p}^T \boldsymbol{H}^T \boldsymbol{H}^{-1} \boldsymbol{H} \boldsymbol{p} \\ =&\boldsymbol{p}^T \boldsymbol{H} \boldsymbol{p}, \end{aligned} \tag{3.48}$$

where, due to Eq. (3.25),

$$\boldsymbol{p} = \gamma' \begin{pmatrix} \hat{s}_1 \times \vec{q}_1 \\ \vdots \\ \hat{s}_N \times \vec{q}_N \end{pmatrix}. \tag{3.49}$$

This was also observed by Lobanov et. al. [127, 165].

Theorem 1 (Variance algebra) *Let X and Y be two random variables. Then the following identity holds*

$$\mathrm{Var}(X+Y) := \mathrm{Var}(X) + 2\,\mathrm{Cov}(X,Y) + \mathrm{Var}(Y),$$

where the covariance $\mathrm{Cov}(X,Y)$ is defined by

$$\mathrm{Cov}(X,Y) := \langle XY \rangle - \langle X \rangle \langle Y \rangle.$$

If, further, X and Y are independent

$$\mathrm{Var}(XY) = \mathrm{Var}(X)\,\mathrm{Var}(Y) + \mathrm{Var}(X)\langle Y \rangle + \mathrm{Var}(Y)\langle X \rangle$$

Theorem 2 (Properties of multivariate Gaussians) *Let X_1 and X_2 be two independent and random variables, distributed according to the normal distributions $X_{1/2} \sim \mathcal{N}(\mu_{1/2}, \sigma^2_{1/2})$. Then, their weighted sum also follows a normal distribution*

$$\alpha X_1 + \beta X_2 \sim \mathcal{N}\left(\alpha\mu_1 + \beta\mu_2, \alpha^2\sigma_1^2 + \beta^2\sigma_1^2\right).$$

3.3 Single anisotropic spin flip

To see the benefits of including thermal contributions to the perpendicular velocity, let us consider the simple example of a single spin with one anisotropy axis, described by the Hamiltonian

$$\mathcal{H} = K(\hat{s} \cdot \hat{e}_z)^2. \tag{3.50}$$

For this spin system, the effective field is

$$\vec{b}^{\text{eff}}(\hat{s}) = -2K(\hat{s} \cdot \hat{e}_z)\hat{e}_z + \sqrt{2D}\,\vec{\xi}. \tag{3.51}$$

The minima of the system are

$$\hat{s}_{\text{min}} = \pm\hat{e}_z \tag{3.52}$$

and the saddle point is degenerate, because rotations around the equatorial plane do not change the energy of the system. The saddle points can be parametrized by the azimuthal angle ϕ

$$\hat{s}_{\text{SP}}(\phi) = \cos\phi\,\hat{e}_x + \sin\phi\,\hat{e}_y. \tag{3.53}$$

For the effective field at these saddle points we obtain

$$\vec{b}^{\text{eff}}(\hat{s}_{\text{SP}}(\phi)) = \sqrt{2D}\,\vec{\xi} \quad \forall\phi \tag{3.54}$$

and, therefore, the perpendicular velocity is zero, if the thermal contribution is not considered. For this reason the HTST theory without the thermal dynamical contribution predicts a rate of zero, which is clearly unphysical!

However, diffusion over the barrier still takes place and, therefore, the extended HTST rate gives a finite result of

$$\Gamma = \frac{2K}{k_b T}\sqrt{\frac{\alpha k_b T \gamma}{(1+\alpha^2)\mu\pi}}\exp\left(-\frac{K}{k_b T}\right). \tag{3.55}$$

For details of the calculation see Appendix A.1.

The rate obtained from this expression has been compared against explicit mean first passage time (MFPT) simulations with the stochastic LLG equation, using the z-component of the spin as a collective variable. The results of this comparison are depicted in Fig. 3.3 – the predicted lifetimes [the inverse of Eq. (3.55)] match the MFPT results within a factor of two.

As an, example of the MFPT method, the recorded passage times at a temperature of $T = 2\ K$ are shown in Fig. 3.4. It clearly exhibits the typical sigmoid shape and thus allows the extraction of a robust lifetime by taking the time difference of the sigmoid values at $\hat{s}_z = +1$ and $\hat{s}_z = -1$.

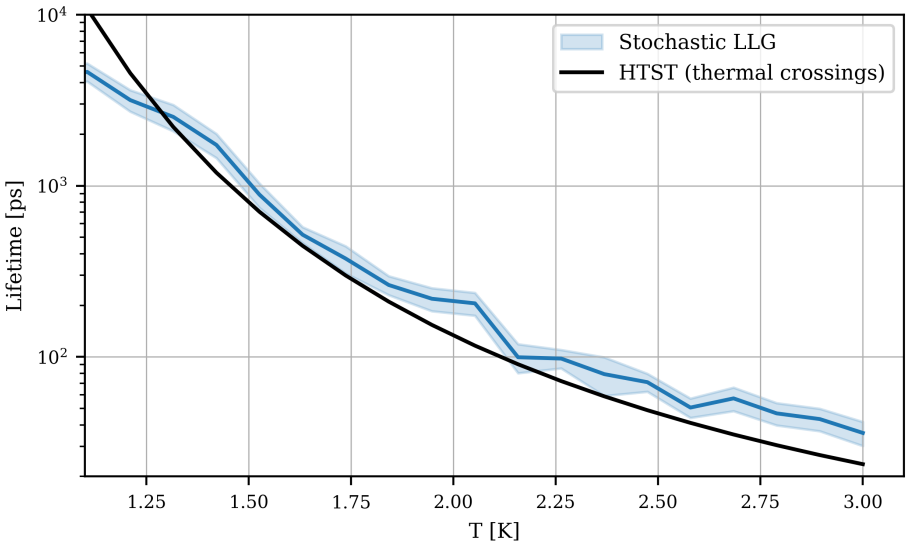


FIGURE 3.3
Lifetime vs temperature for the stochastic LLG (blue) and for the HTST theory with thermal crossings at the saddle point hypersurface (black).

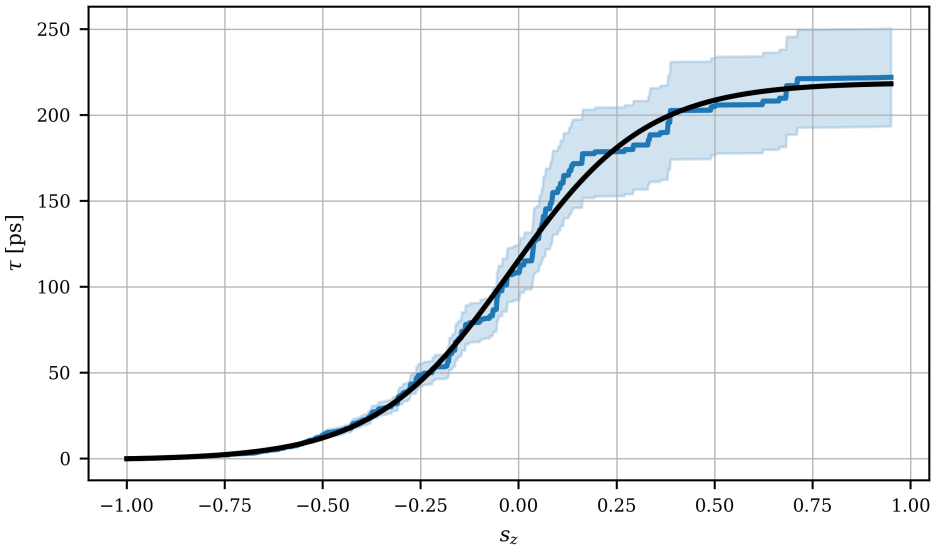


FIGURE 3.4
Mean first passage time of the z-component of the spin at a temperature of $T = 2$ K . Runs from 60 trajectories have been analyzed, all originating in the $\hat{s} = (0, 0, -1)$ state, an the average time the z-component crosses a certain threshold value (a point on the x-axis of the plot) has been determined. This average time is depicted as a dark blue line, and its standard deviation as an area shaded in a lighter blue color. A sigmoidal function (black line) has been fitted through through the mean first passage times.

3.4 Computation of determinants of large matrices

Due to the large number of spins involved in typical atomistic spin simulations, the Hessian matrix $\boldsymbol{H}$ can be exceedingly large and storing it in its entirety quickly becomes infeasible. A quick estimate shows that for a system of moderate size with 50^3 spins, the Hessian matrix has $4 \cdot 50^6$ entries, which when saved in 64 bit precision (the typical precision of floating point numbers on the CPU)[8] equates to 500 GB and would therefore saturate a typical cluster node. Finding the determinants of such large matrices is challenging, since it is computationally infeasible to find the product of all eigenvalues. In this section we will discuss two approaches towards this problem.

3.4.1 Positive definite determinants

As stated in Sec. 3.2.1, the determinants entering the entropic contribution to HTST [see Eq. (3.13)] need to be restricted to the positive-definite part of the eigenvalue spectrum. This means that negative eigenvalues and zero eigenvalues have to be removed from the spectrum – we will call this operation a positive-definite(PD)-determinant and denote it as $\det^+$. The PD-determinant can be computed from the eigenvalues as follows

$$\det{}^+(\boldsymbol{H}) := \prod_{\lambda_i > 0} \lambda_i. \tag{3.56}$$

In practice, we modify the definition of the PD-determinant slightly by introducing a finite threshold d and exclude all the eigenvalues below that threshold

$$\det{}^+(\boldsymbol{H}) = \prod_{\lambda_i > d} \lambda_i = \frac{\det(\boldsymbol{H})}{\prod_{\lambda_i \leq d} \lambda_i}. \tag{3.57}$$

The parameter d simply decides if we consider a mode with a given eigenvalue as a zero-mode or not. The purpose of this modification is to allow for some leeway in the definition of what is considered a Goldstone mode – since modes with a very small (but finite) eigenvalue might be more appropriately described as a zero-mode instead of a harmonic mode. Even translational modes tend to have a finite but small eigenvalue due to lattice effects.

[8] GPU simulations are often conducted with only 32 bit precision. Therefore, the Hessian matrix would take up half as much space. Considering, however, that VRAM is much more expensive than conventional RAM, the situation is not much better.

3.4.2 Sparse decomposition methods

The **sparse LU decomposition** is a powerful technique for computing the determinant of large sparse matrices. It decomposes a sparse matrix $\boldsymbol{A}$ into the product of a lower triangular matrix $\boldsymbol{L}$, an upper triangular matrix $\boldsymbol{U}$, and a permutation matrix $\boldsymbol{P}$ such that

$$\boldsymbol{P}\boldsymbol{A} = \boldsymbol{L}\boldsymbol{U}. \tag{3.58}$$

The determinant of $\boldsymbol{A}$ can be computed from the determinants of $\boldsymbol{L}$ and $\boldsymbol{U}$, which are easy to find since they are triangular matrices

$$\det(\boldsymbol{A}) = \det(\boldsymbol{P}) \cdot \det(\boldsymbol{L}) \cdot \det(\boldsymbol{U}). \tag{3.59}$$

Since $\boldsymbol{P}$ is a permutation matrix, $\det(\boldsymbol{P}) = \pm 1$. The determinants of $\boldsymbol{L}$ and $\boldsymbol{U}$ are the products of their diagonal elements

$$\det(\boldsymbol{L}) = \prod_{i=1}^{n} \boldsymbol{L}_{ii} \quad \text{and} \quad \det(\boldsymbol{U}) = \prod_{i=1}^{n} \boldsymbol{U}_{ii} \tag{3.60}$$

Thus, the determinant of $\boldsymbol{A}$ is

$$\det(\boldsymbol{A}) = \det(\boldsymbol{P}) \cdot \left(\prod_{i=1}^{n} \boldsymbol{L}_{ii} \right) \cdot \left(\prod_{i=1}^{n} \boldsymbol{U}_{ii} \right). \tag{3.61}$$

The **Cholesky decomposition** is another method used for solving linear systems and computing determinants, but it is applicable only to symmetric positive definite matrices. It decomposes a matrix $\boldsymbol{A}$ into

$$\boldsymbol{A} = \boldsymbol{L}\boldsymbol{L}^T, \tag{3.62}$$

where $\boldsymbol{L}$ is a lower triangular matrix. The determinant can be computed as

$$\det(\boldsymbol{A}) = \det(\boldsymbol{L})^2 = \left(\prod_{i=1}^{n} \boldsymbol{L}_{ii} \right)^2. \tag{3.63}$$

However, if a matrix has even a single negative eigenvalue, it is not positive definite, and the Cholesky decomposition will fail. In the context of HTST, we are unfortunately sure to encounter this situation due to the negative eigenvalue at the saddle point.

It is tempting to consider a deflation method to lift the single negative eigenvalue at the saddle point by using a projector onto the negative eigenvector. Indeed the Hessian at the saddle point can easily be modified in such a way

$$\boldsymbol{H}^{\text{SP}}_{\text{mod}} = \boldsymbol{H}^{\text{SP}} + (1 - \lambda)\boldsymbol{q}\boldsymbol{q}^T, \tag{3.64}$$

where $\lambda < 0$ is the negative eigenvalue and $\boldsymbol{q}$ is the associated eigenvector. It is easily verified that

$$\det(\boldsymbol{H}^{\text{SP}}_{\text{mod}}) = \det{}^{+}(\boldsymbol{H}^{\text{SP}}), \tag{3.65}$$

since the eigenvector $\boldsymbol{q}$ of $\boldsymbol{H}^{\mathrm{SP}}$ with negative eigenvalue λ also is an eigenvector of $\boldsymbol{H}^{\mathrm{SP}}_{\mathrm{mod}}$, but with eigenvalue 1 and therefore does not influence the value of the determinant. The bad news is that this so-called deflation destroys sparsity, since the projection operator $\boldsymbol{q}\boldsymbol{q}^T$, in the general case, is *not* sparse. Hence, (3.64) is useless for sparse matrix decomposition methods.

Consequently, the sparse LU decomposition is the method of choice for finding the determinants in an HTST calculation without explicit dipole-dipole interactions. General purpose sparse LU decomposition are implemented in a variety of software packages, for example the SuperLU package [167] or the Eigen3 [168] library. However, it should be noted that these libraries, while making good use of the sparsity, still suffer from a a phenomenon called fill-in. Fill-in (in this context) simply means that the factors of the LU decomposition contain many more non-zero entries than the original matrix itself. Unfortunately, this means at certain system sizes the computation of the determinant runs out of memory. As an example, the determinants for a Hopfion in a simulation box of 64^3 spins (see Section 4.2) could not be determined due to memory limitations on a compute node with 256 GB of working memory. One way to circumvent these limitations is to use our knowledge of the pattern of the non-zero entries in the Hessian: Like described by Lobanov & Uzdin [165], the band-diagonal structure[9] makes is possible to write a specialized version of the LU decomposition with less fill-in.

Combining standard determinants with partial diagonalization

Unfortunately, Equation (3.56) requires knowledge of all the eigenvalues, which for small matrices is not a problem – for large matrices, however, one frequently wishes to compute the determinant, *without* finding all individual eigenvalues. For this purpose, one can make use of the following trivial identity, which, besides the determinant, only requires knowledge of all the negative and zero eigenvalues:

$$\det{}^{+}(\boldsymbol{H}) = \frac{\prod_{\lambda_i>0}\lambda_i}{\prod_{\lambda_i\leq 0}\lambda_i} = \frac{\det(\boldsymbol{H})}{\prod_{\lambda_i\leq 0}\lambda_i}. \tag{3.66}$$

Finding the negative and zero eigenvalues with a partial diagonalization algorithm (like for example Lanczos method [157]) and computing the determinant by other means is a way to make these calculations much more efficient, while leveraging standard methods for determinants and partial diagonalization.

The PD-determinant would then be computed in a two-step procedure:

[9] If the boundary conditions are periodic there are some spurious entries at the edges, which can, however, be dealt with.

1. Find the regular determinant $\det(\boldsymbol{H})$ using an efficient method like the sparse LU decomposition or the Cholesky decomposition
2. Remove the eigenvalues below the threshold by division [Eq. (3.66)]

However, upon inspection of Eq. (3.66), a problem becomes obvious: If any of the eigenvalues in the divisor are zero, the result is undefined. Going further, even if any of the eigenvalues becomes small (compared to the numerical error in the partial diagonalization) the accuracy of (3.56) suffers a lot. Unfortunately, we are almost sure to encounter such cases in our HTST calculations, due to symmetries in the investigated solitons and the Goldstone modes arising from those.

Diagonal shift

One possibility to shift the eigenvalues of Goldstone modes away from zero, *without* destroying the sparsity of the resulting matrix, is to add a scaled identity matrix $\alpha\boldsymbol{I}$ with a shift magnitude α. We can then compute the PD-determinant of the shifted matrix instead

$$\det{}^+(\boldsymbol{H}+\alpha\boldsymbol{I}) = \frac{\det(\boldsymbol{H}+\alpha\boldsymbol{I})}{\prod_{i<k}(\lambda_i+\alpha)}. \tag{3.67}$$

We can estimate by how much this shift changes the PD-determinant by inspecting the relative difference. First, assume that there are k eigenvectors of $\boldsymbol{H}$ with eigenvalues λ_1 to λ_k, with $\lambda_k < 0$.

To compute the relative difference between the shifted PD-determinant and the true PD-determinant, we inspect the absolute differences of the logarithms

$$\begin{aligned}
\varepsilon_{\log} &:= \log(\det{}^+(\boldsymbol{H}+\alpha\boldsymbol{I})) - \log(\det{}^+\boldsymbol{H}) && (3.68)\\
&= \sum_{i=k+1}^{n} \log\left(\frac{\lambda_i+\alpha}{\lambda_i}\right) && (3.69)\\
&= \left[\sum_{i=k+1}^{n}\frac{1}{\lambda_i}\right]\alpha - \left[\frac{1}{2}\sum_{i=k+1}^{n}\frac{1}{\lambda_i^2}\right]\alpha^2 + \mathcal{O}(\alpha^3) && (3.70)
\end{aligned}$$

The relative difference can be computed from the absolute differences of the logarithm as

$$\begin{aligned}
&\left|\frac{\det{}^+(\boldsymbol{H}+\alpha\boldsymbol{I}) - \det{}^+(\boldsymbol{H})}{\det{}^+(\boldsymbol{H})}\right| && (3.71)\\
&= \exp\left(\varepsilon_{\log}\right) - 1 && (3.72)\\
&\approx \exp\left(\left[\sum_{i=k+1}^{n}\frac{1}{\lambda_i}\right]\alpha\right) - 1. && (3.73)
\end{aligned}$$

Clearly, due to the exponential growth in the error, it would be wise to choose a small non-zero value for α. We cannot make α too small though, since then we circle back to the original problem, due to the *relative* error of the divisor in (3.67) tending towards very large values. In the following section we will investigate the interplay of both these sources of errors more closely.

Numerical errors in the partial diagonalization

Assume that we know the k eigenvectors we have to exclude (because their eigenvalue is below the threshold d) are λ_1 to λ_k, and that, from partial diagonalization, we know these eigenvalues up to a numerical error σ. To model such a situation we write our estimate of the eigenvalues as

$$\lambda_i' = \lambda_i + \xi_i, \tag{3.74}$$

where ξ is a random variable, drawn from a Gaussian distribution with zero mean and variance σ^2.

Taking the uncertainty from the partial diagonalization into account, let us inspect the outcome of computing the shifted determinant and dividing by the eigenvalues below the threshold,

$$P = \frac{(\lambda_1+\alpha)\dots(\lambda_k+\alpha)}{(\lambda_1+\alpha+\xi_1)\dots(\lambda_k+\alpha+\xi_k)}(\lambda_{k+1}+\alpha)\dots(\lambda_n+\alpha) \tag{3.75}$$

$$= f(\xi_1,\dots,\xi_k)\det{}^+(\boldsymbol{H}+\alpha\boldsymbol{I}). \tag{3.76}$$

Clearly the uncertainty in the eigenvalues below the threshold has introduced a statistical pre-factor $f(\xi_1,\dots,\xi_k)$. Since the expectation value of the ξ_i is zero, the expectation value of $f(\xi_1,\dots,\xi_k)$ is one.

We will, again, inspect the absolute difference in the logarithm of the PD-determinant

$$\varepsilon_{\log}(\xi_1,\dots,\xi_k) = \log\left[f(\xi_1,\dots,\xi_k)\det{}^+(\boldsymbol{H}+\alpha\boldsymbol{I}) - \det{}^+(\boldsymbol{H})\right] \tag{3.77}$$

$$= \varepsilon_{\log} + \log\left(f(\xi_1,\dots,\xi_k)\right). \tag{3.78}$$

By re-arranging (3.78), we arrive at an expression for the actual PD-determinant:

$$\log\det{}^+\boldsymbol{H} = \log\det{}^+(\boldsymbol{H}+\alpha\boldsymbol{I}) - \mathrm{tr}(\boldsymbol{H}^{-1})\alpha + \log\left(f(\xi_1,\dots,\xi_k)\right) \tag{3.79}$$

The standard deviation of $\log\left(f(\xi_1,\dots,\xi_k)\right)$ can be approximated by

$$\sqrt{\langle\log^2 f(\xi_1,\dots,\xi_k)\rangle_{\xi_1,\dots,\xi_k}} \tag{3.80}$$

$$\approx\sqrt{\sum_{i=1}^{k}\frac{\sigma_i^2}{(\alpha+\lambda_i)^2}}. \tag{3.81}$$

Overall, we arrive at the following expression

$$\begin{aligned}\log\det{}^{+}\boldsymbol{H} =& \log\det{}^{+}(\boldsymbol{H}+\alpha\boldsymbol{I}) - \operatorname{tr}(\boldsymbol{H}^{-1})\alpha \\ &+\sqrt{\sum_{i=1}^{k}\frac{\sigma_i^2}{(\alpha+\lambda_i)^2}} \\ &+\mathcal{O}\left(\frac{\alpha^2}{\operatorname{tr}(\boldsymbol{H}^{-2})}\right).\end{aligned} \tag{3.82}$$

The idea is now to choose a value of α, which fulfills both $\alpha \gg \lambda_k$ and $\alpha \ll \sqrt{\operatorname{tr}(\boldsymbol{H}^{-2})}$. Then, we can use a linear extrapolation to find $\log\det{}^{+}\boldsymbol{H}$.[10] In general, this requires a significant spectral gap between λ_k and λ_{k+1}. In the setting of HTST calculations, this is generally the case. While, we do know the analytical expression for the linear slope in Eq. (3.82), which is given by the trace of the inverse Hessian a direct computation of the slope is generally not feasible or necessary. It can be inferred by performing computations with two different shift values α_i and using a linear interpolation. See also Figure. 3.5 for a visualization.

It is not immediately clear how to find the optimal region of α for the interpolation. It is however possible to make a few simplifying assumptions to obtain a reasonable estimate. We assume a linear spectrum between λ_{k+1} and λ_n, we can then approximate the trace of the inverse as (further assuming $n \to \infty$ and $\lambda_n \gg \lambda_{k+1}$)

$$\operatorname{tr}[\boldsymbol{H}^{-1}] \approx \frac{1}{\lambda_n}\int\frac{1}{x}\mathrm{d}x = \frac{1}{\lambda_n}\log\left(\frac{\lambda_n}{\lambda_{k+1}}\right) \tag{3.83}$$

and for the trace of the inverse square

$$\operatorname{tr}[\boldsymbol{H}^{-2}] \approx \frac{1}{\lambda_n}\int\frac{1}{x^2}\mathrm{d}x \approx \frac{1}{\lambda_n\lambda_k}. \tag{3.84}$$

So if we require

$$\begin{aligned}&\alpha\operatorname{tr}[\boldsymbol{H}^{-1}] \gg \alpha^2\operatorname{tr}[\boldsymbol{H}^{-2}] \\ \iff\quad &\alpha \ll \frac{\operatorname{tr}[\boldsymbol{H}^{-1}]}{\operatorname{tr}[\boldsymbol{H}^{-2}]},\end{aligned}$$

we can approximately choose

$$\alpha \ll \frac{\operatorname{tr}[\boldsymbol{H}^{-1}]}{\operatorname{tr}[\boldsymbol{H}^{-2}]} \tag{3.85}$$

$$\rightsquigarrow\quad \alpha \ll \lambda_k\log\left(\frac{\lambda_n}{\lambda_k}\right). \tag{3.86}$$

[10] It is, of course, also possible to extrapolate using higher order polynomials.

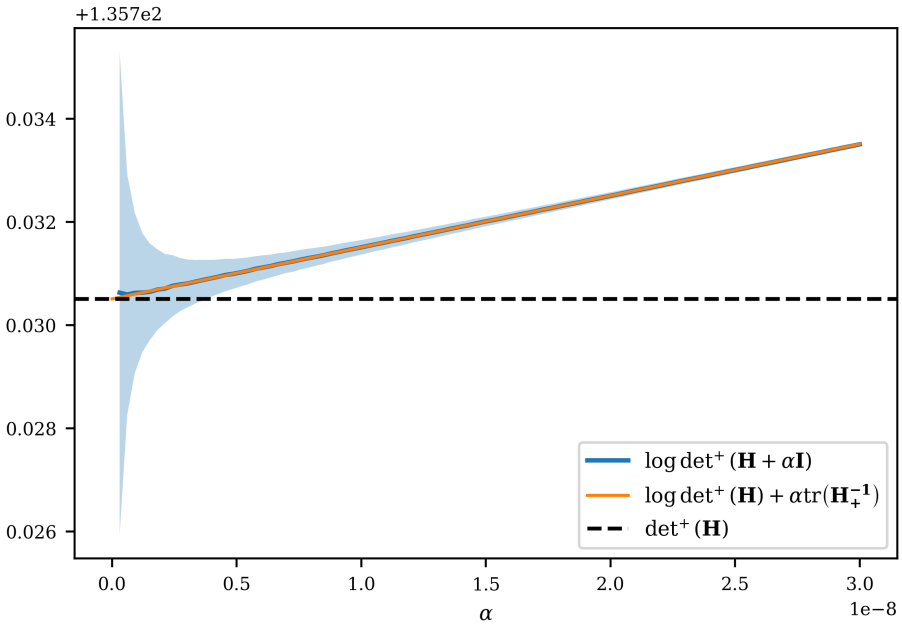


FIGURE 3.5
Shifted log determinant versus shift value α in a toy example. (Blue) Logarithm of shifted PD-determinant with simulated Gaussian noise. The test matrix $\boldsymbol{H}$ had a linear spectrum with two small eigenvalues to be excluded with $\lambda_1 = \lambda_2 = 10^{-12}$, the first not excluded eigenvalue was $\lambda_3 = 10^{-5}$ and the last eigenvalue was $\lambda_1 00 = 12$. The standard deviation of the simulated Gaussian noise was $\sigma_{\lambda_{0/1}} = 10^{-12}$. The resulting standard deviation on the $\log\det^+(\boldsymbol{H} + \alpha\boldsymbol{I})$ is shown by the blue shaded region. (Orange) The linear extrapolation expression. (black) The value of the true log determinant $\log\det^+(\boldsymbol{H})$

The advantage of Eq. (3.86) is its simplicity and that it requires only knowledge of the largest eigenvalue. It is, of course, an extremely rough approximation and in a real application the spectrum will not be exactly linear and thus, to find a suitable range of shifts, careful validation is required. Generally speaking, the low parts of the spectrum are much more important than the higher eigenvalues[11] and the slower the eigenvalues grow, the lower α needs to be and vice versa.

To increase the accessible range of the shift α, it is of course also possible to fit higher order polynomials to the logarithms of the shifted PD-determinants. In such a case it is important to verify that the signs of the polynomial pre-factors are alternating, starting with a positive sign for the linear term.

[11] As can also be seen by the fact that λ_n only enters Eq. (3.86) through the logarithm.

3.4.3 Statistical sampling with the Hutchinson trace estimator

For dense Hessians, or extremely large sparse Hessians, the direct decomposition methods are not feasible. In these cases, we can make use of an algorithm described by Han *et al.* [169]. The idea is to transform the problem of finding the determinant, into the question of finding the trace by using the identity, which holds for positive definite matrices

$$\log\det(\boldsymbol{M}) = \mathrm{tr}[\log \boldsymbol{M}]. \tag{3.87}$$

The algorithm proceeds by generating a set of random vectors $\boldsymbol{v}^1$,$\boldsymbol{v}^2$, ..., $\boldsymbol{v}^N$, where each component is drawn from a so-called Rademacher random distribution $[\boldsymbol{v}^i]_j = \pm 1$ with $P(+1) = P(-1) = \frac{1}{2}$. Then, the product $\boldsymbol{v}^i \cdot \log \boldsymbol{M}\boldsymbol{v}^i$ is approximated for each $\boldsymbol{v}^i$. Averaging these product values gives an estimate of $\mathrm{tr}(\log \boldsymbol{M})$. To estimate the logarithm of the matrix, a polynomial expansion of the $\log$ function is used

$$\log(x) \approx \sum_{i=1}^{d} p_i(x). \tag{3.88}$$

Therefore, the individual terms of the polynomials require powers of the matrix $\boldsymbol{M}$. It turns out that using an expansion Chebyshev polynomials is especially suited to this task, as opposed to e.g a regular taylor expansion [169]. The required matrix-vector products can be efficiently computed via recursion, without ever having to form the full matrices $\boldsymbol{M}^n$ for any power n.

Thus, this algorithm is also amenable to the aforementioned deflation techniques (3.64) and near-zero eigenvalues as well as the negative eigenvalues can be eliminated and thus the positive-definite determinant can be computed. Of course the discussion in Sec. 2.3 of Chap. 2, about how to compute Hessian-vector products by finite differences applies to this algorithm as well.

Another way to apply this algorithm to non-positive definite matrices is to use the identity $\det(\boldsymbol{M}) = \frac{1}{2}\det(\boldsymbol{M}^T\boldsymbol{M})$ as described by Han *et al.* [169].

See Fig. 3.6 for a demonstration of the Hutchinson trace estimator to find the log-determinant of a small Skyrmion in a system with 30×30 lattice sites. In the plot on the top of Fig. 3.6, it can be seen how the mean of the samples quickly stabilizes for as little as 50 samples, after which further sampling only reduces the standard deviation, which is shown as shaded areas around the mean. The difference between the mean and an accurate result from LU decomposition is only further reduced by increasing the degree of the Chebyshev expansion. The dependence of the mean and standard deviation of the computed determinant samples on the number of degrees of the Chebyshev expansion is shown in the bottom.

Fig. 3.6 also presents a good opportunity to discuss a problem of this method: The standard deviation of the log-determinant decreases only slowly with the number of Rademacher samples (approximately as $1/\sqrt{N_{\text{samples}}}$) and increases with the magnitude of the off-diagonal elements (for a diagonal matrix this algorithm would be excellent) – for details see Ref. [170]. If we were only interested in a single determinant, this would not be a huge concern, since the relative error on the log-determinant is still acceptable. For the purpose of HTST, however, we need to find the ratio of PD determinants to compute the ratio of harmonic partition functions [see Eq. (3.13)]. This means we need the *difference* of log determinants with high accuracy, meaning extremely long sampling would be necessitated to guarantee an accurate life time result. See for example the derived convergence properties by Han *et al.* [169]. It may be necessary to somehow devise a sampling scheme for the $(H^{\text{SP}})^{-1}\boldsymbol{H}^{\text{Min}}$ matrix as a whole or otherwise pre-condition the matrices e.g. with an incomplete LU factorization to increase the similarity to a diagonal matrix. For the HTST results in this thesis, we have therefore preferred the sparse LU factorization method coupled with the previously described extrapolation technique.

3.5 Goldstone modes

As stated in the preceding section, the calculation of transition rates with the harmonic transition state theory requires a separate treatment of zero-modes.

3.5.1 Transition between zero-modes and harmonic modes

In practice, frequently none of the eigenvalues will truly be zero.[12]. Due to the crystal lattice, solitons have preferred positions and orientations and the eigenvalues associated to e.g a translation to a different lattice site will be small, but greater than zero. At a low enough temperature, the soliton will simply not move from its preferred lattice site, while at a larger temperature it might easily translate over the lattice. A further complication is that the translational eigenvalues at the minimum and the saddle might well be different, and not including the same number of zero-modes introduces an unphysical scaling with the size of the simulation box. All of these problems raise the

[12] One exception are spin rotation modes in a Hamiltonian with only exchange interactions – A system which we will encounter later on when studying Hopfions in frustrated bulk magnets.

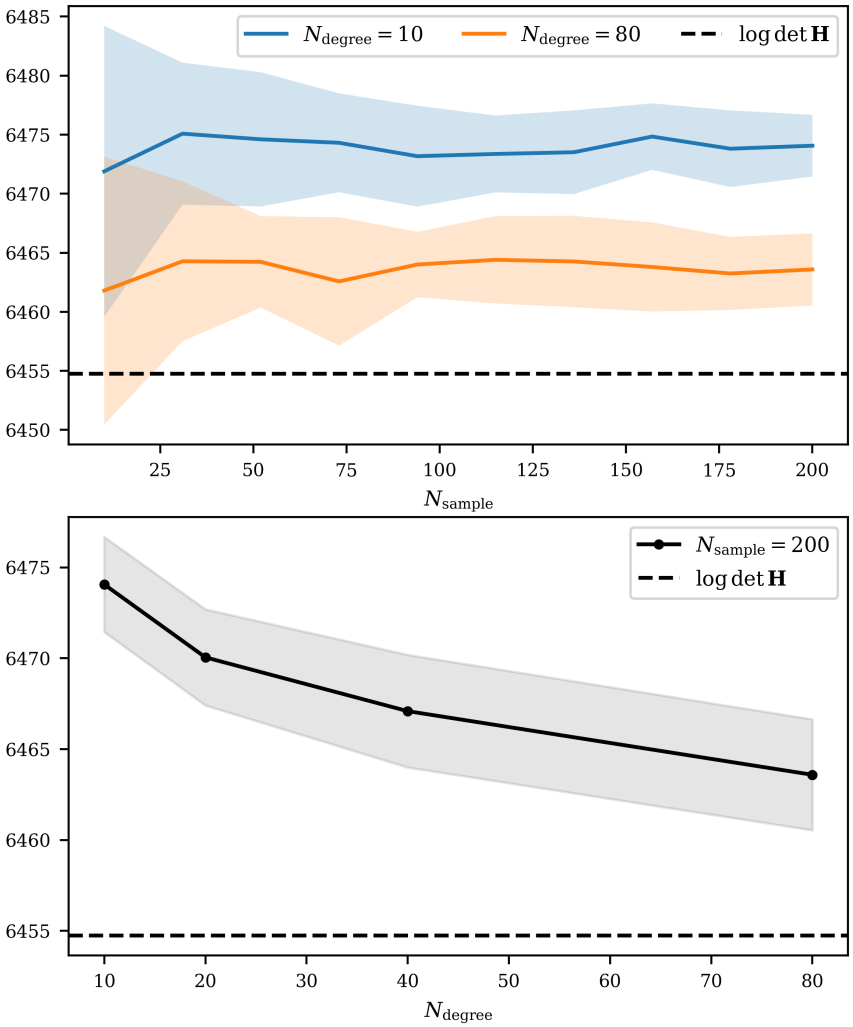


FIGURE 3.6

Determinant obtained from the Hutchinson sampler. The test matrix had 1800×1800 entries and corresponds to the hessian of a small Skyrmion (with nearest neighbor interactions) in a system with 30×30 lattice sites. The two minimum eigenvalues with a value of $4.5 \cdot 10^{-}5$, were removed via deflation, and the maximum eigenvalue was 85.5. (Top:) The plot shows results from the Hutchinson sampling versus the number of Rademacher samples (N_{samples}) for two different maximum degrees of the expansion of the $\log$-function in Chebyshev polynomials. The mean value for $N_{\text{degree}} = 10$ is shown as a blue line, with a shaded area behind it for the standard deviation. For $N_{\text{degree}} = 80$, the results are shown in the same manner, but with an orange color. An accurate result for the positive definite log determinant (from LU decomposition) is shown as a horizontal black and dashed line. (Bottom:) The plot shows how the average determinant (black line) approaches approaches the accurate positive definite Log determinant as the number of degrees is increased, while keeping the number of samples at a constant $N_{\text{samples}} = 200$.

question of how the transition from harmonic modes to zero-modes takes place. To shed some light on this issue, we will first perform some simple calculations in a one-dimensional toy-model, that (in some sense) includes the periodicity of the lattice and the effect of the curvature around the local energy minimum.

Assume the energy in the direction of a low eigenvalue mode is connected to a discrete symmetry such that the energy is given by the following cosine model:

$$E(x) = A\left[1 - \cos\left(\frac{2\pi}{a}x\right)\right]. \tag{3.89}$$

The second derivative of (3.89) at the origin is given by

$$\frac{\partial^2}{\partial x^2}E(x)\bigg|_{x=0} = \lambda = \frac{4\pi^2}{a^2}A, \tag{3.90}$$

therefore we set

$$A = \frac{a^2}{4\pi^2}\lambda, \tag{3.91}$$

and thus obtain a periodic energy that matches the curvature at the stationary point. The energy of the cosine model, as well as the harmonic approximation, are depicted in Fig. 3.7 a).

We can obtain the contribution to the partition function from this mode by performing the integration over one period of the potential

$$\begin{aligned} Z &= \int_{-a/2}^{a/2} \exp\left(-\frac{E(x)}{k_B T}\right) \mathrm{d}x && (3.92)\\ &= \frac{a}{2\pi}\exp\left(-\frac{A}{k_B T}\right)\int_{-\pi}^{\pi}\exp\left(\frac{A}{k_b T}\cos(u)\right)\mathrm{d}u && (3.93)\\ &= a\exp\left(-\frac{A}{k_B T}\right)\mathrm{I}_0\left(\frac{A}{k_b T}\right) && (3.94)\\ &= a\exp\left(-\frac{a^2\lambda}{4\pi^2 k_B T}\right)\mathrm{I}_0\left(\frac{a^2\lambda}{4\pi^2 k_B T}\right) && (3.95) \end{aligned}$$

where I_0 is the modified Bessel function of the first kind of zeroth-order.

On the other hand, the partition function in case for the harmonic approximation is

$$\begin{aligned} Z_{\text{harmonic}} &= \int_{-\infty}^{\infty}\exp\left(\frac{-\lambda x^2}{2k_B T}\right)\mathrm{d}x && (3.96)\\ &= \sqrt{\frac{2\pi k_B T}{\lambda}}, && (3.97) \end{aligned}$$

while for the approximation as a Goldstone mode, it simply is

$$Z_{\text{goldstone}} = \int_{-a/2}^{a/2}\mathrm{d}x = a. \tag{3.98}$$

Fig. 3.7 b), illustrated the transition from a harmonic mode to a Goldstone mode as the temperature increases. Further, by computing the intersection point between the harmonic approximation and the zeromode approximation we can define the following rough criterion for a translational mode with eigenvalue λ to be treated as a harmonic mode

$$T \lessapprox \frac{1}{2\pi k_B} a^2 \lambda \tag{3.99}$$

3.6 Mode volumes of solitons

To apply the simple one-dimensional model discussed in Section 3.5.1 [including the approximation as a Goldstone mode (3.98)], to an actual soliton, like a Skyrmion or a Hopfion, we have to find a connection between the coordinates in the tangent space of the stationary point (in the one-dimensional model this corresponds to the integration variable x) and the distances in the simulation box (the period of the cosine potential a). For the harmonic modes, this is not necessary since only the curvature λ and the temperature was required to compute the contribution to the partition function Z_{harmonic} in (3.97). As we will see in the following, the necessary connection between these length scales, is given by the length of the modes.

We will assume the case a mode described by the infinitesimal action on each spin in the system

$$\hat{s}_i(\varepsilon) = \hat{s}_i + \varepsilon \vec{k}_i + \mathcal{O}(\varepsilon^2), \tag{3.100}$$

where the vector $\vec{k}$ represents three components of the *normalized*[13] $3N_{\text{spin}}$ dimensional mode $\hat{\boldsymbol{k}} \in \mathbb{R}^{3N_{\text{spin}}}$, where N_{spin} is the number of spins. The contribution to the partition function would then be

$$Z = \int_0^a B(\varepsilon) \mathrm{d}\varepsilon, \tag{3.101}$$

where $B(\varepsilon) = \exp\left(-\frac{E(\varepsilon)}{k_B T}\right)$ is the Boltzmann weight and we will leave the integration limit a unspecified for now. We clearly have the relation

$$\varepsilon = \sqrt{\sum_i \left|\hat{s}_i(\varepsilon) - \hat{s}_i\right|^2} := \left|\hat{s}(\varepsilon) - \hat{s}\right|. \tag{3.102}$$

In the application to numerical simulations, we might want to compute the mode contribution from N discrete samples of a mode

[13] Normalizing the mode simplifies things, since then the eigenvalue of the Hessian and the second derivative of the energy with regards to ε coincide.

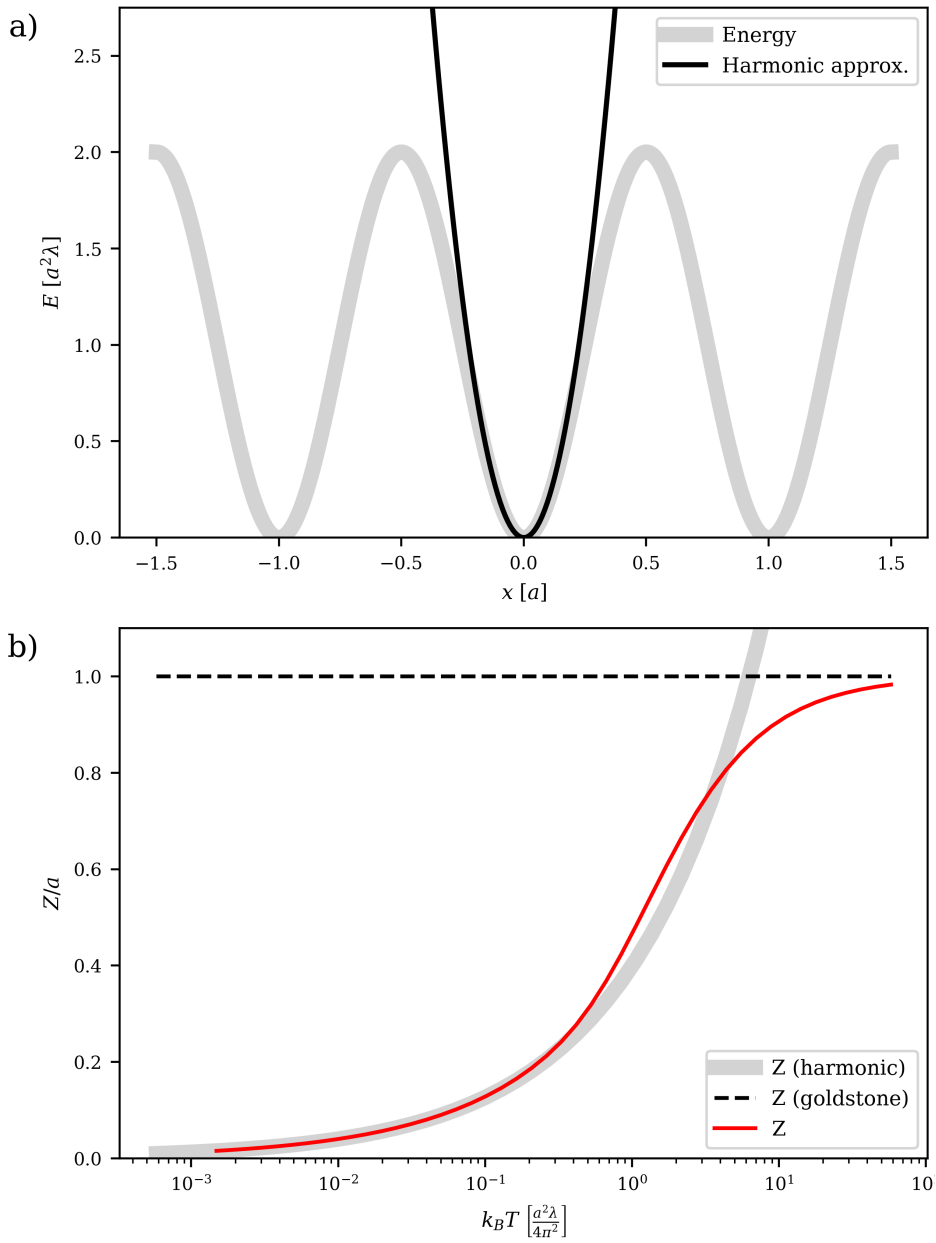


FIGURE 3.7
The transition between a Goldstone mode and a harmonic mode in the one-dimensional model with cosine shaped energy. a) The true energy of the one-dimensional cosine model [see (3.89)] is shown as a thick light gray line. The harmonic approximation of energy basin at the origin is shown as a thinner black line. b) The contribution to the partition function of a single potential period (the hop to an adjacent energy basin). The dashed black line shows the result from the goldstone mode approximation (3.98) and the thick gray line shows the approximation as a harmonic mode (3.97). The red curve [see (3.95)] interpolates between the two asymptotic limits (harmonic at low temperatures) and Goldstone at high temperatures.

following algorithm. Let these samples be denoted by

$$\{\hat{s}_i^{(j)}\}_{j=1\ldots N}. \tag{3.103}$$

Due to (3.102), we can approximate the integral (3.101) as a Riemann sum

$$Z \approx \sum_{j=0}^{N-1} B\left(\hat{s}^{(j)}\right) \left|\hat{s}^{(j+1)} - \hat{s}^{(j)}\right|. \tag{3.104}$$

Following modes of low eigenvalues to compute more accurate life times expensive, but has, for example, been done by Malottki *et al.* [171]. In the following, we will examine techniques to construct zeromodes from a-priori information and how to use these constructed modes to evaluate zero-mode volumes or even to apply an approximation like (3.95).

3.6.1 Constructing modes

Consider the situation, where we have a system of N_{spin} discrete normalized spins $\{\hat{s}_i\}$ living on a lattice $\{\vec{r}_i\}_{i=1\ldots N}$.

In order to construct modes, corresponding to certain collective movements of these spins, it is helpful to think of this system as a discrete sampling of a continuous function $\hat{s}(\vec{r}) : \mathbb{R}^3 \to S^2$, where each discrete spin is just the value of this smooth function evaluated at a position of the lattice

$$\hat{s}_i = \hat{s}(\vec{r}_i)\ \forall i. \tag{3.105}$$

Now we will inspect small, spatially heterogenous, perturbations $\varepsilon\vec{v}(\vec{r})$ of this smooth function

$$\hat{s}\left(\vec{r} + \varepsilon\vec{v}(\vec{r})\right) \approx \hat{s}(\vec{r}) + \varepsilon \boldsymbol{J}(\vec{r})\vec{v}(\vec{r}) + \mathcal{O}(\varepsilon^2), \tag{3.106}$$

where $\boldsymbol{J}(\vec{r})$ is the Jacobian defined by

$$\boldsymbol{J}(\vec{r}) = \begin{pmatrix} [\nabla \hat{s}_x(\vec{r})]^T \\ [\nabla \hat{s}_y(\vec{r})]^T \\ [\nabla \hat{s}_z(\vec{r})]^T \end{pmatrix}. \tag{3.107}$$

We define the continuous mode $\vec{k}(\vec{r})$ as the coefficient of the contribution that is linear in ε, giving

$$\vec{k}(\vec{r}) = \boldsymbol{J}(\vec{r})\vec{v}(\vec{r}). \tag{3.108}$$

Sampling $\vec{k}(\vec{r})$ at the lattice points will give a discrete mode $\vec{k}_i$ in 3N space,

$$\vec{k}_i = \boldsymbol{J}_i\vec{v}(\vec{r}_i), \tag{3.109}$$

where the jacobians at the lattice points $\boldsymbol{J}_i$ have to be approximated by finite differences. Of course the discrete mode can then be freely normalized and projected into the tangential space.

The mode can be thought of as the generator of some transformation of the spin directions, which of course depends on the choice of $\vec{v}(\vec{r})$. The vector $\boldsymbol{v}(\boldsymbol{r})$ can be thought of as the description of the collective motion. *For example,* a translation in direction $\vec{t}$ can be generated by

$$\vec{v}(\vec{r}) = \vec{t}, \tag{3.110}$$

and a shrinking/growing transformation towards a center $\vec{c}$ can be generated by choosing

$$\vec{v}(\vec{r}) = \vec{r} - \vec{c}. \tag{3.111}$$

Generally speaking, it is possible to construct a plethora of different "modes" given an appropriate intuition for how to choose $\vec{k}(\vec{r})$.

Rotations

How these transformations relate to the energy of the system is a question of the spin directions $\hat{s}(\vec{r})$ and the Hamiltonian.

To properly consider spatial rotations, one needs to slightly extend Eq. (3.106) by also allowing the spins to rotate and the position coordinate to rotate. A rotation of $\hat{s}(\vec{r})$ by a rotation matrix $\boldsymbol{R}$ is defined as

$$\hat{s}(\vec{r}) \to \boldsymbol{R}^T \hat{s}(\boldsymbol{R}\vec{r}). \tag{3.112}$$

If we consider infinitesimal rotations of some vector $\vec{b}$ around an axis $\vec{a}$ by an angle ε we get

$$\boldsymbol{R}\vec{b} \approx \vec{b} + \varepsilon(\vec{a} \times \vec{b}). \tag{3.113}$$

Applying the infinitesimal rotation to Eq. (3.112) leads to

$$\begin{aligned}
\hat{s}(\vec{r}) &\to \boldsymbol{R}^T \hat{s}\left(\vec{r} + \varepsilon \vec{a} \times \vec{r}\right) && (3.114)\\
&\approx \boldsymbol{R}^T \left[\hat{s}(\vec{r}) + \varepsilon \boldsymbol{J}(\vec{r})(\vec{a} \times \vec{r})\right] && (3.115)\\
&\approx \hat{s}(\vec{r}) + \varepsilon \left[\boldsymbol{J}(\vec{r})(\vec{a} \times \vec{r}) - \vec{a} \times \hat{s}(\vec{r})\right] + \mathcal{O}(\varepsilon^2). && (3.116)
\end{aligned}$$

Thus, the continuous rotation can be approximated by

$$\vec{k}(\vec{r}) = \boldsymbol{J}(\vec{r})(\vec{a} \times \vec{r}) - \vec{a} \times \hat{s}(\vec{r}). \tag{3.117}$$

As explained before, this continuous approximation can be sampled at the lattice sites.

3.6.2 Zero-mode volume of a translation

From (3.104) it is straight forward to recover the approximation for the volume of a translational mode published by Bessarab *et al.* [129]. Consider that the approximate translational invariance implies that the norm of the difference between subsequent samples, $|\hat{s}_{i+1} - \hat{s}_i|$, does not depend much on the index i and, consequently, we can simplify the sum over the index i in Eq. (3.104). This allows us to write

$$Z_0 \approx \sum_{i=1}^{N} \left|\hat{s}^{(j+1)} - \hat{s}^{(j)}\right| \tag{3.118}$$

$$\approx N \left|\hat{s}^{(1)} - \hat{s}^{(0)}\right| \tag{3.119}$$

$$\approx \frac{L}{a} \left|\hat{s}^{(1)} - \hat{s}^{(0)}\right| \tag{3.120}$$

$$= \frac{L}{a} \left(\sum_j \left|\hat{s}(\vec{r}_j + \vec{a}) - \hat{s}(\vec{r}_j)\right|^2 \right)^{1/2}, \tag{3.121}$$

where L is the length of the periodic box in the direction of the zero-mode and a is the lattice constant of the system.

We can even go further an apply the cosine-model approximation. Since now we want to integrate over one period of the potential, it is necessary to revisit the upper limit of the integral in (3.101).

To integrate over one period of the potential, which for a translation corresponds to the lattice constant, we need to displace the spins by a vector $\vec{a}$, thus we define the volume of such a displacement as

$$V_a := \left|\hat{s}(\vec{r} + \vec{a}) - \hat{s}(\vec{r})\right|. \tag{3.122}$$

Due to Equation (3.102), the upper limit a in (3.101) simply becomes V_a and we can apply the cosine model by plugging $a = V_a$ into (3.95). Therefore, the total zeromode volume will be

$$Z_0 = \frac{L}{a} V_a \exp(-V_a^2 \kappa) \mathrm{I}_0(V_a^2 \kappa), \tag{3.123}$$

where

$$\kappa = \frac{\lambda}{4\pi^2 k_B T}, \tag{3.124}$$

and λ is the small (but finite) eigenvalue of the translational mode. Due to the transition behavior, displayed in Fig. 3.7 b), Equation (3.123) will interpolate between (3.121) and the value for the harmonic approximation.

The example of a small Skyrmion

In the following, we will discuss a small illustrative example of the mismatch between translational zero-modes at the saddle point and

at the minimum. The system is small Skyrmion in a square lattice with nearest-neighbor exchange ($J = 10\ \mathrm{meV}$) and Dzyaloshinski-Moriya interaction ($D = 6\ \mathrm{meV}$). Further, we assume an external magnetic field with strength $25\ \mathrm{T}$ and magnetic moments of $2\mu_B$. A GNEB calculation quickly gives the saddle point for the radial collapse to the ferromagnetic (+z) ground state of the system, with an energy barrier of $38.17\ \mathrm{meV}$.

The first fifty eigenvalues of the Hessian spectrum at the minimum and at the saddle point are shown in Fig. 3.8. While the translational modes at the minimum have an extremely small value, the translational modes at the saddle point, while still being small, have a significant value of $0.74\ \mathrm{meV}$.

Using (3.121), the translational mode volume at the saddle point can be computed. Its value is $V_a^{\mathrm{sp}} = 2.33$. According to (3.99), this means that these translational modes can be treated as harmonic modes if

$$T \lessapprox \frac{1}{2\pi k_B} V_a^2 \lambda \Leftrightarrow \ T \lessapprox 7.42\ \mathrm{K}. \tag{3.125}$$

The zeromode volume for one translation into an adjacent energy basin at the minimum is $V_a^{\mathrm{min}} = 3.64$. Hence, the total zero-mode volume, according to (3.121). Hence these modes must can be treated as zeromodes if $T > 2.6 \cdot 10^{-4}\ \mathrm{K}$, which is practically always the case.

For the fraction of zeromode volumes we can write

$$\frac{Z_0^{\mathrm{sp}}}{Z_0^{\mathrm{min}}} = \left[\frac{L}{a} V_a^{\mathrm{min}}\right] \left[\frac{L}{a} V_a^{\mathrm{sp}} \exp\left(-[V_a^{\mathrm{sp}}]^2 \kappa\right) \mathrm{I}_0\left([V_a^{\mathrm{sp}}]^2 \kappa\right)\right]^{-1} \tag{3.126}$$

$$\approx \frac{V_a^{\mathrm{min}}}{V^{\mathrm{sp,harm.}}} \text{ (if T < 7.42 K)} \tag{3.127}$$

As we can see, even for temperatures where the harmonic approximation is justified for the translational modes at the saddle point, we have to take the periodic nature of the lattice into account. If we had not done so, and had only computed the zero-mode volume at the minimum the factor $\frac{L}{a}$ in (3.127) would not have cancelled and the transition rate would have depended on the size of the periodic simulation box.

3.6.3 Zero-mode volume of a rotation

To find the zero-mode volume for a rotation, we make the same assumption as in the translational case, meaning $|\hat{s}_{i+1} - \hat{s}_i| = |\hat{s}_1 - \hat{s}_0|$. Then, since we know that the rotation has a period of 2π, we arrive at the zero-mode volume

$$Z_0 = 2\pi \left|\boldsymbol{J}(\vec{r})(\vec{a} \times \vec{r}) - \vec{a} \times \hat{s}(\vec{r})\right|. \tag{3.128}$$

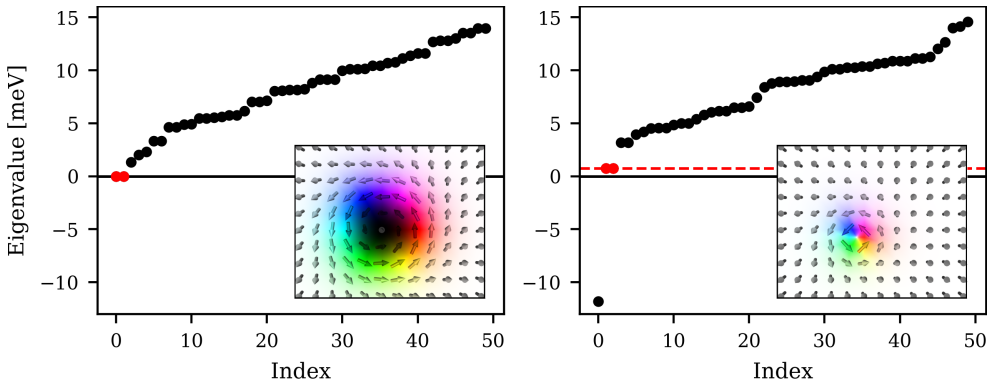


FIGURE 3.8

Spectrum of Hessian eigenvalues at the minimum (left) and at the saddle point (right) for a small Skyrmion in a square lattice. The translational eigenvalues are marked in red and the insets show the spin configuration at the respective point. For the minimum the translational modes have an extremely small eigenvalue of $1.08 \cdot 10^{-05}$ meV, while for the saddle point the translational modes have a small but finite value of 0.74 meV.

HOPFIONS IN MAGNETS 4

A *topological* magnetization soliton is a particle-like spin configuration that cannot be continuously deformed into the topologically trivial, collinear ground state [172]. By virtue of this impossibility, the collapse of topologically non-trivial spin configurations is associated with an energy barrier, making topology a useful indicator (not a criterion!) of thermal stability. One should, however, be aware that, strictly speaking, the definition of the soliton relies on a continuous field, while the spins live on a discrete lattice.

Magnetic Hopfions are such three-dimensional, topological solitons, characterised by the Hopf invariant, which can be described as the linking number of pre-images. In the exploration of their physical properties, an important goal is the search for true, stable Hopfions in bulk magnets. This is of special interest as there has been no experimental observation of Hopfions to date. Differently from the Skyrmion, the Hopfion is an inherently more complex, three-dimensional object and is comparatively less well studied. It is also by virtue of this additional dimension, that the treatment of Hopfions, both numerically and analytically, is more involved than for the Skyrmion.

A major hindrance for the use of Hopfions is the fact that physical systems with the ability to host them as meta-stable states seem to be very rare. At the time of writing and to the best of our knowledge, no experimental observations of isolated Hopfions in bulk magnetic systems have been made. So far, experimental evidence has been limited to "pseudo" Hopfions, relying on geometrical confinement [173–176] or stabilization by via additional structures like Hopfions on a skyrmion "string" [91]. Isolated Hopfions in bulk solids have not been observed yet.

On the theoretical side, different systems – i.e. different energy functionals – have been researched. The Skyrme-Faddeev model [177] proved to be especially productive and quite an impressive zoology of Hopfions could be identified numerically [178].

The physical laws governing the behavior of chiral magnets, which are interesting candidates for spintronics applications, are unfortunately not described by the Skyrme-Faddeev model, and there the search for Hopfions typically begins with studying effective model

Hamiltonians. Most of the current literature uses the framework of micromagnetics, where the discrete spin configuration is approximated via a continuous spin density. Theoretical considerations show that the typical micromagnetic Heisenberg Hamiltonian with only an exchange interaction does not allow for stable (static) soliton solutions, due to the Derrick theorem [179]. If the Heisenberg-Hamiltonian is extended to also include the Dzyaloshinski-Moriya interaction (DMI) [180], occurring in non-centro symmetric crystals, this theorem does not forbid the existence of Hopfion solutions [181]. These systems, called chiral magnets, are also where the well-studied Skyrmions are found.

At strengths of the DMI, thought to be necessary to stabilize Hopfions, the collinear background state is not energetically favorable and would therefore collapse to spin-spiral or cone phases, which may lead to non-trivial consequences regarding the topological definition of the Hopf invariant [79]. If a collinear (ferromagnetic) ground state is required, numerical simulations in chiral magnets can only produce Hopfions in confined geometries. In these confined geometries the finite system size prevents the Hopfion from expanding to infinity, and the inclusion of additional pinning layers stabilizes the collinear state [76, 83, 84]. Arguably, such Hopfions are of limited use for spintronic applications, due to the loss of many of the desirable particle-like properties, like their mobility.

Of further interest are higher order spin-interaction terms, for which effective model parameters, extending the atomistic Heisenberg Hamiltonian, can be derived from density functional theory (DFT) [182]. For example, multi-site-multi-spin interactions such as the biquadratic exchange or the four-spin interaction translate in the continuum limit to higher-order gradients of the magnetization field and thus to Hopfion stabilizer. In this context the discovery of the spin interaction due to the topological orbital moments generated by the scalar spin-chirality [90] is very interesting as it was found that this interaction combined with the Heisenberg model converges to the Faddeev model, which is known to host Hopfions.

Fortunately, there remains another promising avenue towards stable, unconfined Hopfions in bulk material. Numerical studies predict the stability of Hopfions in frustrated magnets – i.e. magnets with competing exchange interactions. In Refs. [74, 77] stable Hopfions could be predicted by extending the micromagnetic exchange energy density with terms accounting for anti-ferro magnetic coupling to next-nearest neighbors.

Using (amongst others) atomistic spin simulations, Rybakov *et al.* [74], have shown that Hopfions can be stabilized in a classical Heisenberg model of bulk magnets with frustrated exchange interactions. Further, they give a stability criterion derived from an extended micromagnetic energy functional. The rest of this chapter will focus on

Hopfions in the model of Rybakov *et al.* [74], which, in the following, is called the RKBDMB-model.[1]

4.1 The RKBDMB-model

In this section[2], we will summarize the RKBDMB-model, describing magnetization textures in terms of the unit vector field $\hat{s}(\vec{r})$, with $|\hat{s}(\vec{r})| = 1$, in cubic bulk magnets with frustrated exchange interactions and negligible magnetic anisotropy by the energy functional

$$E = \int_{\mathbb{R}^3} \left[\mathcal{A} \sum_{\alpha} \left(\frac{\partial \hat{s}}{\partial r_\alpha} \right)^2 + \mathcal{B} \sum_{\alpha,\beta\neq\alpha} \left(\frac{\partial^2 \hat{s}}{\partial r_\alpha^2} - \frac{\partial^2 \hat{s}}{\partial r_\beta^2} \right)^2 + \mathcal{C} \sum_{\alpha,\beta\neq\alpha} \left(\frac{\partial^2 \hat{s}}{\partial r_\alpha \partial r_\beta} \right)^2 \right] \mathrm{d}^3\vec{r}, \tag{4.1}$$

where $\alpha, \beta \in \{x, y, z\}$, $\mathcal{A}$ is the spin-stiffness, and $\mathcal{B}$, $\mathcal{C}$ are exchange constants beyond the micromagnetic standard model.

As described by Sallermann *et al.* [81], one can employ a reduced unit system to simplify the analysis. These reduced units are defined by the substitutions

$$\vec{r} \to \vec{x} = \vec{r}/r_0 \quad \text{with} \quad r_0 = \sqrt{\frac{\mathcal{B}+\mathcal{C}}{\mathcal{A}}} \tag{4.2}$$

and

$$E \to \mathcal{E} = E/E_0 \quad \text{with} \quad E_0 = \mathcal{A} r_0. \tag{4.3}$$

The energy functional (4.1) is, thus, transformed into

$$\mathcal{E} = \int_{\mathbb{R}^3} \left[\sum_{\alpha} \left(\frac{\partial \hat{s}}{\partial x_\alpha} \right)^2 + (1-\gamma) \sum_{\alpha,\beta\neq\alpha} \left(\frac{\partial^2 \hat{s}}{\partial x_\alpha^2} - \frac{\partial^2 \hat{s}}{\partial x_\beta^2} \right)^2 + \gamma \sum_{\alpha,\beta\neq\alpha} \left(\frac{\partial^2 \hat{s}}{\partial x_\alpha \partial x_\beta} \right)^2 \right] \mathrm{d}^3\vec{r}, \tag{4.4}$$

with one dimensionless parameter

$$\gamma = \frac{\mathcal{C}}{\mathcal{B}+\mathcal{C}}. \tag{4.5}$$

[1] The acronym RKBDMB-model was used by Sallermann *et al.* [81] and is derived from the initials of the last names of all co-authors of Ref. [74] (Rybakov, Kiselev, Borisov, Döring, Melcher and Blügel). The usefulness of this abbreviation remains an open question.

[2] Please note that this section has been adapted from Sallermann *et al.* [81].

If the constant coefficients are greater than zero ($\mathcal{A}, \mathcal{B}, \mathcal{C} \geq 0$), the energy density is always non-negative [due to the powers of two in (4.1)]. An energy of exactly zero is obtained if all derivatives vanish, and consequentially the ground state is ferromagnetic if $\mathcal{A}, \mathcal{B}, \mathcal{C} \geq 0$. In this case, the parameter γ only takes values within the interval $[0, 1]$. It is evident that $\gamma = 0$ corresponds to $\mathcal{C} = 0$, while $\gamma = 1$ corresponds to $\mathcal{B} = 0$. As shown in Ref. [81], γ can be interpreted as an anisotropy parameter that controls the symmetry of locally optimal spin configurations, ranging from (amongst others) toroidal Hopfions with hexagonal symmetry at $\gamma = 0$ to the fully isotropic case attained at $\gamma = 6/7$ when $\mathcal{C} = 6\mathcal{B}$, to a quadratic symmetry at $\gamma = 1$. The parameter r_0 is a characteristic length scale that isotropically scales the size of these configurations without changing the symmetry.

According to the approximate criterion, derived by Rybakov *et al.* [74], Hopfions are likely to be local energy minima of discrete realizations of the energy functional (4.4), if the condition

$$\max\Big(\gamma, 6(1-\gamma)\Big) \gtrapprox 6.5 \left(\frac{d}{r_0}\right)^2 \tag{4.6}$$

holds, where d is the distance between nearest neighbor spins. In the case of the simple cubic lattice, d equals the lattice constant a.

As shown by Rybakov *et al.* [74], the RKBDMB-model is the long-wavelength limit of a minimal effective isotropic Heisenberg Hamiltonian [for a more general form of the Heisenberg Hamiltonian see Eq. (1.16)]

$$\mathcal{H} = -\sum_{s=1}^{4} J_s \sum_{\langle i,j \rangle_s} \hat{s}_i \cdot \hat{s}_j, \tag{4.7}$$

a spin-lattice model considering the magnetic interaction between atoms up to four atomic shells s of nearest neighbor atoms.[3] If the expansion of the Heisenberg model is truncated at the fourth power in the angular change of the magnetic moments between neighbors, the micromagnetic parameters ($\mathcal{A}, \mathcal{B}$ and $\mathcal{C}$) and the Heisenberg exchange couplings J_s are related by linear maps $\mathcal{A}\{\mathcal{B}, \mathcal{C}\} = \sum_s a_s\{b_s, c_s\}J_s$. The coefficients in the linear maps depend on the underlying atomic lattice, for some lattices these values are tabulated in Ref. [74]. The coefficients for the purpose of this thesis can be found by following the instructions in the Appendix of Ref. [81].

[3] Of course, more than four shells can be considered as well.

4.2 Energy barriers of Hopfions in the RKBDMB-model

For the sake of completeness, this section briefly summarizes the results by Sallermann *et al.* [81].[4]

Sallermann *et al.* [81] investigated energy barriers for the decay of toroidal Hopfions, with unity Hopf charge, to the ferromagnetic ground state for a range of symmetry parameters γ and characteristic length scales r_0.

An overview of the tested parameters as well as the obtained Hopfions is shown in Fig. 4.1. For all the tested parameters, the decay mechanism was the collapse of the central hole of the toroid (and the formation of two Bloch points), followed by a gradual shrinking of the outer structure. For examples of how these saddle points look, for a few selected parameters, refer to Fig. 4.2. The energy barriers obtained in Ref. [81], are plotted in Fig. 4.3.

4.3 Lifetimes of Hopfions in the RKBDMB-model

As clearly evidenced by Fig. 4.3, the energy barriers can reach significant values. However, it is also clear that the energy barrier is not the sole determining factor for thermal decay rates and, therefore, a computation of the pre-exponential factor in the spirit of Chapter 3 is desirable. To that end (simultaneously with the work on energy barriers in Ref. [81]), the pre-exponential pre-factor was computed by Lobanov & Uzdin [127] (also working in the RKBDMB-model but at a fixed r_0 of $2.1\ a$). The results by Lobanov *et. al.*, pointed at an extraordinarily large rate constant ($\sim 10^{19}$ ps), due to the relatively high entropy of the saddle point compared to the Hopfion.

In this section, we shall conduct further investigation of the pre-exponential factor of Hopfions in the RKBDMB-model. The study, conducted here, differs from the work of Lobanov *et. al.* in the following ways:

1. *Different parameters.* The Hamiltonian is the same as (4.7) and we investigate isotropic Hopfions ($\gamma = 6/7$) at a fixed characteristic energy E_0, but increase the characteristic length scale r_0. The parameters are summarized in Table 4.1. They are a subset of the parameters investigated for the energy barriers in Ref. [81].

[4] Please note that this section has been adapted from Sallermann *et al.* [81].

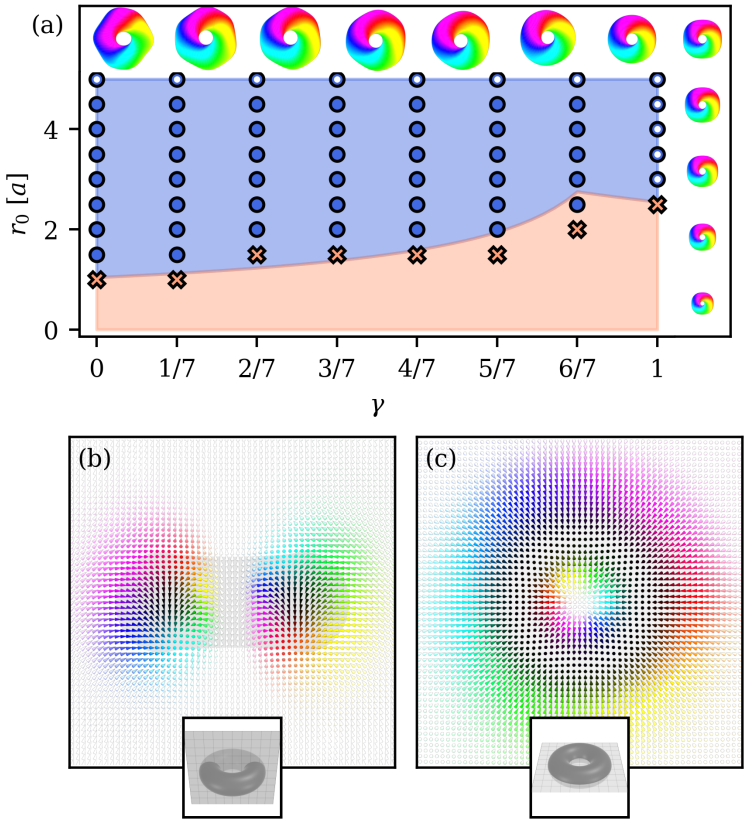


FIGURE 4.1

(a) The investigated parameter space (γ, r_0). The characteristic energy E_0 has been kept constant at 1 meV, while γ has been varied in steps of $1/7$ and r_0 in steps of $0.5\ a$, where a is the lattice constant of the simple cubic atomic lattice. The markers show the discrete pairs of (γ, r_0) for which the energy barrier was investigated. A blue circle signifies a stabilized Hopfion and a red cross signifies a point where a Hopfion could not be stabilized and the system decayed into the ferromagnetic ground state. The blue (red) shaded background illustrates the region where the criterion Eq. (4.6), which is derived from micromagnetic models, predicts Hopfion stability (instability). The images of the magnetization textures at the top and right side show $n_z = 0$ isosurfaces of the magnetization texture, for different values of γ and r_0. The color tone of the surface depends on the azimuthal angle of the spin direction, additionally a detailed depiction of the color code can be found in Appendix A.2. Small white dots on top of the blue circles mark (γ, r_0)-points for which isosurfaces are shown. (b) Cross section of the isotropic (γ, r_0) = ($6/7$, $5\ a$) Hopfion in a plane containing the central normal of the toroid. The bottom inset illustrates the cross section plane in relation to the $\hat{s}_z = 0$ isosurface. (c) Cross section of the same Hopfion in the equatorial plane of the toroid. Again, the bottom inset illustrates the cross section plane in relation to the $\hat{s}_z = 0$ isosurface. Reprinted with permission from Sallermann *et al.* [81].

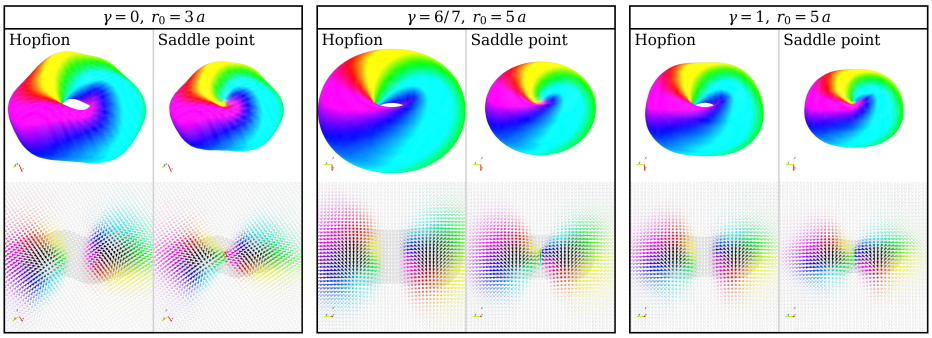


FIGURE 4.2
Hopfions and saddle points for the collapse of small toroidal unit charge Hopfions to the ferromagnetic ground state in the RKBDMB model for a few selected parameters. For each set of parameters (γ, r_0), a panel of four images is shown. The Hopfion (a local energy minimum) is shown on the left column and the saddle point is shown on the right column. The top row shows renderings of the $(\hat{s}_z = 0)$-isosurface, colored according to the orientation of the spin in the xy-plane. The bottom row shows cross sections of the same structure through the toroidal normal. Reprinted with permission from Sallermann *et al.* [81].

2. *Treatment of zeromodes.* While in Ref. [127] the boundary spins were pinned to remove zeromodes, the zeromode contribution is treated with the techniques developed and described in Chapter 3.

4.3.1 Zeromode analysis

For the zeromode analysis, we compute the Hessian modes with the smallest eigenvalues, using a partial diagonalization of the Hessian matrix $\boldsymbol{H}$.

As an example, the spectra at the local minimum and at the saddle point for the Hopfion with $r_0 = 3\ a$ (System II in Tab. 4.1) are shown in Figure 4.4.

At the minimum, six modes with extremely small eigenvalues (smaller than 10^{-10} meV) are present. Further there exist two intermediate modes with small eigenvalues of $1.5 \cdot 10^{-5}$ meV. Finally a continuous spectrum of modes emerges at around $1.5 \cdot 10^{-3}$ meV. For the other parameter sets in Tab. 4.1, the same number of and types of zeromodes are found.

At the saddle point, on the other hand, only three modes with a clear gap to the rest of the spectrum are present. This hints at the fact that the saddle point is more localized due to the discretization effect of the crystal lattice. As we have seen before, it is crucial to correctly treat the zeromode volumes at the minimum and at the saddle point

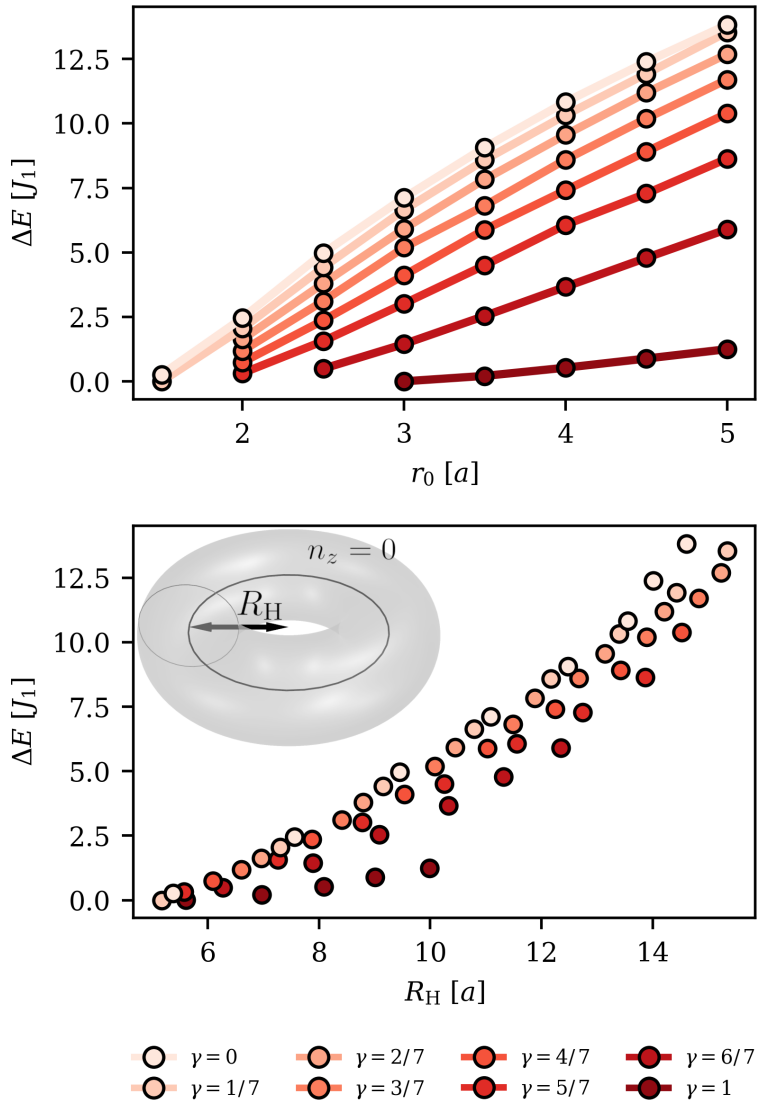


FIGURE 4.3
Energy barriers for the collapse of small toroidal unit charge Hopfions to the ferromagnetic ground state in the RKBDMB model. For both plots (top and bottom), the energy barrier (in units of the exchange constant of the first shell) is shown on the y-axis. The top plot puts the characteristic length scale on the x-axis, while the bottom plot instead uses an ad-hoc definition of the Hopfion radius (illustrated in the inset) on the x-axis, to correct for the tendency of the symmetry parameter γ to also change the size of the Hopfion. Reprinted with permission from Sallermann *et al.* [81].

Name	J_1 [meV]	J_2 [meV]	J_3 [meV]	J_4 [meV]	γ []	r_0 []	ΔE [meV]	N_{spin} []
I	10.0	-2.009	0.290	-0.730	$6/7$	2.5	4.32	48^3
II	10.0	-1.460	-0.127	-0.871	$6/7$	3.0	13.46	48^3
III	10.0	-0.905	-0.548	-1.012	$6/7$	3.5	24.01	48^3
IV	10.0	-0.345	-0.970	-1.153	$6/7$	4.0	35.33	48^3
V	10.0	0.217	-1.395	-1.295	$6/7$	4.5	47.00	48^3
VI	10.0	0.781	-1.819	-1.437	$6/7$	5.0	58.78	48^3

TABLE 4.1
Parameters for the lifetime calculations of Hopfions in frustrated exchange magnets. The J_i parameter is the strength of symmetric exchange interactions with the i-th neighbor shell in the simple cubic lattice. The characteristic length r_0 and symmetry parameter γ are computed from Eqs. (4.2) and (4.5).

in order to not incur any unphysical scaling with the system size.

For a summary of the zeromode analysis at the minima (the Hopfions) and at the saddle points refer to Tables 4.2 and 4.3 respectively.

Collective spin rotations

Since the Hamiltonian (4.7) contains only exchange interactions, the energy is perfectly invariant[5] under collective rotations of all spins around the same axis and by the same angle (this means the pairwise angle between spins does not change). Such modes are trivial to construct by following the steps in Section 3.6. The modes are found by setting

$$\vec{k}_i = \vec{a} \times \hat{s}_i, \tag{4.8}$$

in Eq. (3.100), where $\vec{a}$ is the axis of rotation. The corresponding mode volume is

$$Z_0 = 2\pi \left| \vec{a} \times \hat{s}_i \right|. \tag{4.9}$$

Since these are true zeromodes,[6] the considerations in Section 3.5.1 do not apply. At a first glance, it might seem like the collective spin rotations could account for three zeromodes (one for each spatial axis), this is however *not* the case since only two linearly independent $3N$-dimensional vectors $\boldsymbol{k}$ can be constructed from Eq. (4.8). Intuitively,

[5] In this case the eigenvalues for the collective spin rotation modes should truly be equal to zero and not, like it is usually the case with e.g. translations, just close to zero. However, due to finite precision in the partial diagonalization algorithm the numerical result does not quite achieve this.

[6] True in the sense that the eigenvalue should indeed be exactly equal to zero and not just a very small, but finite, number like it is the case for translations and spatial rotations. However, in the partial diagonalization eigenvalues of exactly zero are not quite achieved due to numerical inaccuracies.

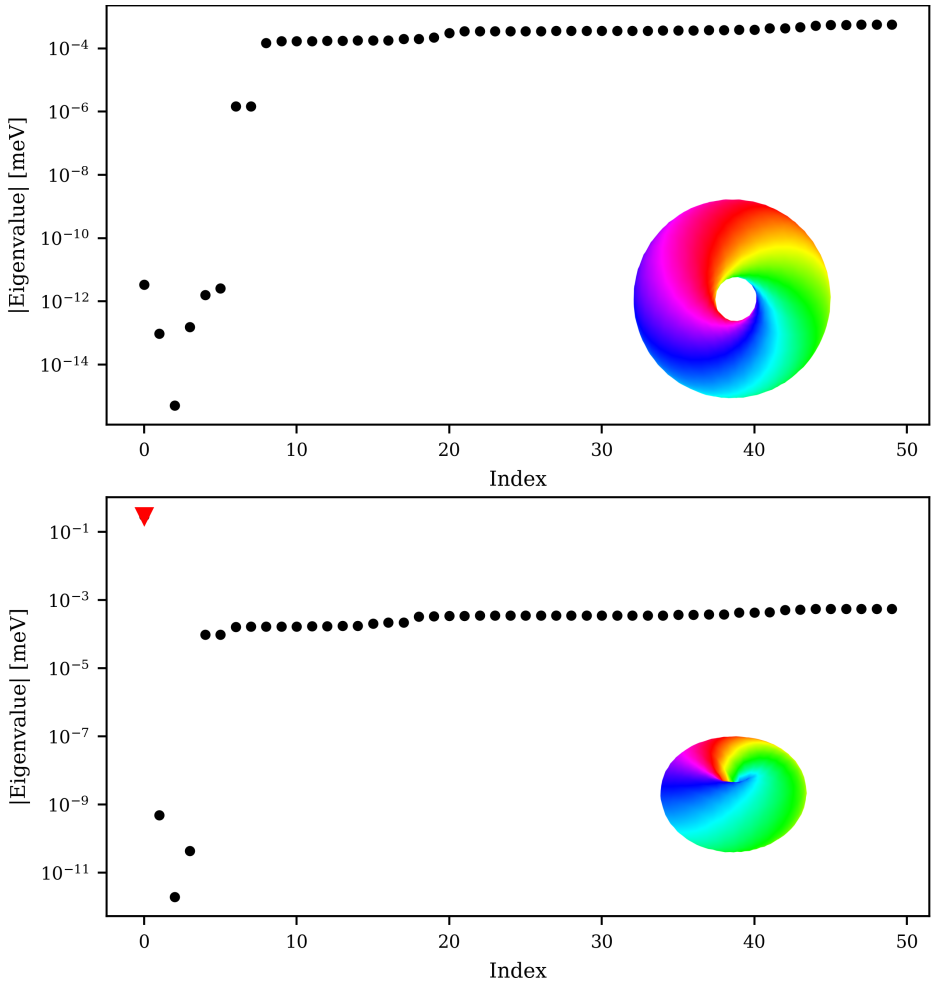


FIGURE 4.4
Spectra of the Hopfion with $r_0 = 3\ a$ at the minimum (top) and at the saddle point (bottom). Due to the use of the log-scale on the y-axis, the absolute value of the eigenvalues is shown, the x-axis shows the index of the eigenvalue in increasing order. The negative eigenvalue at the saddle point is marked with a red downwards pointing triangle. The insets show renderings of the $\hat{s}_z = 0$ isosurface.

this is quite easy to see from the fact that the tangent space of each spin has only two degrees of freedom.

At both stationary points, the minimum and the saddle point, two collective spin rotation modes are present.

Translations

As expected in a bulk system, three translational modes can be observed at the Hopfion. They are constructed from Eq. (3.100) by using

$$\vec{k}_i = \boldsymbol{J}_i \vec{t} \text{ with } \vec{t} \in \{\hat{e}_x, \hat{e}_y, \hat{e}_z\}, \tag{4.10}$$

where $\boldsymbol{J}_i$ is the Jacobian of the spin structure at the lattice site i.

At the saddle point, the eigenvalue of the translational modes is high enough for them to be absorbed into the rest of the spectrum. Nonetheless, they enter the calculation by cancelling the scaling with the size of the simulation box, which stems from the zeromode volume of the translations of the minimum.

Spatial rotation around normal

Another zero-mode is the spatial rotation around the normal of the Hopfion toroid (the normal is also indicated in the illustration Fig. 1.1).

This mode can be constructed from (3.117), if one only takes the contribution that depends on the Jacobian. Effectively, the constructed mode is a linear combination of a collective spin rotation and a "proper" spatial rotation. This "hybridisation" occurs since the eigenvectors of the Hessian are pairwise orthogonal and the collective spin rotation is already a separate eigenmode.

Intuitively, since the Hopfion normal is not aligned with the background spins, which point in the $\hat{e}_z$ direction, the collective spin rotation simply counteracts the contribution in (3.117) that would rotate the background spins.

At the saddle point, the same rotation around the normal occurs as well.

Spatial rotations orthogonal to normal

The two intermediate modes at the minimum, with an eigenvalue of around $1.5 \cdot 10^{-5}$ meV (see Fig. 4.4) are spatial rotations around an axis orthogonal to the Hopfion normal.

At the saddle point, similarly to the minimum, spatial rotations around the axes orthogonal to the normal also exist at intermediate eigenvalues – although, here, the gap to the rest of the continuous part of the spectrum is reduced, compared to the situation at the minimum.

Given the large spectral gap of the first six modes to the rest of the continuous spectrum at the minimum, it should be obvious that these modes must be treated as true zero-modes. The intermediate spatial rotations around axes orthogonal to the Hopfion normal, however, might have to be treated as zeromodes or harmonic modes depending on the temperature. Using the criterion for harmonic modes (3.99), which we derived earlier, and the mode lengths of these rotations, we can estimate the temperatures up to which, these modes should be treated as harmonic. Given the simple cubic lattice, it is natural to assume that the discretization of the lattice occurs at angles of $\frac{\pi}{4}$, hence the length of the mode should be multiplied by that number.

Overall, this means that these modes should be treated as harmonic, only if $T < 2.1 \cdot 10^{-1}$ K. Of course, it is also possible to use the cosine model (3.95) to approximate the zeromode contribution for all temperature ranges.

Verification of constructed zeromodes

Due to the finite numerical precision of the partial diagonalization and the potential mode hybridization, it can be difficult to find the mapping between constructed modes and the computed eigenvectors of the Hessian. Therefore, it is useful to perform a verification by comparing how closely the space of constructed linear modes approximates the linear subspace of near-zero-eigenvalue Hessian eigenvectors. In order to make such a comparison, we compute the geodesic distance between the two subspaces on the Grassmann manifold.

For the comparison, we construct two points on the Grassmann manifold $G_{m,2N_{\text{spin}}}$,[7] where m is the number of zeromodes.

The points on the manifold can be represented by tall matrices with columns formed by the respective vectors. We thus construct the point

$$\boldsymbol{K} = \Big(\boldsymbol{k}_1, ..., \boldsymbol{k}_m\Big) \in \mathbb{R}^{2N_{\text{spin}},m}, \tag{4.11}$$

where $\boldsymbol{k}_i$ denotes the constructed modes (after projection into the tangent space of the spin manifold) and the point

$$\boldsymbol{V} = \Big(\boldsymbol{v}_1, ..., \boldsymbol{v}_m\Big) \in \mathbb{R}^{2N_{\text{spin}},m}, \tag{4.12}$$

where $\boldsymbol{v}_i$ denotes the computed eigenvectors of the Hessian.

Then we compute the geodesic distance between $\boldsymbol{K}$ and $\boldsymbol{V}$ as

$$d(\boldsymbol{K}, \boldsymbol{V}) = \sqrt{\sum_{i=1}^{m} \arccos^2 s_i}, \tag{4.13}$$

[7] The Grassmann manifold is the manifold of k-dimensional linear subspaces of $\mathbb{R}^n$

TABLE 4.2
Volumes of zeromodes at the local minimum, as well as the achieved quality factors q, computed from Eq. (4.14). The parameters, in each column, correspond to the ones shown in Tab. 4.1.

r_0 $[a]$	2.50	3.00	3.50	4.00	4.50	5.00
Transl. $\hat{e}_x$	17.03	19.14	20.89	22.42	23.76	24.89
Transl. $\hat{e}_y$	17.03	19.14	20.89	22.42	23.76	24.89
Transl. $\hat{e}_z$	17.03	19.14	20.89	22.42	23.76	24.89
Rot. (normal)	82.92	107.13	132.65	161.01	195.65	219.10
Spin rot. ($\hat{e}_x$)	246.49	242.64	238.51	233.74	228.70	224.88
Spin rot. ($\hat{e}_y$)	246.51	242.75	238.32	233.75	229.07	224.64
Rot. (orth. norm.)	79.11	108.75	140.46	174.23	212.88	243.79
Rot. (orth. norm.)	79.60	108.90	140.00	174.31	214.17	242.00
q	0.13	0.15	0.18	0.21	0.24	0.25

TABLE 4.3
Volumes of zeromodes at the saddle points, as well as the achieved quality factors q, computed from Eq. (4.14). The parameters, in each column, correspond to the ones shown in Tab. 4.1

r_0 $[a]$	2.50	3.00	3.50	4.00	4.50	5.00
Spin rot. ($\hat{e}_x$)	248.71	246.95	245.25	240.71	241.71	240.21
Spin rot. ($\hat{e}_y$)	248.71	247.09	244.95	242.68	241.72	240.21
Rot. (normal)	68.30	83.23	95.70	115.83	120.09	130.16
q	0.17	0.21	0.22	0.27	0.27	0.28

where s_i are the singular values of $\boldsymbol{K}^T\boldsymbol{V}$.

Finally, we use the maximum geodesic distance between any pair of points, which is $d_{\text{max}} = \frac{\pi}{2}\sqrt{m}$, to define the dimensionless "quality" of the zeromode construction

$$q = \frac{d(\boldsymbol{K}, \boldsymbol{V})}{d_{\text{max}}} = \frac{2d(\boldsymbol{K}, \boldsymbol{V})}{\pi\sqrt{m}} \in [0, 1], \tag{4.14}$$

where $q = 0$ indicates a perfect match and $q = 1$ a perfectly orthogonal subspace. The advantage of using Eq. (4.14) is that it is not sensitive to effects like mode hybridization and finding, for instance, the *exact* direction of translational modes or the axes of collective spin rotations.

The volumes of the zeromodes, as well as the achieved qualities q for the local minimum (the Hopfion) and the saddle points, are tabulated in Tables 4.2 and 4.3 respectively.

4.3.2 Determinant computation

Following the discussion in Sec. 3.4.2, the determinants at the saddle points and at the minima, were computed from a sparse LU decomposition with diagonal shifting.

To confirm that the shift parameters were large enough it was ensured that, in the region of the fit, the inequality

$$\frac{\partial}{\partial \log \alpha} \log \det(\boldsymbol{H} + \alpha \boldsymbol{I}) > n_{\text{zero}} \tag{4.15}$$

was fulfilled, where n_{zero} is the expected number of zeromodes (six for the Hopfions and three for the saddle points) $\boldsymbol{H}$ is the hessian matrix, α is the diagonal shift parameter and $\boldsymbol{I}$ a diagonal matrix of the same shape as the Hessian. For an example of Eq. (4.15), applied to a Hopfion and to a saddle point, refer to Fig. 4.5a and Fig. 4.6a, respectively.

Then, the second order polynomial, with positive coefficients,

$$a + \alpha b - \frac{1}{2}\alpha^2 c \text{ with } a, b, c > 0 \tag{4.16}$$

was fitted to the shifted positive definite log-determinants[8]. The value of the true (non-shifted) positive-definite (PD log-determinant is then immediately available as the offset a in (4.16).

The results of this procedure, for a minimum and for a saddle points, are shown in Fig. 4.5b and Fig. 4.6b, respectively. These figures also underline the need for diagonal shifting: For very small shifts, in the range of $\alpha < 10^{-9}$, the obtained PD-determinants fluctuate by up to six orders of magnitude and are essentially unusable, the diagonal shifting technique allows us to extract a much more accurate determinant. This happens due to the extremely high *relative* error of the near-zero eigenvalues in the partial diagonalization.

Comparison to previous calculations

Lobanov & Uzdin [127] have calculated lifetimes for Hopfions with competing exchange interactions in a simulation box, which contained $60 \times 60 \times 60$ spins. The exchange interaction parameters used can be found in Table. 4.4.

Fig. 4.7 displays the contribution of the determinants to the entropy factor as computed in this work, as well as three parameter

[8] Positive definite determinant, here, means that the result of the sparse LU decomposition was divided by the shift parameter raised to the power of the number of zeromodes. At the level of the log-determinant this leads to $\log \det^{+}(\boldsymbol{H} + \alpha \boldsymbol{I}) \approx \log \det(\boldsymbol{H} + \alpha \boldsymbol{I}) - n_{\text{zero}} \log \alpha$. The negative eigenvalue at the saddle point is removed as well, of course.

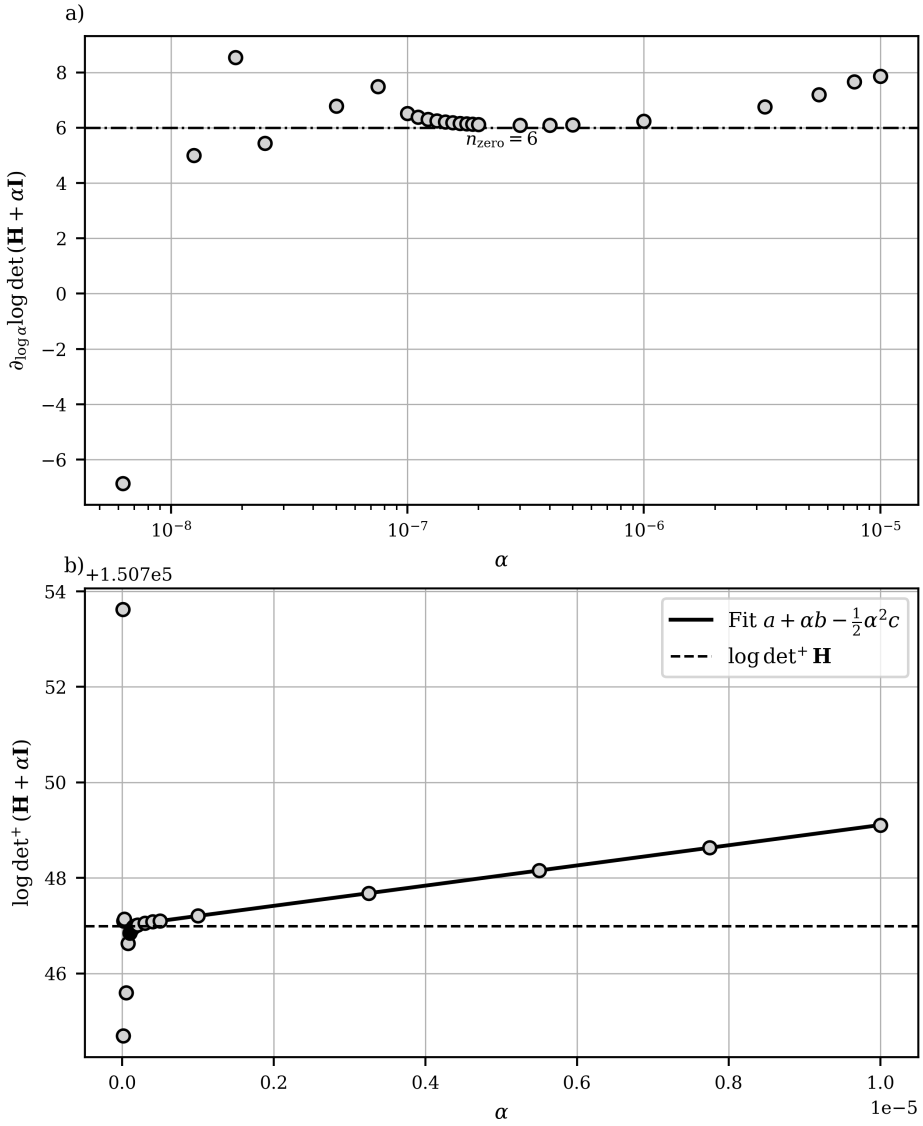


FIGURE 4.5

Result of diagonally shifted determinants of the Hessian for the RKBDMB Hopfion model at the minimum, for $r_0 = 4.5\ a$. **a)** The derivative of the log-determinants with respect to the logarithm of α. This derivative is expected to match the number of eigenvalues with $\lambda_i \ll \alpha$ and, therefore, the number of zeromodes. The expected number of zeromodes (six for a minimum) is drawn as a red horizontal line and we see a good match towards the right hand side of the plot. **b)** The logarithm of the shifted positive-definite determinants $\log\det^+(\boldsymbol{H} + \alpha\boldsymbol{I})$, at the right-hand side of the plot (for $\alpha > 2 \cdot 10^{-7}$) a second order polynomial was fitted (solid black line) and extrapolated to $\alpha = 0$ in order to find the value of $\log\det^+(\boldsymbol{H})$ (dashed black line). The coefficients of the polynomial provide approximations for the trace of the inverse of the positive definite part of the Hessian and the trace of the squared inverse of the positive definite part of the Hessian.

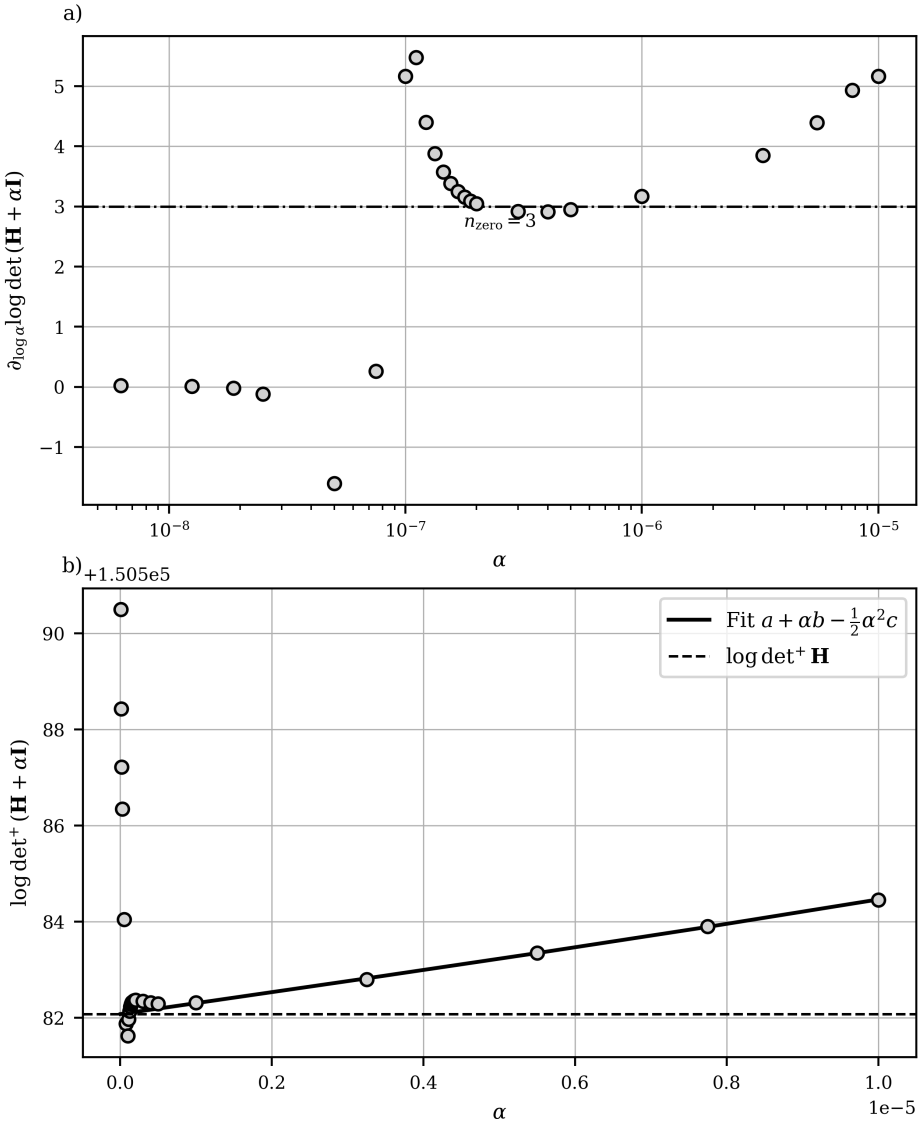


FIGURE 4.6

Result of diagonally shifted determinants at the saddle point, for $l_0 = 4.5\ a$. **a)** The derivative of the log-determinants with respect to the logarithm of α. This derivative is expected to match the number of eigenvalues with $\lambda_i \ll \alpha$ and, therefore, the number of zeromodes. The expected number of zeromodes (three for a saddle point) is drawn as a red horizontal line and we see a good match towards the right hand side of the plot. **b)** The logarithm of the shifted PD-determinants $\log\det^+(\boldsymbol{H}+\alpha\boldsymbol{I})$, at the right-hand side of the plot (for $\alpha > 2 \cdot 10^{-7}$) a second order polynomial was fitted (solid black line) and extrapolated to $\alpha = 0$ in order to find the value of $\log\det^+(\boldsymbol{H})$ (dashed black line). The coefficients of the polynomial provide approximations for the trace of the inverse of the positive definite part of the Hessian and the trace of the squared inverse of the positive definite part of the Hessian.

Name	J_1	J_2	J_3	J_4
Lobanov-I [127]	1	0	0	-0.24
Lobanov-II [127]	0.5	0.25	-0.125	-0.24
Lobanov-III [127]	2	-0.5	0.25	-0.24

TABLE 4.4
Parameters of Hopfions for lifetime calculation in arbitrary units of J_0. The first three rows correspond to the parameter set, studied by Lobanov & Uzdin [127]. All of these parameters correspond to the same micromagnetic units $a\mathcal{A} = 2.1$, $\mathcal{B}/a = 0.02958(3)$ and $\mathcal{C}/a = 2\mathcal{B}$

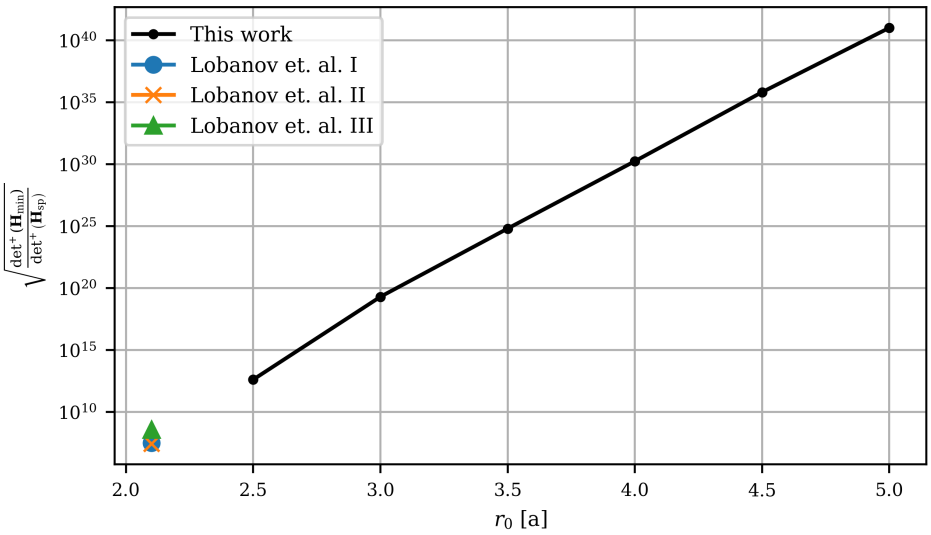


FIGURE 4.7
Determinant contribution to the rate pre-factor. Black dots and line show the contributions found in this work, while the colored markers denote the results by Lobanov & Uzdin [127].

sets (all corresponding to the same characteristic length) investigated by Lobanov & Uzdin [127] – showing good agreement. It is, further, evident that increasing the characteristic length scale r_0 leads to a rapid increase of the rate pre-factor, counteracting the concurrent increase in the decay energy barriers (shown in Fig. 4.3). Similar relationships between pre-exponential factors and energy barriers have been observed often enough, albeit in different fields and contexts, to be given the name *law of compensation* or Meyer-Neldel rule [183, 184].

4.3.3 Lifetimes

By now, we have seen that increasing the characteristic length scale r_0 of (4.4), leads to two counteracting effects: (1) an increase in the decay energy barriers (favouring longer lifetimes) and (2) an increase in the determinant contribution to the rate pre-factor (favouring shorter lifetimes). Which of these two contributions dominates and decides if the lifetime of a Hopfion ultimately increases or decreases with an increase in the size r_0 is, of course, also a question of the temperature.

In order to gain more insight into this problem, the lifetimes were obtained from harmonic transition state theory *without* taking thermal crossings into account, which means that only the $k_B T \boldsymbol{a}^T \boldsymbol{H}^{-1} \boldsymbol{a}$ contribution [evaluated from Eq. (3.48)] entered into the variance of the perpendicular velocity. For the entropic contribution, Eq. (3.13) was used with $N_0^{\mathrm{M}} = 6$ and $N_0^{\mathrm{SP}} = 3$.

In agreement with the earlier discussion, we can indeed observe a law of compensation. See for example, Fig. 4.8, where at $T = 5\ \mathrm{K}$ (top plot), the lifetime does increase with increasing r_0, but for $T = 10\ \mathrm{K}$ (bottom plot) it flattens out. The reason is, of course, that the slope (in a log-plot) of the pre-factor is not temperature dependent and tends to decrease the lifetime, while the slope for the energy barrier contribution scales inversely with the lifetime and can therefore only counter the pre-factor slope at low temperatures.

An overview of all the found lifetimes is provided by Fig. 4.9, which displays the obtained Hopfion lifetimes against the temperature and the characteristic length scale r_0. For low temperatures (around $4\ \mathrm{K}$) and relatively large Hopfions $r_0 > 4\ a$, significant lifetimes of around one year are predicted. It is thus possible that Hopfions could indeed be observed at very low temperatures ($4.2\ \mathrm{K}$ matches the boiling point of liquid Helium and is a temperature achievable in cryostats). Considering the significant number of approximations made at all levels of these calculations, it would be unwise to consider these results as anything but indicative.

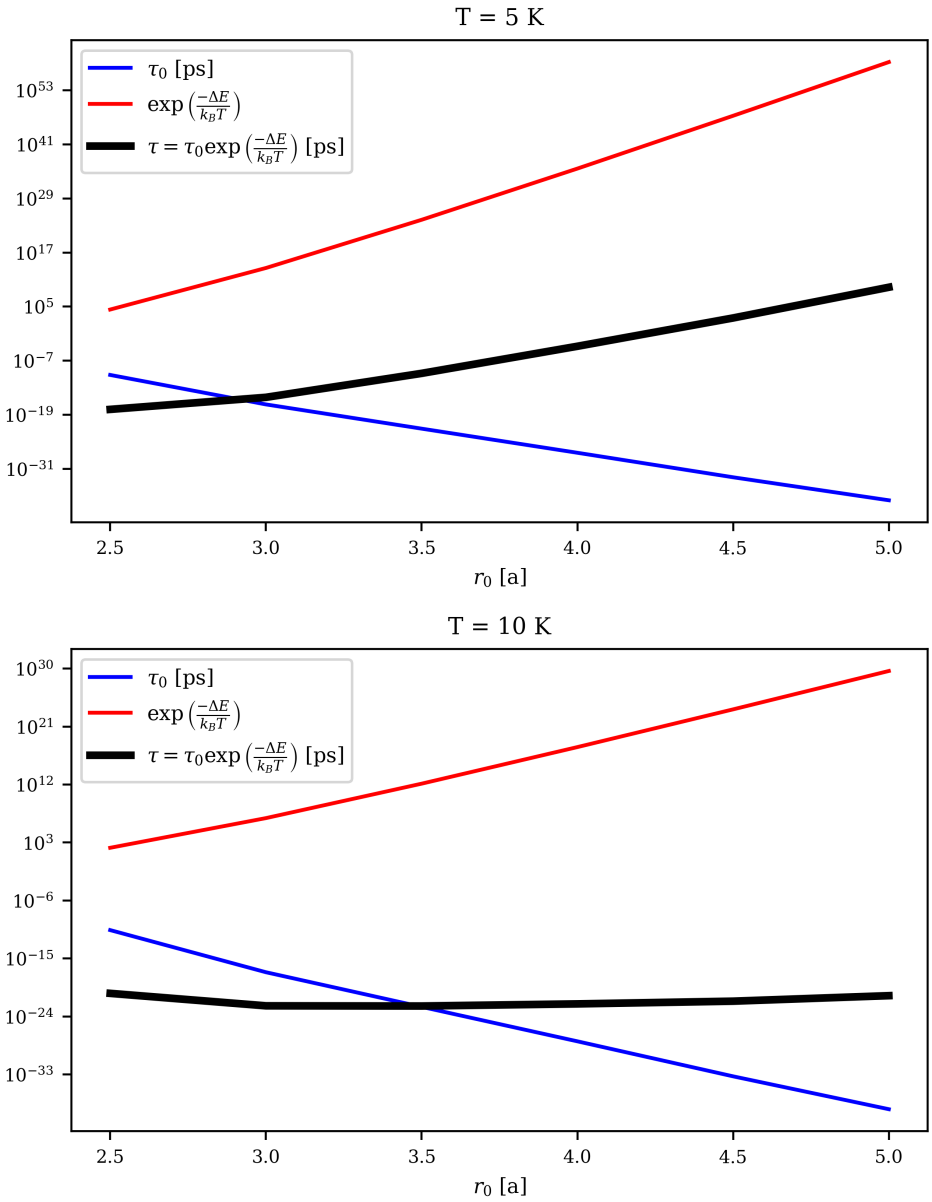


FIGURE 4.8
Predicted lifetime from HTST calculations for the decay of Hopfions to the ferromagnetic ground state against the characteristic length scale r_0. The upper plot was obtained at $T = 5$ K and the lower plot at $T = 10$ K. The total lifetime τ is plotted as a thick black line and it consists of two factors, the Boltzmann weight due to the energy barrier $[\exp\left(\frac{-\Delta E}{k_B T}\right)]$ (plotted in red) and the pre-exponential factor τ_0 (blue line). Since the (positive) contribution to the lifetime stemming from the Boltzmann weight of the energy barrier decreases with temperature, the lifetime only increases with r_0 if the temperature is low enough.

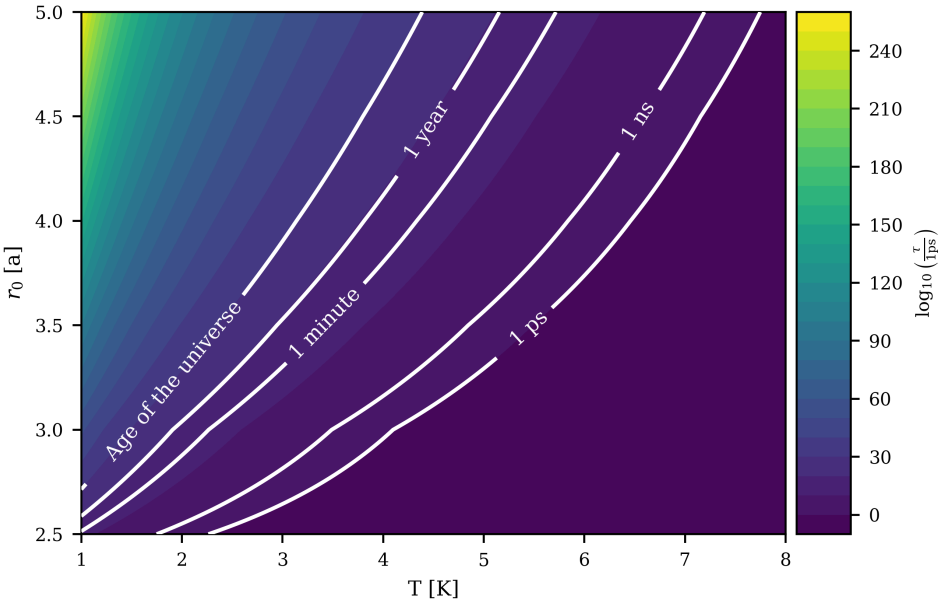


FIGURE 4.9
Arrhenius plot of the lifetime for the decay of small toroidal unit charge Hopfions in the RKBDMB model as obtained from harmonic transition state theory versus the characteristic length scale r_0. The lifetime found corresponds to the color scale on the right. White iso-lines display several lifetime thresholds.

CONCLUSION 5

This work is centered in the exciting burgeoning field of three-dimensional magnetism using the atomistic spin model.

The most relevant aspects of the spin model have been introduced concisely, emphasizing clarity and brevity. A substantial part of this thesis involved the preparation and enhancement of the Spirit code [185], specifically geared towards applications in three-dimensional magnetism simulations of three-dimensional (3D) solitons in 3D magnets. Thus, the advances in numerical techniques and theoretical insights presented in this thesis significantly extend the capabilities of the Spirit software, demonstrating its versatility and effectiveness for complex, three-dimensional magnetic systems and opening new pathways for future studies. To maintain a high degree of flexibility (especially needed for the considerations in three-dimensional magnets), it was decided to not implement the alternative harmonic transition state theory (HTST) methods in the C++ code itself, but rather as separate python workflows making use of the Snakemake [186, 187] workflow management engine.

Important improvements in the speed of converging out local energy minima were achieved through the implementation of more powerful quasi-Newton energy minimization solvers, which make use of norm-preserving coordinate transformations.

Some saddle point search methods have been reviewed – notably, the geodesic nudged elastic band method (GNEB) and an efficient extension of the GNEB which turns out to be similar to the dimer method. Furthermore, performance enhancements were realized in saddle point search methods by incorporating the Hessian matrix's action via finite differences. An efficient limited memory Fletcher-Broyden-Shannon-Goldfarb (L-BFGS) based method for finding extremal eigenvalues has been developed and discussed.

Additionally, the HTST calculations have become considerably more performant by making use of Hessian sparsity. As an alternative for systems where the Hessian cannot be considered sparse (for example, in the presence of dipole-dipole interactions) a method for determinant computation, based on the Hutchinson trace estimator has been implemented.

The derivation of HTST was revisited, closely linking it to the properties of multivariate Gaussian distributions, transparently eliminating the dependency of the expressions on the eigenbasis. Theoretical enhancements also included thermal barrier crossings, validated through a targeted test on a single spin system with uniaxial anisotropy. Moreover, the entropy contribution of zero-modes has been thoroughly revisited, resulting in the development of a flexible method capable of constructing arbitrary modes.

A significant computational challenge – the calculation of large, sparse, positive definite determinants, while efficiently excluding eigenvectors associated with small magnitude eigenvalues – has been addressed through the development and analysis of an extrapolation technique based on diagonal perturbations of the Hessian matrix.

In Chapter 4, these new computational methods have been successfully applied to study isolated free Hopfions in bulk magnets characterized by competing exchange interactions. Energy barriers were computed within a simplified, parameter-free model, and their dependence on system size, relative to the intrinsic length scale of the extended micromagnetic functional, was established [81]. Furthermore, the rate pre-factor was evaluated employing the newly developed techniques suitable for large-scale sparse Hessians. For small Hopfions, the results for the entropy contribution to the rate pre-factor agree well with previous calculations by Lobanov & Uzdin [127]. Going beyond the parameters tested in Ref. [127], to larger Hopfion sizes, it was found that the rate pre-factor and the energy barrier both increase, leading to a compensation law. Overall, the calculated lifetimes were demonstrated to be significant, particularly at low temperatures around $\sim 5\ \mathrm{K}$, despite the tendency of the rate pre-factor to decrease the Hopfion lifetime as their size increases (through manipulation of Hamiltonian exchange parameters).

In summary, the thesis provides, both, algorithmic advances as well as theoretical insights into the stability of Hopfions at finite temperatures. In particular, parameter ranges for which the Heisenberg model yields experimentally accessible lifetimes have been identified.

Outlook

Although significant progress has been achieved, much remains to be explored. Future investigations could extend the range of parameters considered for the Hopfion lifetime calculations, including higher Hopfion charges, larger systems, additional exchange shells, and further physical interactions – like Dzyaloshinskii-Moriya interactions, anisotropy etc. Extending the model to incorporate magnon-phonon interactions also presents an intriguing direction for future studies. Additionally, a systematic investigation of how sensitive the calculated

lifetimes are to rescaling based on energy arguments derived from continuum functional considerations would provide valuable insights.

The inclusion of dipolar interactions into the HTST theory presents another important, yet challenging, avenue due to inherent computational difficulties associated with determinant calculations. From a theoretical perspective, further study into the transition between Goldstone modes and harmonic modes, particularly from the viewpoint of the perpendicular velocity out of the transition state, would enhance our understanding significantly. Moreover, extensive validation of lifetime calculation methods is essential to ensure robustness and accuracy. Finally, developing the saddle point search methods further towards an effective kinetic Monte Carlo approach represents a promising research direction to explore the energy landscape of atomistic spin models more comprehensively.

APPENDIX A

A.1 HTST rate for the flip of a single spin with uniaxial anisotropy

Recall the Hamiltonian

$$\mathcal{H} = -K(\hat{s} \cdot \hat{e}_z)^2 \tag{A.1}$$

and the effective field. Since the saddle points lie in the equator and, hence, have zero z component and the minima lie at the poles with unity z-component, the energy barrier is

$$\Delta E = E^{\mathrm{SP}} - E^{\mathrm{M}} = K. \tag{A.2}$$

For this spin system, the effective field is

$$\vec{b}^{\,\mathrm{eff}}(\hat{s}) = -2K(\hat{s} \cdot \hat{e}_z)\hat{e}_z + \sqrt{2D}\,\vec{\xi}\,. \tag{A.3}$$

The embedding space Hessian is

$$\boldsymbol{H}^{\mathrm{em}} = \begin{pmatrix} 0 & 0 & 0 \\ 0 & 0 & 0 \\ 0 & 0 & -2K \end{pmatrix} \tag{A.4}$$

and for the bordered Hessian we get

$$\begin{aligned} \boldsymbol{H} &= \boldsymbol{H}^{\mathrm{em}} - \left[\hat{s} \cdot \vec{b}^{\,\mathrm{eff}}(\hat{s})\right] \boldsymbol{I}_3 \\ &= \begin{pmatrix} 2K\hat{s}_z^2 & 0 & 0 \\ 0 & 2K\hat{s}_z^2 & 0 \\ 0 & 0 & 2K(\hat{s}_z^2 - 1) \end{pmatrix}. \end{aligned} \tag{A.5}$$

This gives an unstable mode direction of $\vec{q} = \hat{e}_z$. The positive definite determinant at the minimum is, therefore,

$$\det{}^{+}\, \boldsymbol{H}^{\mathrm{M}} = 4K^2. \tag{A.6}$$

To evaluate the entropic contribution, we use (3.13) with $N_0^{\mathrm{SP}} = 1$, $N_0^{\mathrm{M}} = 0$ and $V_0^{\mathrm{SP}} = 2\pi$ [see Eq. (3.128)]

$$\begin{aligned}\frac{Z^{\mathrm{SP}}}{Z} &= 2\pi\sqrt{2\pi k_b T}^{-2}\sqrt{4K^2}\exp\left(-\frac{K}{k_b T}\right) \\ &= \frac{2K}{k_b T}\exp\left(-\frac{K}{k_b T}\right)\end{aligned} \tag{A.7}$$

The dynamical contribution is found from Eqs. (3.46) and (3.47), where only the b-term contributes, since no integration in the tangent space is carried out.

From Eq. (3.26) we get

$$\begin{aligned}\mathrm{Var}(v_\perp) = \vec{b}^T\vec{b} &= 2D\gamma'^2\left|\hat{e}_x \times \hat{e}_z + \alpha\hat{e}_z\right|^2 \\ &= 2D\gamma'^2(1+\alpha^2)\end{aligned} \tag{A.8}$$

and therefore

$$\begin{aligned}\langle v_\perp\theta(v_\perp)\rangle &= \sqrt{\frac{2D\gamma'^2(1+\alpha^2)}{2\pi}} \\ &= \sqrt{\frac{\alpha k_b T\gamma}{(1+\alpha^2)\mu\pi}}\end{aligned} \tag{A.9}$$

Resulting in the overall rate

$$\Gamma = \frac{2K}{k_b T}\sqrt{\frac{\alpha k_b T\mu\gamma}{(1+\alpha^2)\mu\pi}}\exp\left(-\frac{K}{k_b T}\right). \tag{A.10}$$

A.2 Colorcode for spin isosurfaces

The colorcode used for isosurfaces throughout this document is displayed in Fig. A.1. It indicates the direction of the spin unit vectors $\{\hat{s}_i\}$. The frequently shown $\hat{s}_z = 0$ isosurfaces only make use of the colors of the xy-plane ring.

A.3 Used software packages

All of the spin simulations were performed using the Spirit code [114, 119]. In the course of this work, Snakemake [186, 187] has been used to coordinate runs of the Spirit code through its python API.

Most of the 3D images in this thesis (spin structures, isosurfaces, illustrations) were created using the PyVista python library [188, 189]. Some 3D images were created using the graphical user interface of the Spirit code [114, 119]. Most of the 2D images (line plots, heatmaps, etc.) were created using the matplotlib python library [190]. Some

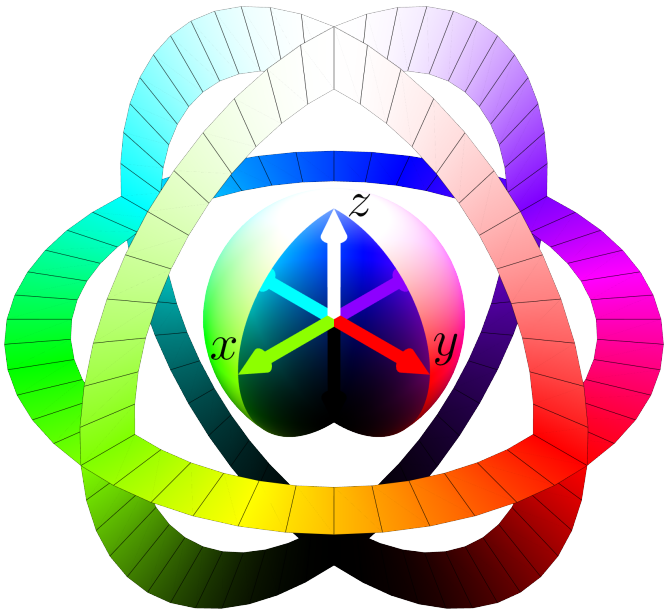


FIGURE A.1
Color code that maps the direction of the spin unit vector to hue and saturation. The azimuthal angle of the spin direction corresponds to the hue, while the polar angle determines the saturation. The spherical shape at the center of the figure is colored according to the radial vector of points on the surface. The surrounding rings show colors according to spins oriented in the xy-, yz- or xz- plane respectively. Figure reprinted with permission from [81].

images (flow charts and illustrations) were created using Tikz/PGF [191].

The "ChatGPT" large language model has been used to help with editing and proof-reading [192].

BIBLIOGRAPHY

1. Komarov, A., Komarov, K., Niang, A. & Sanchez, F. Nature of Soliton Interaction in Fiber Lasers with Continuous External Optical Injection. *Physical Review A* **89,** 013833 (2014).
2. Khaykovich, L. *et al.* Formation of a Matter-Wave Bright Soliton. *Science* **296,** 1290–1293 (2002).
3. Herr, T. *et al.* Temporal Solitons in Optical Microresonators. *Nature Photonics* **8,** 145–152 (2014).
4. Grelu, P. & Akhmediev, N. Dissipative Solitons for Mode-Locked Lasers. *Nature Photonics* **6,** 84–92 (2012).
5. Lakshmanan, M. The Fascinating World of the LandauLifshitzGilbert Equation: An Overview. *Philosophical Transactions of the Royal Society A: Mathematical, Physical and Engineering Sciences* **369,** 1280–1300 (2011).
6. Jin, X.-W. *et al.* Hidden Chiral Mode Self-Generated from Intrinsic Magnetic Heterogeneity. *Physical Review B* **110,** 184424 (2024).
7. Kläui, M. *et al.* Direct Observation of Domain-Wall Configurations Transformed by Spin Currents. *Physical Review Letters* **95,** 026601 (2005).
8. Parkin, S. S. P., Hayashi, M. & Thomas, L. Magnetic Domain-Wall Racetrack Memory. *Science* **320,** 190–194 (2008).
9. Miron, I. M. *et al.* Fast Current-Induced Domain-Wall Motion Controlled by the Rashba Effect. *Nature Materials* **10,** 419–423 (2011).
10. Ryu, K.-S., Thomas, L., Yang, S.-H. & Parkin, S. Chiral Spin Torque at Magnetic Domain Walls. *Nature Nanotechnology* **8,** 527–533 (2013).
11. Emori, S., Bauer, U., Ahn, S.-M., Martinez, E. & Beach, G. S. D. Current-Driven Dynamics of Chiral Ferromagnetic Domain Walls. *Nature Materials* **12,** 611–616 (2013).
12. Cowburn, R. P., Koltsov, D. K., Adeyeye, A. O., Welland, M. E. & Tricker, D. M. Single-Domain Circular Nanomagnets. *Physical Review Letters* **83,** 1042–1045 (1999).
13. Wachowiak, A. *et al.* Direct Observation of Internal Spin Structure of Magnetic Vortex Cores. *Science* **298,** 577–580 (2002).

14. Ruotolo, A. *et al.* Phase-Locking of Magnetic Vortices Mediated by Antivortices. *Nature Nanotechnology* **4,** 528–532 (8 2009).

15. Im, M.-Y. *et al.* Symmetry Breaking in the Formation of Magnetic Vortex States in a Permalloy Nanodisk. *Nature Communications* **3,** 983 (2012).

16. Giordano, A. *et al.* Micromagnetic Study of Spin-Transfer-Driven Vortex Dipole and Vortex Quadrupole Dynamics. *IEEE Transactions on Magnetics* **50,** 1–4 (2014).

17. Sluka, V. *et al.* Spin-Torque-Induced Dynamics at Fine-Split Frequencies in Nano-Oscillators with Two Stacked Vortices. *Nature Communications* **6,** 1–8 (1 2015).

18. Komineas, S., Vaz, C. A. F., Bland, J. A. C. & Papanicolaou, N. Bubble Domains in Disc-Shaped Ferromagnetic Particles. *Physical Review B* **71,** 060405 (2005).

19. Vukadinovic, N. & Boust, F. Three-Dimensional Micromagnetic Simulations of Magnetic Excitations in Cylindrical Nanodots with Perpendicular Anisotropy. *Physical Review B* **75,** 014420 (2007).

20. Ozatay, O. *et al.* Probing Activation Energy Barrier Distribution for Reversal of Strongly Exchange-Coupled Magnetic Multilayer Thin Films. *Applied Physics Letters* **95,** 172502 (2009).

21. Makhfudz, I., Krüger, B. & Tchernyshyov, O. Inertia and Chiral Edge Modes of a Skyrmion Magnetic Bubble. *Physical Review Letters* **109,** 217201 (2012).

22. Liu, T. *et al.* Reproducible Formation of Single Magnetic Bubbles in an Array of Patterned Dots. *Journal of Physics D: Applied Physics* **49,** 245002 (2016).

23. Rössler, U. K., Bogdanov, A. N. & Pfleiderer, C. Spontaneous Skyrmion Ground States in Magnetic Metals. *Nature* **442,** 797–801 (2006).

24. Bode, M. *et al.* Chiral Magnetic Order at Surfaces Driven by Inversion Asymmetry. *Nature* **447,** 190–193 (2007).

25. Mühlbauer, S. *et al.* Skyrmion Lattice in a Chiral Magnet. *Science* **323,** 915–919 (2009).

26. Yu, X. Z. *et al.* Real-Space Observation of a Two-Dimensional Skyrmion Crystal. *Nature* **465,** 901–904 (2010).

27. Heinze, S. *et al.* Spontaneous Atomic-Scale Magnetic Skyrmion Lattice in Two Dimensions. *Nature Physics* **7,** 713–718 (2011).

28. Schulz, T. *et al.* Emergent Electrodynamics of Skyrmions in a Chiral Magnet. *Nature Physics* **8,** 301–304 (2012).

29. Fert, A., Cros, V. & Sampaio, J. Skyrmions on the Track. *Nature Nanotechnology* **8,** 152–156 (2013).

30. Nagaosa, N. & Tokura, Y. Topological Properties and Dynamics of Magnetic Skyrmions. *Nature Nanotechnology* **8,** 899–911 (2013).

31. Sampaio, J., Cros, V., Rohart, S., Thiaville, A. & Fert, A. Nucleation, Stability and Current-Induced Motion of Isolated Magnetic Skyrmions in Nanostructures. *Nature Nanotechnology* **8,** 839–844 (2013).

32. Tomasello, R. *et al.* A Strategy for the Design of Skyrmion Racetrack Memories. *Scientific Reports* **4,** 6784 (2014).

33. Zhang, X. *et al.* Skyrmion-Skyrmion and Skyrmion-Edge Repulsions in Skyrmion-Based Racetrack Memory. *Scientific Reports* **5,** 7643 (2015).

34. Büttner, F. *et al.* Dynamics and Inertia of Skyrmionic Spin Structures. *Nature Physics* **11,** 225–228 (2015).

35. Jiang, W. *et al.* Blowing Magnetic Skyrmion Bubbles. *Science* **349,** 283–286 (2015).

36. Moreau-Luchaire, C. *et al.* Additive Interfacial Chiral Interaction in Multilayers for Stabilization of Small Individual Skyrmions at Room Temperature. *Nature Nanotechnology* **11,** 444–448 (2016).

37. Boulle, O. *et al.* Room-Temperature Chiral Magnetic Skyrmions in Ultrathin Magnetic Nanostructures. *Nature Nanotechnology* **11,** 449–454 (2016).

38. Woo, S. *et al.* Observation of Room-Temperature Magnetic Skyrmions and Their Current-Driven Dynamics in Ultrathin Metallic Ferromagnets. *Nature Materials* **15,** 501–506 (2016).

39. Landau, L. & Lifshitz, E. On the Theory of the Dispersion of Magnetic Permeability in Ferromagnetic Bodies. *Physikalische Zeitschrift der Sowjetunion* **8,** 101–114 (1935).

40. Gilbert, T. L. A Phenomenological Theory of Damping in Ferromagnetic Materials. *IEEE transactions on magnetics* **40,** 3443–3449 (2004).

41. Komineas, S. Frequency Generation by a Magnetic Vortex-Antivortex Dipole in Spin-Polarized Current. *Europhysics Letters* **98,** 57002 (2012).

42. Mohseni, S. M. *et al.* Spin TorqueGenerated Magnetic Droplet Solitons. *Science* **339,** 1295–1298 (2013).

43. Finocchio, G. *et al.* Nanoscale Spintronic Oscillators Based on the Excitation of Confined Soliton Modes. *Journal of Applied Physics* **114,** 163908 (2013).

44. Macià, F., Backes, D. & Kent, A. D. Stable Magnetic Droplet Solitons in Spin-Transfer Nanocontacts. *Nature Nanotechnology* **9,** 992–996 (2014).

45. Puliafito, V., Siracusano, G., Azzerboni, B. & Finocchio, G. Self-Modulated Soliton Modes Excited in a Nanocontact Spin-Torque Oscillator. *IEEE Magnetics Letters* **5,** 1–4 (2014).

46. Puliafito, V. *et al.* Micromagnetic Analysis of Dynamical Bubble-like Solitons Based on the Time Domain Evolution of the Topological Density. *Journal of Applied Physics* **115,** 17D139 (2014).

47. Liu, R. H., Lim, W. L. & Urazhdin, S. Dynamical Skyrmion State in a Spin Current Nano-Oscillator with Perpendicular Magnetic Anisotropy. *Physical Review Letters* **114,** 137201 (2015).

48. Zhou, Y. *et al.* Dynamically Stabilized Magnetic Skyrmions. *Nature Communications* **6,** 8193 (2015).

49. Carpentieri, M., Tomasello, R., Zivieri, R. & Finocchio, G. Topological, Non-Topological and Instanton Droplets Driven by Spin-Transfer Torque in Materials with Perpendicular Magnetic Anisotropy and DzyaloshinskiiMoriya Interaction. *Scientific Reports* **5,** 16184 (2015).

50. Slonczewski, J. C. Current-Driven Excitation of Magnetic Multilayers. *Journal of Magnetism and Magnetic Materials* **159,** L1–L7 (1996).

51. Bessarab, P. F. *et al.* Lifetime of Racetrack Skyrmions. *Scientific reports* **8,** 3433 (2018).

52. Parkin, S. & Yang, S.-H. Memory on the Racetrack. *Nature Nanotechnology* **10,** 195–198 (2015).

53. Hanyu, T. *et al.* in *Advances in Non-Volatile Memory and Storage Technology (Second Edition)* (eds Magyari-Köpe, B. & Nishi, Y.) 237–281 (Woodhead Publishing, 2019).

54. Pathak, S., Youm, C. & Hong, J. Impact of Spin-Orbit Torque on Spin-Transfer Torque Switching in Magnetic Tunnel Junctions. *Scientific Reports* **10,** 2799 (2020).

55. Khalili Amiri, P. *et al.* Low Write-Energy Magnetic Tunnel Junctions for High-Speed Spin-Transfer-Torque MRAM. *IEEE Electron Device Letters* **32,** 57–59 (2011).

56. Meo, A., Chureemart, J., Chantrell, R. W. & Chureemart, P. Magnetisation Switching Dynamics Induced by Combination of Spin Transfer Torque and Spin Orbit Torque. *Scientific Reports* **12,** 3380 (2022).

57. Ikegawa, S., Mancoff, F. B., Janesky, J. & Aggarwal, S. Magnetoresistive Random Access Memory: Present and Future. *IEEE Transactions on Electron Devices* **67,** 1407–1419 (2020).

58. Mojumder, N. N. & Roy, K. Proposal for Switching Current Reduction Using Reference Layer With Tilted Magnetic Anisotropy in Magnetic Tunnel Junctions for Spin-Transfer Torque (STT) MRAM. *IEEE Transactions on Electron Devices* **59,** 3054–3060 (2012).

59. Law, W. C. & Wong, S. D. W. in *Emerging Non-volatile Memory Technologies: Physics, Engineering, and Applications* (eds Lew, W. S., Lim, G. J. & Dananjaya, P. A.) 45–102 (Springer, Singapore, 2021).

60. Dieny, B. *et al.* Spin-Transfer Effect and Its Use in Spintronic Components. *International Journal of Nanotechnology* **7,** 591–614 (2010).

61. Fong, X. *et al.* Spin-Transfer Torque Memories: Devices, Circuits, and Systems. *Proceedings of the IEEE* **104,** 1449–1488 (2016).

62. Bhatti, S. *et al.* Spintronics Based Random Access Memory: A Review. *Materials Today* **20,** 530–548 (2017).

63. Hanif, A., Rahim, A. A. & Maab, H. A Spin Torque Nano Oscillator Model Based on DzyaloshinskiiMoriya Interaction in the IMA/PMA Bilayered Spin Valve Nanopillar: Micromagnetic Study. *Physica B: Condensed Matter* **677,** 415714 (2024).

64. Ovcharov, R. V., Hamdi, M., Ivanov, B. A., Åkerman, J. & Khymyn, R. S. Antiferromagnetic Droplet Soliton Driven by Spin Current. *Applied Physics Letters* **124,** 172406 (2024).

65. Kim, J.-V. in *Solid State Physics* (eds Camley, R. E. & Stamps, R. L.) 217–294 (Academic Press, 2012).

66. Bonetti, S. *et al.* Direct Observation and Imaging of a Spin-Wave Soliton with p-like Symmetry. *Nature Communications* **6,** 8889 (2015).

67. Liang, X., Shen, L., Xing, X. & Zhou, Y. Elongated Skyrmion as Spin Torque Nano-Oscillator and Magnonic Waveguide. *Communications Physics* **5,** 310 (2022).

68. Das, D., Muralidharan, B. & Tulapurkar, A. Skyrmion Based Spin-Torque Nano-Oscillator. *Journal of Magnetism and Magnetic Materials* **491,** 165608 (2019).

69. Luo, S. & You, L. Skyrmion Devices for Memory and Logic Applications. *APL Materials* **9,** 050901 (2021).

70. Yan, Z. *et al.* Skyrmion-Based Programmable Logic Device with Complete Boolean Logic Functions. *Physical Review Applied* **15,** 064004 (2021).

71. Navarro Vilca, S. R., Urcia Romero, S. R. & Vigo Cotrina, H. E. Spintronic Logic Devices Based on Skyrmioniums and Magnetic Defects. *ACS Applied Electronic Materials* **7,** 3432–3438 (2025).

72. Xu, T., Guo, X.-Y., Liu, Y., Du, H. & Shao, D.-F. Thin-Film Magnetic Skyrmions for Spintronic Devices. *Advanced Functional Materials* **n/a,** 2504100 (2025).

73. Hopf, H. Über die Abbildungen der dreidimensionalen Sphäre auf die Kugelfläche. *Mathematische Annalen* **104,** 637–665 (1931).

74. Rybakov, F. N. *et al.* Magnetic Hopfions in Solids. *APL Materials* **10,** 111113 (2022).

75. Whitehead, J. H. C. An Expression of Hopf's Invariant as an Integral. *Proceedings of the National Academy of Sciences* **33,** 117–123 (1947).

76. Liu, Y., Lake, R. & Zang, J. Binding a Hopfion in Chiral Magnet Nanodisk. *Physical Review B* **98,** 174437 (2018).

77. Sutcliffe, P. Skyrmion Knots in Frustrated Magnets. *Physical Review Letters* **118,** 247203 (2017).

78. Knapman, R. *et al.* Numerical Calculation of the Hopf Index for Three-Dimensional Magnetic Textures. *Physical Review B* **111,** 134408 (2025).

79. Azhar, M., Shaju, S. C., Knapman, R., Pignedoli, A. & Everschor-Sitte, K. *3D Magnetic Textures with Mixed Topology: Unlocking the Tunable Hopf Index* http://arxiv.org/abs/2411.06929 (2025). Pre-published.

80. Yu, X. *et al.* Realization and Current-Driven Dynamics of Fractional Hopfions and Their Ensembles in a Helimagnet FeGe. *Advanced Materials* **35,** 2210646 (2023).

81. Sallermann, M., Jónsson, H. & Blügel, S. Stability of Hopfions in Bulk Magnets with Competing Exchange Interactions. *Physical Review B* **107,** 104404 (2023).

82. Sutcliffe, P. Let's Twist Again. *Nature Materials* **16,** 392–393 (2017).

83. Sutcliffe, P. Hopfions in Chiral Magnets. *Journal of Physics A: Mathematical and Theoretical* **51,** 375401 (2018).

84. Tai, J.-S. B. & Smalyukh, I. I. Static Hopf Solitons and Knotted Emergent Fields in Solid-State Noncentrosymmetric Magnetic Nanostructures. *Physical Review Letters* **121,** 187201 (2018).

85. Li, S. *et al.* Mutual Conversion between a Magnetic Néel Hopfion and a Néel Toron. *Physical Review B* **105,** 174407 (2022).

86. Voinescu, R., Tai, J. S. B. & Smalyukh, I. I. Hopf Solitons in Helical and Conical Backgrounds of Chiral Magnetic Solids. *Physical Review Letters* **125,** 057201 (2020).

87. Bogolubsky, I. L. Three-Dimensional Topological Solitons in the Lattice Model of a Magnet with Competing Interactions. *Physics Letters A* **126,** 511–514 (1988).

88. Barts, E. & Mostovoy, M. Magnetic Particles and Strings in Iron Langasite. *npj Quantum Mater.* **6,** 104 (2021).

89. Faddeev, L. & Niemi, A. J. Stable Knot-like Structures in Classical Field Theory. *Nature* **387,** 58–61 (1997).

90. Grytsiuk, S. *et al.* TopologicalChiral Magnetic Interactions Driven by Emergent Orbital Magnetism. *Nature Communications* **11,** 511 (2020).

91. Zheng, F. *et al.* Hopfion Rings in a Cubic Chiral Magnet. *Nature* **623,** 718–723 (2023).

92. Saji, C., Saavedra, E., Carvalho-Santos, V. L., Nunez, A. S. & Troncoso, R. E. *Static and Dynamics of Twisted Skyrmion Tubes in Frustrated Magnets* http://arxiv.org/abs/2505.20570 (2025). Pre-published.

93. Saavedra, E. *et al.* Exploring Hopfion Stability and Dynamics in Ring-like Structures. *Results in Physics* **62,** 107835 (2024).

94. Maucher, F. & Sutcliffe, P. Colonies of Threaded Rings in Excitable Media. *Physical Review E* **102,** 010601 (2020).

95. Kasai, S., Shimizu, K., Okumura, S., Kato, Y. & Motome, Y. *Three-Dimensional Topological Superstructure of Magnetic Hopfions Threaded by Meron Strings in Easy-plane Magnets* http://arxiv.org/abs/2411.00396 (2025). Pre-published.

96. Wang, X. S., Qaiumzadeh, A. & Brataas, A. Current-Driven Dynamics of Magnetic Hopfions. *Physical Review Letters* **123,** 147203 (2019).

97. Liu, Y., Watanabe, H. & Nagaosa, N. Emergent Magnetomultipoles and Nonlinear Responses of a Magnetic Hopfion. *Physical Review Letters* **129,** 267201 (2022).

98. Castillo-Sepúlveda, S., Cacilhas, R., Carvalho-Santos, V. L., Corona, R. M. & Altbir, D. Magnetic Hopfions in Toroidal Nanostructures Driven by an Oersted Magnetic Field. *Physical Review B* **104,** 184406 (2021).

99. Göbel, B., Akosa, C. A., Tatara, G. & Mertig, I. Topological Hall Signatures of Magnetic Hopfions. *Physical Review Research* **2,** 013315 (2020).

100. Liu, Y., Hou, W., Han, X. & Zang, J. Three-Dimensional Dynamics of a Magnetic Hopfion Driven by Spin Transfer Torque. *Physical Review Letters* **124,** 127204 (2020).

101. Liu, Y., Hou, W., Han, X. & Zang, J. Erratum: Three-dimensional Dynamics of a Magnetic Hopfion Driven by Spin Transfer Torque [Phys. Rev. Lett. 124, 127204 (2020)]. *Physical Review Letters* **125,** 159901 (2020).

102. Bellizotti Souza, J. C. *et al.* Topological Transitions, Pinning and Ratchets for Driven Magnetic Hopfions in Nanostructures. *Scientific Reports* **15,** 16802 (2025).

103. Göbel, B. & Lounis, S. *Three-Dimensional Topological Orbital Hall Effect Caused by Magnetic Hopfions* http://arxiv.org/abs/2506.11448 (2025). Pre-published.

104. Raftrey, D. & Fischer, P. Field-Driven Dynamics of Magnetic Hopfions. *Physical Review Letters* **127,** 257201 (2021).

105. Metlov, K. L., Tarasenko, A. S., Bezus, Y. A. & Gordei, M. M. *Control of the Magnetic Hopfion Lattice in Helimagnet with the External Field and Anisotropy* http://arxiv.org/abs/2503.23481 (2025). Pre-published.

106. Kent, N. *et al.* Creation and Observation of Hopfions in Magnetic Multilayer Systems. *Nature Communications* **12,** 1562 (2021).

107. Hoffmann, M., Müller, G. P. & Blügel, S. Atomistic Perspective of Long Lifetimes of Small Skyrmions at Room Temperature. *Physical Review Letters* **124,** 247201 (2020).

108. Varentcova, A., Potkina, M., Malottki, S., Heinze, S. & Bessarab, P. Interplay between Size and Stability of Magnetic Skyrmions. *Nanosyst: Phys, Chem, Math.* **9,** 356–363 (2018).

109. Müller, G. P. *Advanced Methods for Atomic Scale Spin Simulations and Application to Localized Magnetic States* (Dissertation, RWTH Aachen University, 2019. - Dissertation, University of Iceland, 2019, 2019).

110. Edelman, A., Arias, T. A. & Smith, S. T. The Geometry of Algorithms with Orthogonality Constraints. *SIAM Journal on Matrix Analysis and Applications* **20,** 303–353 (1998).

111. Depondt, P. & Mertens, F. G. Spin Dynamics Simulations of Two-Dimensional Clusters with Heisenberg and DipoleDipole Interactions. *Journal of Physics: Condensed Matter* **21,** 336005 (2009).

112. Mentink, J. H., Tretyakov, M. V., Fasolino, A., Katsnelson, M. I. & Rasing, T. Stable and Fast Semi-Implicit Integration of the Stochastic LandauLifshitz Equation. *Journal of Physics: Condensed Matter* **22,** 176001 (2010).

113. Heun, K. Neue Methode zur approximativen Integration der Differentialgleichungen einer unabhängigen Veränderlichen. *Zeitschrift für Mathematik und Physik* **45,** 23–38 (1900).

114. Müller, G. P. *et al.* Spirit: Multifunctional Framework for Atomistic Spin Simulations. *Physical Review B* **99,** 224414 (2019).

115. Sallermann, M. *et al. Time Reversible Integration of the Landau-Lifshitz-Gilbert Equation* http://arxiv.org/abs/2508.12994 (2025). Pre-published.

116. Richardson, L. F. & Glazebrook, R. T. IX. The Approximate Arithmetical Solution by Finite Differences of Physical Problems Involving Differential Equations, with an Application to the Stresses in a Masonry Dam. *Philosophical Transactions of the Royal Society of London. Series A, Containing Papers of a Mathematical or Physical Character* **210,** 307–357 (1997).

117. Bessarab, P. F., Uzdin, V. M. & Jónsson, H. Method for Finding Mechanism and Activation Energy of Magnetic Transitions, Applied to Skyrmion and Antivortex Annihilation. *Computer Physics Communications* **196,** 335–347 (2015).

118. Liu, D. C. & Nocedal, J. On the Limited Memory BFGS Method for Large Scale Optimization. *Mathematical Programming* **45,** 503–528 (1989).

119. Müller, G. & Sallermann, M. *Spirit-Code/Spirit* Spirit - Atomistic Spin Framework, 2024. https://github.com/spirit-code/spirit (2024).

120. Ivanov, A. V., Uzdin, V. M. & Jónsson, H. Fast and Robust Algorithm for Energy Minimization of Spin Systems Applied in an Analysis of High Temperature Spin Configurations in Terms of Skyrmion Density. *Computer Physics Communications* **260,** 107749 (2021).

121. Press, W. H., Teukolsky, S. A., Vetterling, W. T. & Flannery, B. P. *Numerical Recipes 3rd Edition: The Art of Scientific Computing* Third edition. 1256 pp. (Cambridge University Press, Cambridge, UK, 2007).

122. Nocedal, J. & Wright, S. *Numerical Optimization* (Springer New York, 2006).

123. Ivanov, A. V., Dagbartsson, D., Tranchida, J., Uzdin, V. M. & Jónsson, H. Efficient Optimization Method for Finding Minimum Energy Paths of Magnetic Transitions. *Journal of Physics: Condensed Matter* **32,** 345901 (2020).

124. Eyring, H. The Activated Complex in Chemical Reactions. *The Journal of Chemical Physics* **3,** 107–115 (1935).

125. Wigner, E. The Transition State Method. *Transactions of the Faraday Society* **34,** 29–41 (1938).

126. Bogdanov, A. & Yablonskiui, D. Thermodynamically Stable "Vortices" in Magnetically Ordered Crystals. The Mixed State of Magnets. *Soviet PhysicsJETP [translation of Zhurnal Eksperimentalnoi i Teoreticheskoi Fiziki]* **95,** 178–182 (1989).

127. Lobanov, I. S. & Uzdin, V. M. Lifetime, Collapse, and Escape Paths for Hopfions in Bulk Magnets with Competing Exchange Interactions. *Physical Review B* **107,** 104405 (2023).

128. Von Malottki, S., Dupé, B., Bessarab, P. F., Delin, A. & Heinze, S. Enhanced Skyrmion Stability Due to Exchange Frustration. *Scientific Reports* **7,** 12299 (1 2017).

129. Bessarab, P., Uzdin, V. & Jonsson, H. Harmonic Transition-State Theory of Thermal Spin Transitions. *Physical Review B* **85,** 184409 (2012).

130. Bessarab, P. F. *et al.* Stability and Lifetime of Antiferromagnetic Skyrmions. *Physical Review B* **99,** 140411 (2019).

131. Von Malottki, S., Bessarab, P. F., Haldar, S., Delin, A. & Heinze, S. Skyrmion Lifetime in Ultrathin Films. *Physical Review B* **99,** 060409 (2019).

132. Bessarab, P. F., Uzdin, V. M. & Jónsson, H. Size and Shape Dependence of Thermal Spin Transitions in Nanoislands. *Physical Review Letters* **110,** 020604 (2013).

133. Uzdin, V. M., Potkina, M. N., Lobanov, I. S., Bessarab, P. F. & Jónsson, H. Energy Surface and Lifetime of Magnetic Skyrmions. *Journal of Magnetism and Magnetic Materials* **459,** 236–240 (2018).

134. Paul, S., Haldar, S., von Malottki, S. & Heinze, S. Role of Higher-Order Exchange Interactions for Skyrmion Stability. *Nature communications* **11,** 4756 (2020).

135. Varentcova, A. S. *et al.* Toward Room-Temperature Nanoscale Skyrmions in Ultrathin Films. *npj Computational Materials* **6,** 193 (2020).

136. Goerzen, M. A., Von Malottki, S., Kwiatkowski, G. J., Bessarab, P. F. & Heinze, S. Atomistic Spin Simulations of Electric-Field-Assisted Nucleation and Annihilation of Magnetic Skyrmions in Pd/Fe/Ir(111). *Physical Review B* **105,** 214435 (2022).

137. Goerzen, M. A., von Malottki, S., Meyer, S., Bessarab, P. F. & Heinze, S. Lifetime of Coexisting Sub-10 Nm Zero-Field Skyrmions and Antiskyrmions. *npj Quantum Materials* **8,** 54 (2023).

138. Desplat, L., Suess, D., Kim, J.-V. & Stamps, R. L. Thermal Stability of Metastable Magnetic Skyrmions: Entropic Narrowing and Significance of Internal Eigenmodes. *Physical Review B* **98,** 134407 (2018).

139. Desplat, L., Kim, J.-V. & Stamps, R. L. Paths to Annihilation of First- and Second-Order (Anti)Skyrmions via (Anti)Meron Nucleation on the Frustrated Square Lattice. *Physical Review B* **99,** 174409 (2019).

140. Desplat, L. & Kim, J.-V. Entropy-Reduced Retention Times in Magnetic Memory Elements: A Case of the Meyer-Neldel Compensation Rule. *Physical Review Letters* **125,** 107201 (2020).

141. Desplat, L., Vogler, C., Kim, J.-V., Stamps, R. L. & Suess, D. Path Sampling for Lifetimes of Metastable Magnetic Skyrmions and Direct Comparison with Kramers' Method. *Physical Review B* **101,** 060403 (2020).

142. Desplat, L. *et al.* Mechanism for Ultrafast Electric-Field Driven Skyrmion Nucleation. *Physical Review B* **104,** L060409 (2021).

143. Ritzmann, U., Desplat, L., Dupé, B., Camley, R. E. & Kim, J.-V. Asymmetric Skyrmion-Antiskyrmion Production in Ultrathin Ferromagnetic Films. *Physical Review B* **102,** 174409 (2020).

144. Desplat, L. & Kim, J.-V. Quantifying the Thermal Stability in Perpendicularly Magnetized Ferromagnetic Nanodisks with Forward Flux Sampling. *Physical Review Applied* **14,** 064064 (2020).

145. Müller, G. P. *et al.* Duplication, Collapse, and Escape of Magnetic Skyrmions Revealed Using a Systematic Saddle Point Search Method. *Physical Review Letters* **121,** 197202 (2018).

146. Jónsson, H., Mills, G. & Jacobsen, K. W. *Nudged Elastic Band Method for Finding Minimum Energy Paths of Transitions* in *Classical and Quantum Dynamics in Condensed Phase Simulations* Proceedings of the International School of Physics (WORLD SCIENTIFIC, LERICI, Villa Marigola, 1998), 385–404.

147. Henkelman, G. & Jónsson, H. Improved Tangent Estimate in the Nudged Elastic Band Method for Finding Minimum Energy Paths and Saddle Points. *The Journal of chemical physics* **113,** 9978–9985 (2000).

148. Henkelman, G., Uberuaga, B. P. & Jónsson, H. A Climbing Image Nudged Elastic Band Method for Finding Saddle Points and Minimum Energy Paths. *The Journal of Chemical Physics* **113,** 9901–9904 (2000).

149. Pedersen, A., Hafstein, S. F. & Jónsson, H. Efficient Sampling of Saddle Points with the Minimum-Mode Following Method. *SIAM Journal on Scientific Computing* **33,** 633–652 (2011).

150. Plasencia Gutiérrez, M., Argaez, C. & Jonsson, H. Improved Minimum Mode Following Method for Finding First Order Saddle Points. *Journal of chemical theory and computation* **13,** 125–134 (2017).

151. Cerjan, C. J. & Miller, W. H. On Finding Transition States. *The Journal of Chemical Physics* **75,** 2800–2806 (1981).

152. Henkelman, G. & Jónsson, H. A Dimer Method for Finding Saddle Points on High Dimensional Potential Surfaces Using Only First Derivatives. *The Journal of Chemical Physics* **111,** 7010–7022 (1999).

153. Zeng, Y., Xiao, P. & Henkelman, G. Unification of Algorithms for Minimum Mode Optimization. *The Journal of Chemical Physics* **140,** 044115 (2014).

154. Schrautzer, H., Sallermann, M., Bessarab, P. F. & Jónsson, H. Identification of Mechanisms of Magnetic Transitions Using an Efficient Method for Converging on First-Order Saddle Points. *Physical Review B* **112,** 104433 (2025).

155. Sleijpen, G. L. G. & Van der Vorst, H. A. A Jacobi–Davidson Iteration Method for Linear Eigenvalue Problems. *SIAM Review* **42,** 267–293 (2000).

156. Davidson, E. R. The Iterative Calculation of a Few of the Lowest Eigenvalues and Corresponding Eigenvectors of Large Real-Symmetric Matrices. *Journal of Computational Physics* **17,** 87–94 (1975).

157. Lanczos, C. An Iteration Method for the Solution of the Eigenvalue Problem of Linear Differential and Integral Operators. *Journal of Research of the National Bureau of Standards* **45,** 255–282 (1950).

158. Rodrigues, O. Des Lois Géométriques Qui Régissent Les Déplacements d'un Système Solide Dans l'espace, et de La Variation Des Coordonnées Provenant de Ces Déplacements Considérés Indépendamment Des Causes Qui Peuvent Les Produire. *J. Math. Pures. Appl.,* 380–440 (1840).

159. Wolfe, P. Convergence Conditions for Ascent Methods. *SIAM Review* **11,** 226–235 (1969).

160. Wolfe, P. Convergence Conditions for Ascent Methods. II: Some Corrections. *SIAM Review* **13,** 185–188 (1971).

161. Duncan, J., Wu, Q., Promislow, K. & Henkelman, G. Biased Gradient Squared Descent Saddle Point Finding Method. *The Journal of Chemical Physics* **140,** 194102 (2014).

162. Quapp, W. Gradient Extremals and Valley Floor Bifurcations on Potential Energy Surfaces. *Theoretica chimica acta* **75,** 447–460 (1989).

163. E, W. & Zhou, X. The Gentlest Ascent Dynamics. *Nonlinearity* **24,** 1831 (2011).

164. Peters, B. Common Features of Extraordinary Rate Theories. *The Journal of Physical Chemistry B* **119,** 6349–6356 (2015).

165. Lobanov, I. S. & Uzdin, V. M. The Lifetime of Micron Scale Topological Chiral Magnetic States with Atomic Resolution. *Computer Physics Communications* **269,** 108136 (2021).

166. Mökkönen, H., Ala-Nissila, T. & Jónsson, H. Efficient Dynamical Correction of the Transition State Theory Rate Estimate for a Flat Energy Barrier. *The Journal of Chemical Physics* **145,** 094901 (2016).

167. Li, X. S. An Overview of SuperLU: Algorithms, Implementation, and User Interface. *ACM Trans. Math. Softw.* **31,** 302–325 (2005).

168. Guennebaud, G., Jacob, B., *et al. Eigen V3* http://eigen.tuxfamily.org.

169. Han, I., Malioutov, D. & Shin, J. *Large-Scale Log-Determinant Computation through Stochastic Chebyshev Expansions* in *Proceedings of the 32nd International Conference on Machine Learning* International Conference on Machine Learning (PMLR, 2015), 908–917.

170. Skorski, M. *Modern Analysis of Hutchinson's Trace Estimator* in *2021 55th Annual Conference on Information Sciences and Systems (CISS)* 2021 55th Annual Conference on Information Sciences and Systems (CISS) (2021), 1–5.

171. Malottki, S. von, Goerzen, M. A., Schrautzer, H., Bessarab, P. F. & Heinze, S. *Eigenmode Following for Direct Entropy Calculation and Characterization of Magnetic Systems* http://arxiv.org/abs/2503.12109 (2025). Pre-published.

172. Manton, N. & Sutcliffe, P. *Topological Solitons* 493 pp. (Cambridge, Cambridge, U.K. ; New York, 2004).

173. Ackerman, P. & Smalyukh, I. Static Three-Dimensional Topological Solitons in Fluid Chiral Ferromagnets and Colloids. *Nature Materials* **16,** 426–432 (2016).

174. Bouligand, Y., Derrida, B., Poenaru, V., Pomeau, Y. & Toulouse, G. Distortions with Double Topological Character : The Case of Cholesterics. *Journal de Physique* **39,** 863–867 (1978).

175. Chen, B. G.-g., Ackerman, P. J., Alexander, G. P., Kamien, R. D. & Smalyukh, I. I. Generating the Hopf Fibration Experimentally in Nematic Liquid Crystals. *Physical Review Letters* **110,** 237801 (2013).

176. Hall, D. S. *et al.* Tying Quantum Knots. *Nature Physics* **12,** 478–483 (2016).

177. Korepin, V. E. & Faddeev, L. D. Quantization of Solitons. *Theoretical and Mathematical Physics* **25,** 1039–1049 (1975).

178. Sutcliffe, P. Knots in the Skyrme-Faddeev Model. *Proceedings of the Royal Society A: Mathematical, Physical and Engineering Sciences* **463,** 3001–3020 (2007).

179. Derrick, G. H. Comments on Nonlinear Wave Equations as Models for Elementary Particles. *Journal of Mathematical Physics* **5,** 1252–1254 (1964).

180. Dzyaloshinsky, I. A Thermodynamic Theory of Weak Ferromagnetism of Antiferromagnetics. *Journal of Physics and Chemistry of Solids* **4,** 241–255 (1958).

181. Bogdanov, A. New Localized Solutions of the Nonlinear Field Equations. *JETP Letters* **62,** 247–251 (1995).

182. Hoffmann, M. & Blügel, S. Systematic Derivation of Realistic Spin Models for Beyond-Heisenberg Solids. *Physical Review B* **101,** 024418 (2020).

183. Meyer, W. & Neldel, H. Concerning the Relationship between the Energy Constant Epsilon and the Quantum Constant Alpha in the Conduction-Temperature Formula in Oxydising Semi-Conductors. *Phys. Z* **38,** 1014–1019 (1937).

184. Yelon, A., Movaghar, B. & Branz, H. M. Origin and Consequences of the Compensation (Meyer-Neldel) Law. *Physical Review B* **46,** 12244–12250 (1992).

185. Müller, G. P. *et al. Spirit-Code/Spirit: New Desktop GUI, Update to C++14* version v2.2.0. Zenodo, 2023. https://zenodo.org/records/7746552 (2025).

186. Mölder, F. *et al.* Sustainable Data Analysis with Snakemake [Version 2; Peer Review: 2 Approved]. *F1000Research* **10,** 33 (2021).

187. Köster, J. *Snakemake/Snakemake* Snakemake, 2025. https://github.com/snakemake/snakemake (2025).

188. Sullivan, C. B. & Kaszynski, A. PyVista: 3D Plotting and Mesh Analysis through a Streamlined Interface for the Visualization Toolkit (VTK). *Journal of Open Source Software* **4,** 1450 (2019).

189. *PyVista* https://github.com/pyvista (2025).

190. Hunter, J. D. Matplotlib: A 2D Graphics Environment. *Computing in Science & Engineering* **9,** 90–95 (2007).

191. *PGF/TikZ Manual - Complete Online Documentation* https://tikz.dev/ (2025).

192. OpenAI. *ChatGPT* https://chat.openai.com/ (2023).

LIST OF PUBLICATIONS

- Gideon P Müller, Markus Hoffmann, Constantin DiSSelkamp, Daniel Schürhoff, Stefanos Mavros, **Moritz Sallermann**, Nikolai S Kiselev, Hannes Jónsson, Stefan Blügel
  "Spirit: Multifunctional framework for atomistic spin simulations", Physical Review B **99**, 224414 (2019)
  – The author contributed to the *Spirit* code by implementing dipolar interactions with the convolution theorem and improved the computation of the topological charge (Skyrmion winding number) to correctly handle periodic boundary conditions and helped a little with the preparation of the manuscript. No figures or text have been included in this thesis.

- Hongying Jia, Bernd Zimmermann, Markus Hoffmann, **Moritz Sallermann**, Gustav Bihlmayer, Stefan Blügel
  "Material systems for FM-/AFM-coupled skyrmions in Co/Pt-based multilayers"
  Physical Review Materials **4**, 094407 (2020)
  – The author contributed by fixing numerical instabilities in the shooting method calculator and by improving the "Swiss army knife" Skyrmion radius calculations by improving the performance of the magnetostatic interactions and by porting it to C++. He also helped with the shooting method calculations and in the preparation of the manuscript. No figures or text have been included in this thesis.

- Philipp Rüßmann, Jordi Ribas Sobreviela, **Moritz Sallermann**, Markus Hoffmann, Florian Rhiem, Stefan Blügel
  "The AiiDA-Spirit Plugin for Automated Spin-Dynamics Simulations and Multi-Scale Modeling Based on First-Principles Calculations", Frontiers in Materials **9**, 825043 (2022)
  – The author contributed by implementing the Monte-Carlo method in the AiiDa Spirit plugin. No figures or text have been included in this thesis.

- Dongwook Go, **Moritz Sallermann**, Fabian R Lux, Stefan Blügel, Olena Gomonay, Yuriy Mokrousov "Noncollinear spin current for switching of chiral magnetic textures", Physical Review Letters **129**, 097204 (2022)
  – The author contributed by implementing basis cell resolved

spin polarized currents in Spirit. No figures or text have been included in this thesis.

- Amal Aldarawsheh, Imara Lima Fernandes, Sascha Brinker, **Moritz Sallermann**, Muayad Abusaa, Stefan Blügel, Samir Lounis
  "Emergence of zero-field non-synthetic single and interchained antiferromagnetic skyrmions in thin films", Nature Communications **13**, 7369 (2022)
  – The author contributed by writing several scripts for the Spirit code to help with running the simulations as well as analysis of results and writing of the manuscript. No figures or text have been included in this thesis.

- **Moritz Sallermann**, Hannes Jónsson, Stefan Blügel
  "Stability of hopfions in bulk magnets with competing exchange interactions", Physical Review B **107**, 104404 (2023)
  – The author came up with the concept of the paper, implemented the NEB dimer method in Spirit and performed all of the simulations as well as the analysis and writing the bulk of the manuscript. Part of the content of this paper is used in Chapter 4 and is indicated by footnotes in the relevant section(s).

- Amal Aldarawsheh, **Moritz Sallermann**, Muayad Abusaa, Samir Lounis
  "A spin model for intrinsic antiferromagnetic skyrmions on a triangular lattice" Frontiers in Physics **11** (2023)
  – The author contributed by helping to write several scripts for the Spirit code and providing general advice about how to perform the atomistic simulations. No figures or text have been included in this thesis.

- Amal Aldarawsheh, **Moritz Sallermann**, Muayad Abusaa, Samir Lounis
  "Intrinsic Néel antiferromagnetic multimeronic spin textures in ultrathin films" The Journal of Physical Chemistry Letters **14**, 8970-8978 (2023)
  – The author contributed by helping to write several scripts for the Spirit code and providing general advice about how to perform the atomistic simulations. No figures or text have been included in this thesis. The author also implemented spin-polarized currents for anti-ferromagnets.

- Hendrik Schrautzer, **Moritz Sallermann**, Pavel F Bessarab, Hannes Jónsson
  "Identification of mechanisms of magnetic transitions using an efficient method for converging on first order saddle points"

arXiV preprint (2403.11799) (accepted by Physical Review B) (2024)
– The author is equally contributing with Hendrik Schrautzer. He came up with idea of the manuscript, did the theoretical work and wrote roughly 50% of the manuscript. Part of the content of this paper is used in Chapter 2 and is indicated by footnotes in the relevant section(s).

- Amal Aldarawsheh, **Moritz Sallermann**, Muayad Abusaa, Samir Lounis
"Current-driven dynamics of antiferromagnetic skyrmions: from skyrmion Hall effects to hybrid inter-skyrmion scattering", NPJ Spintronics **2**, 41 (2024)
– The author contributed by helping to write several scripts for the Spirit code and providing general advice about how to perform the atomistic simulations. No figures or text have been included in this thesis.

- **Moritz Sallermann**, Amrita Goswami, Alejandro Peña-Torres, Rohit Goswami
"Flowy: High performance probabilistic lava emplacement prediction" Computer Physics Communications **315**, 109745 (2025)
– The author came up with the idea for the manuscript and performed roughly half of the Coding work for the C++ "Flowy" code and roughly half of the analysis and manuscript writing. No figures or text have been included in this thesis.

- **Moritz Sallermann**, Thorsteinn Freygardsson, Sergei Egorov, Pavel Bessarab, Grzegorz Kwiatkowski, Hannes Jónsson
"Time Reversible Integration of the Landau-Lifshitz-Gilbert Equation" arXiV preprint (2508.12994) (2025)
– The author came up with the idea for "implicit" time reversible integrator wrote the manuscript and implemented the Suzuki-Trotter solver in the "Spirit" code. Part of the content of this paper is used in Chapter 1 and is indicated by footnotes in the relevant section(s).

PRODUCED SOFTWARE AND SCRIPTS

- **Spirit**: https://zenodo.org/records/7746552. I have contributed various pieces of code to Spirit. Details can be found in the commit history of https://github.com/spirit-code/spirit.
- **hopfion-illustrations**: https://github.com/MSallermann/hopfion_illustrations. PyVista scripts to produce the illustrations in the introduction.
- **spirit-extras**: spirit-extras(https://github.com/MSallermann/spirit_extras). A python package with helper classes for working with Spirit's python API
- **st-solver-tests**: https://github.com/MSallermann/st_solver_tests. Testing the Suzuki-Trotter solver in Spirit.
- **cos2_ridge_following**: https://github.com/MSallermann/cos2_ridge_following. Implementation of the "Cosine square" ridge following method, described in Chap. 2.
- **energy surfaces**: https://github.com/MSallermann/energy_surfaces. Toy energy surfaces implemented in python (with numba). Useful for testing saddle point searches.
- **chebdet**: https://github.com/MSallermann/chebdet. Parallel implementation of the stochastic chebyshev determinant sampling, described in Chap. 3.
- **mpft_post_processor**: https://github.com/MSallermann/mfpt_post_processor. C++ implementation for computing the mean first passage time from trajectory data. Used in Chap 3.
- **lifetime_tests**: https://github.com/MSallermann/lifetime_tests. Implementation and tests of the extended form of HTST, described in Chap. 3.
- **dimer_dangling**: https://github.com/MSallermann/mep_rayleigh_dimer_dangling. Script for MEP constrained minimization. Useful for "reverse-engineering" an MEP from a saddle-point.

- **hopfion_simulations**: https://github.com/MSallermann/hopfion_simulations. Scripts for finding the saddle points for Hopfions with the dimer method [81].
- **hopfion_lifetimes**: https://github.com/MSallermann/hopfion_lifetimes. Workflows for computing the lifetimes of Hopfions as per Chap 4.

COTUTELLE AGREEMENT

This thesis has been written under a Cotutelle agreement between RWTH Aachen and the University of Iceland.

EIDESSTATTLICHE ERKLÄRUNG

Moritz Sallermann erklärt hiermit, dass diese Dissertation und die darin dargelegten Inhalte die eigenen sind und selbstständig, als Ergebnis der eigenen originären Forschung, generiert wurden.

Hiermit erkläre ich an Eides statt:

1. Diese Arbeit wurde vollständig oder gröSStenteils in der Phase als Doktorand dieser Fakultät und Universität angefertigt;
2. Sofern irgendein Bestandteil dieser Dissertation zuvor für einen akademischen Abschluss oder eine andere Qualifikation an dieser oder einer anderen Institution verwendet wurde, wurde dies klar angezeigt;
3. Wenn immer andere eigene- oder Veröffentlichungen Dritter herangezogen wurden, wurden diese klar benannt;
4. Wenn aus anderen eigenen- oder Veröffentlichungen Dritter zitiert wurde, wurde stets die Quelle hierfür angegeben. Diese Dissertation ist vollständig meine eigene Arbeit, mit der Ausnahme solcher Zitate;
5. Alle wesentlichen Quellen von Unterstützung wurden benannt;
6. Wenn immer ein Teil dieser Dissertation auf der Zusammenarbeit mit anderen basiert, wurde von mir klar gekennzeichnet, was von anderen und was von mir selbst erarbeitet wurde;
7. Ein Teil oder Teile dieser Arbeit wurden zuvor veröffentlicht und zwar in:
   - Sallermann, Jónsson & Blügel [81]
   - Schrautzer, Sallermann, Bessarab & Jónsson [154]
   - Sallermann, Freygardsson, Egorov, Bessarab, Kwiatkowski & Jónsson [115]

Moritz Sallermann